Engineering Protein-Drug Conjugates for Solid Tumor Immunotherapy

by
Ian Nessler

A dissertation submitted in partial fulfillment
of the requirements for the degree of
Doctor of Philosophy
(Chemical Engineering)
in the University of Michigan
2022

Doctoral Committee:

Associate Professor Greg M. Thurber, Chair
Professor Jennifer Linderman
Professor Peter Tessier
Associate Professor Fei Wen

Ian Nessler

inessler@umich.edu

ORCID ID: 0000-0002-9508-0167

DEDICATION

This dissertation is dedicated to
Mom and Dad
Katie & Ivy

ACKNOWLEDGMENTS

The work conducted and presented herein would not have been possible without the wide support network I experienced from colleagues, friends, and family starting at the University of Iowa and continuing to grow at the University of Michigan.

My research experience began in a Computational Biomedical Engineering lab at the University of Iowa under the mentorship of Dr. Mike Schnieders. While I may not have always believed in my ability to conduct research, Mike constantly provided praise, support, and guidance that poised me to achieve this work. In addition to instilling the ideals of rigorous scientific research, he connected me to my first industry experience at Genentech, allowed me the academic freedom to publish my first, first-author paper, and backed my successful application to the National Science Foundation's Graduate Research Fellowship (NSF GRFP) all of which led to my appointment at the University of Michigan. I would also like to thank Dr. Allan Guymon for serving as a mentor in my undergraduate work and Kelly Thornburg for her support in my successful NSF GRFP application.

Arriving at Michigan I was fortunate to find a strong mentor in Dr. Greg Thurber. Over the course of almost 6 years Greg has continued to push the limit of my understanding of my research. Pressing me to ask additional questions even after I thought I had it figured out. Even in my first year, Greg made me feel like an equal and was always happy to discuss the complex (and sometimes basic) parts of my research. Again, while I would question my ability conduct research, Greg was always adamant that I was capable, and we only needed to better understand the data to

come to our eventual conclusion. This unwavering support allowed me to explore the more difficult aspects of my research with confidence and resulted in the work, of which, I am most proud. Additionally, I would like to thank my dissertation committee members: Dr. Pete Tessier, Dr. Jennifer Linderman, and Dr. Fei wen. Further, I want to acknowledge the mentoring provided by Dr. Pete Tessier during research collaboration and a GSI appointment which led to discussions on research, teaching, and career choices that have supported me holistically. I would also like to express gratitude to Dr. Lola Eniola-Adefeso for providing opportunities to mentor and teach through the peer mentoring program which I have valued dearly.

It's impossible to measure the impact of Thurber lab members on my development as a researcher and person. Liang Zhang, Sumit Bhatnagar, Cornelius Cilliers, Tejas Navaratna, Lydia Atangcho, Bruna Menezes, Eshita Khera, Reggie Evans, Anna Kopp, Marshall Case, Celia Shujun Dong, Haolong Huang, Jane Kwon, Melissa Calopiz, Baron Rubahamya, and Tiexin Wang have all contributed in sometimes small and at other times large ways to this thesis. Specifically, I want to thank Cornelius as mentor and teacher as well as Sumit for always having an open ear for discussion and a critical thinking mindset. I had the pleasure of working with multiple undergraduates on these projects and would like to thank them: Darby Mckernan, Matt Ratanapanichkich, and Matthew Proefke. Additionally, the Eniola lab members deserve recognition for their helpful discussion and support as well as lending supplies when experimental outlooks appeared most bleak.

I would like to thank my groomsmen, IM friends, Trivia friends, board game friends, and soccer friends for providing outlets for the downtimes and moments to celebrate the good times. My family including my parents who have offered support through every uncertain moment in my life and offered positive perspectives in difficult times. My brother Aaron Nessler, sister-in-law

Jenny Nessler, nephew Callum, and niece Azelie for their support. Additionally, Ann, Tom, and Hannah Langenfeld for their support.

Finally, I want to thank the two who have been by my side during every (good or bad) day of my PhD, Katie Langenfeld and Ivy. Without their infallible support during the difficult times and dedication to pause and celebrate moments of success this dissertation would not have been possible.

TABLE OF CONTENTS

LIST OF FIGURES

List of Appendices

Abstract

Antibody therapies have dominated biologics for many years. The innate specificity and long half-lives of these proteins provide a sustained response in many disease indications, including cancer. However, solid tumors can often evade treatment by antibodies alone which has led to the development of antibody-drug conjugates (ADCs). Although successful development of ADCs is a recent endeavor, the concept of a "magic bullet" or an agent that could kill unhealthy cells while leaving healthy cells unharmed was discussed in the early 1900's. ADCs have experienced a rocky start but are currently experiencing unprecedented success. To better understand the mechanisms behind these clinical trends, this work first improved upon previously existing near infrared fluorophore techniques to increase the limit of detection of overall antibody uptake and cellular degradation for use in low expression target systems. Conjugating proteins of interest to a non-residualizing and residualizing fluorophore provided total protein uptake, tumor distribution, and cellular degradation in vivo. Utilizing similar fluorescent techniques, the tumor distribution for a panel of protein-drug conjugates with varying binding kinetics and size was tracked in vitro and in vivo. Computational simulations with a Krogh cylinder model along with in vitro and in vivo assays highlighted the internalization rate as a key feature to balance tumor penetration with cellular uptake and potency. The results demonstrated that rapid internalization rates induced by biparatopic antibodies with a highly potent payload against a highly expressed target (Prostate Specific Membrane Antigen, PSMA) increase the potency against cell lines in vitro but lead to greater heterogeneity in delivery and lower efficacy in vivo. In contrast, a slower

internalization rate allowed for greater tumor penetration and higher efficacy even with decreased payload delivery per cell. Therefore, greater tumor penetration was beneficial for tumor efficacy with subsaturating doses. However, more recent ADCs utilize moderate potency payloads that can deliver saturating doses to the tumor due to their greater tolerability. Next, the impact of internalization rate under saturating conditions for anti-CEA ADCs. In contrast to the subsaturating PSMA ADCs, the more rapidly internalized anti-CEA cross-linking ADC delivered more payload to each cell in vitro and in vivo, resulting in greater efficacy when compared to a slower internalizing ADC. This work demonstrated the need to design ADCs to match the key tumor parameters associated with cell delivery to achieve a therapeutic dose in the largest fraction of tumor cells. Finally, a model system was developed to determine the relative importance of the three known mechanisms of ADC action: 1) receptor modulation, 2) payload delivery, and 3) Fc-effector function. In a genetically engineered mouse model, each mechanism played a role in the overall efficacy. In conclusion, this work developed improved methods for tracking ADCs in vitro and in vivo and demonstrated how internalization rate can be modified, depending on the target and therapeutic/payload properties, to provide maximum effect in vivo. Importantly, these results can differ from maximum efficacy in vitro, but computational methods were shown to be able to predict the optimal properties to aid in effective ADC design.

Chapter I

Introduction

1.1 Antibody Therapy

Antibody-Drug Conjugates (ADCs) are made from 3 components: an antibody backbone, conjugating linker, and a potent payload. The largest component of an ADC is the antibody. The first FDA approval for an antibody therapy was in 1986 for murine antibody (muromonab-CD3). Since then, these agents have quickly been established as a dominant drug class with 8 of the 10 best-selling drugs belonging to biologics. Advances in protein engineering have fueled this rise by developing methods to move from murine antibodies to humanized, chimeric, and fully human antibodies as well as increase the efficiency of developing antibodies against novel targets. In 2020, this capability was demonstrated by bamlanivimab and the casirivimab/imdevimab cocktail, which were developed and authorized for emergency use against COVID-19 in ~10 months. Even outside of these unusual circumstances the rate of new FDA approved antibodies has been increasing. From 1997-2013 (17 years period) only 34 antibodies were FDA approved while the past ~7 years (2014-2020) have provided 61 therapies[1]. With an additional 38 antibody therapeutics in late-stage clinical trials as of November 2020, it appears that antibodies will continue to lead the field.

Antibodies are naturally occurring proteins of the humoral immune system which protect the body from foreign pathogens. They are commonly depicted as “Y-shaped” proteins, with two

binding regions (Fabs) that recognize an antigen with high specificity, in addition to a constant (Fc) region responsible for immune cell interaction and the antibodies long circulating half-life. Of the five human antibody isotypes, the most common antibody isotype, IgG, represents ~75% of serum antibodies and has a large molecular weight of ~150kDa. Remarkably, <10% of an antibody's amino acids are responsible for antigen binding. The combination of these amino acids forms the complementary determining regions (CDRs) which are crucial for antigen specificity.

Current antibody therapies function through four main mechanisms of action: Blocking, receptor signaling, antibody dependent cell mediated cytotoxicity (ADCC), and complement dependent cytotoxicity (CDC)[2]. These mechanisms begin with the binding of the variable binding region to the specified antigen. Blocking antibodies aim to interrupt the binding of endogenous ligands to cellular receptors, diminishing their signaling effect by binding either the ligand or the receptor. Immune checkpoint inhibitors (ICIs) are a recent advancement and illustration in blocking antibodies for which the 2018 Nobel prize award was given to James Allison and Tasuko Honjo. These antibodies are lauded for their long term and durable responses in the clinic albeit in only a subset of patients. In other antibody indications, the antibody disrupts cellular signaling by interrupting cellular surface receptor interactions such as Trastuzumab. In addition to the blocking and signaling mechanisms of action, ADCC and CDC can also occur in tandem. Both mechanisms require host immune cells to recognize the Fc portion of the antibody, induce the release of proteins which lyse the targeted cell.

The innate complexity of antibodies allows for protein engineering approaches to selectively modify individual components of the antibody to further elicit particular mechanisms

of action. Changing the antibody isotype can significantly impact the role of ADCC and CDC function, while point mutations can alter pharmacokinetics, binding characteristics, and overall effectiveness. Some of the most complex and advanced antibody therapeutics include ADCs which offer a wide design space for perfecting therapeutic action while at the same time increasing complexity.

1.2 Protein Drug Conjugates

Protein drug conjugates are hybrid drugs combining a proteins specificity to a tumor antigen with the toxicity of the small molecule payload. The dominant protein scaffold in the clinic is the antibody. Antibodies are extremely tight and specific binders such that a cytotoxic payload that is used in conjunction with the antibody backbone can be more potent than conventional chemotherapeutics with relative potencies of 100-10,000 fold greater toxicity[3]. The antibody backbone of the ADC is engineered to bind tumor-specific or tumor associated antigens to ensure only cancer cells receive the toxic payload. Although ADCs are designed to limit side effects (tumor selectivity of antibodies and stability of the chemical linker[4]), systemic toxicity caused by the small molecule payload has been deemed a critical factor in some clinical failures[5]. Although 11 ADCs have been approved[6], a significant fraction of ADCs do not achieve FDA approval demonstrating a need for improvement in mechanistic understanding of ADC drug action. The payload toxicity can also limit the dose and frequency of treatment, lowering penetration depths, and allowing regrowth between doses (currently given every 3 weeks)[7]. Since antibodies are large and delivered to tissues with high antigen expression, they tend to penetrate only a few cell layers past the blood vessel[8, 9]. The limited penetration leads to perivascular cell death which has the potential to cut off tumor blood supply, oxygen, and nutrients[10], however, revascularization in

between treatment provides relief from these factors. These results demonstrate the crucial role of the tumor microenvironment in the efficacy of ADCs as well as some common challenges of solid tumor targeting.

1.3 Challenges of Solid Tumor Therapy

Unlike healthy tissue, tumor tissue is characterized by a unique vasculature and cellular composition. As a result, the tumor microenvironment consists of high interstitial pressure and dynamic, aberrant vasculature characterized by leakiness that causes inefficient distribution of pharmaceuticals[11]. The poor distribution profile not only leads to decreased efficacy; it can result in the selection of resistant tumor cells[12]. A fundamental understanding of tumor specific parameters (vessel density, receptor expression/internalization, etc.) that affect therapeutic distribution is necessary for developing clinically successful drugs. Key protein scaffold properties such as affinity, size, and drug antibody ratio (DAR) can be adapted to match tumor parameters and maximize efficacy. The Thurber lab has previously demonstrated that for a tumor with extremely high receptor expression, the coadministration of Herceptin along with the clinical dose of Kadcyla can improve tumor regression by effectively increasing the penetration distance of the ADC without decreasing efficacy[13]. This highlights the importance of the tumor microenvironment/distribution on therapeutic efficacy for antibody therapies.

An additional consideration is the immune cell infiltrate. Tumor associated macrophages are some of the most common innate immune cells intertwined in the tumor stroma. There are two main types categories of macrophages M1 (inflammatory) and M2 (healing). Although these subclasses have high plasticity and exist more on a spectrum than a binary basis, an increase in

M1 macrophages is a positive indicator in an immunological context compared to an increase in M2 macrophages. In addition to the macrophage subclasses, there are various classes of T-lymphocytes (cytotoxic, helper, and regulatory T-cells). The relative abundance and status of each of these cells play a role in the overall efficacy of the antibody therapy.

1.4 Near Infrared (NIR) Fluorescence Imaging

Understanding the distribution of proteins on multiple length scales has been key in the advancement of next generation biologics. Although these agents act at the molecular scale, it is necessary to quantify both the microscopic (sub-cellular and cellular) and macroscopic (tissue and organ) distribution to bridge the relationship between pharmacokinetics (PK) and pharmacodynamics (PD)[14, 15]. PK is routinely measured through multiple techniques: radiolabels, florescent labels, ELISA, and mass spectrometry. However, quantitative measures of ADC rates and tumor parameters that influence delivery and distribution in vivo are limited[16]. Fluorescently labeled proteins can provide semi-quantitative as well as quantitative data depending on the instruments used.

Semi-quantitative Euclidean distance mapping of tumor histology can provide a glimpse into the relative concentrations of protein at varying penetration depths, but quantitative pharmacology is required to gather rates that support simulations as well as identify therapeutic thresholds required to induce a response. Flow cytometry and fluorescently conjugated proteins provide a method to identify not only fraction of cells targeted but also the number of proteins or payloads delivered to these targeted cells. Using this information provides a dial that can be tuned to target the most cells with a therapeutic payload dose. While distribution of biologics across

multiple length scales is readily measured using near-infrared (NIR) labeling to track biologics; quantifying protein degradation requires a second NIR label.

Chapter II

Practical Guide for Quantification of In Vivo Degradation Rates for Therapeutic Proteins with Single-Cell Resolution Using Fluorescence Ratio Imaging

2.1 Publication Information

Nessler I, Cilliers C, Thurber GM. Practical Guide for Quantification of In Vivo Degradation Rates for Therapeutic Proteins with Single-Cell Resolution Using Fluorescence Ratio Imaging. Pharmaceutics. 2020; 12(2):132. https://doi.org/10.3390/pharmaceutics12020132

Modifications have been made to the published document to adapt the content to this text. The goal of this chapter is to identify a novel fluorescent dye pair for protein degradation imaging with greater sensitivity than previous fluorescent methods for use in indications with low target expression.

2.2 Abstract

Many tools for studying the pharmacokinetics of biologics lack single-cell resolution to quantify the heterogeneous tissue distribution and subsequent therapeutic degradation in vivo. This protocol describes a dual-labeling technique using two near-infrared dyes with widely differing residualization rates to efficiently quantify in vivo therapeutic protein distribution and degradation rates at the single cell level (number of proteins/cell) via ex vivo flow cytometry and histology.

Examples are shown for four biologics with varying rates of receptor internalization and degradation and a secondary dye pair for use in systems with lower receptor expression. Organ biodistribution, tissue-level confocal microscopy, and cellular-level flow cytometry were used to image the multi-scale distribution of these agents in tumor xenograft mouse models. The single-cell measurements reveal highly heterogeneous delivery, and degradation results show the delay between peak tumor uptake and maximum protein degradation. This approach has broad applicability in tracking the tissue and cellular distribution of protein therapeutics for drug development and dose determination.

2.3 Background

Therapeutic proteins remain one of the fastest growing areas of pharmaceutical development in the treatment of many diseases, including cancer and autoimmune disorders[17-19]. The varying physicochemical properties of next generation proteins, including molecular weight, molecular radius, avidity, charge, etc., can result in unexpected pharmacokinetics, making it difficult to predict their distribution[20] and subsequent efficacy. Although these agents act at the molecular scale, it is necessary to quantify both the microscopic (sub-cellular and cellular) and macroscopic (tissue and organ) distribution in order to bridge the relationship between pharmacokinetics (PK) and pharmacodynamics (PD)[21-23]. For example, in the case of antibody drug conjugates (ADCs), efficacy can be enhanced by understanding the internalization/degradation and payload release at the subcellular scale, the average number and variability of payload molecules required to achieve cell death *in vivo* at the cellular scale[13], the number of cells in the tumor receiving a therapeutic dose at the tissue scale, and the healthy tissue exposure and resulting toxicity at the whole organ level[24]. The distribution of biologics across

multiple length scales is readily measured using near-infrared (NIR) labeling to track biologics; however, to quantify protein degradation, a second NIR label is needed.

One approach uses dual NIR labeling of proteins with a non-residualizing and residualizing fluorophore. The residualization properties of many molecular labels including radiolabels and other visible light fluorophores are currently known[19, 25, 26]. For example, in nuclear imaging ^{125}I is a non-residualizing label, which results in washout of the signal once the iodine is released, typically following protein degradation. Therefore, the signal approximates intact protein. In contrast ^{111}In, ^{68}Ga, ^{98}Zr are residualizing agents, which approximates the cumulative uptake of the protein[27]. In an elegant approach, Ferl et al. dually labeled different engineered protein variants with residualizing ^{111}In and non-residualizing ^{125}I radioisotopes to measure *in vivo* protein degradation[28]. To model the degradation within each organ, a known quantity of each isotope was injected and the relative amount of ^{125}I to ^{111}In was measured over time. This method provides robust results for tracking organ biodistribution and degradation at the whole animal and organ level (e.g. [29]). Motivated by this approach, we measured the residualization properties of NIR fluorophores, identifying both residualizing and non-residualizing dyes[30]. Using a dual non-residualizing and residualizing label, the local intact and degraded protein can be detected[26-28, 30, 31]. The current protocol is similar in concept to the radiolabeling approach but uses NIR fluorescence to increase spatial and temporal resolution. This allows measurement of degradation and distribution across multiple length scales using the high spatial resolution of fluorescence and ability to quantify kinetic rates, such as degradation at the cellular level *in vivo* while reducing safety concerns, time/half-life constraints, and expense of radioactivity. Importantly, multiple

length scales can be analyzed *in vivo* for the *same* animal, providing insight into heterogeneity and inter-animal variability.

Previously, we have demonstrated this technique by measuring the distribution and degradation of the FDA approved ADC Kadcyla (T-DM1) at several length scales, *in vitro* and *in vivo*[13]. We found that the distribution of a clinical dose (3.6 mg/kg) of T-DM1 in HER2 expressing tumor xenografts was highly heterogeneous and perivascular. We measured the amount of degraded ADC and corresponding release of payload and demonstrated that the targeted perivascular cells received more small molecule payload than necessary to achieve cell death, resulting in "overkill" of the perivascular cells[13]. Additionally, we showed that efficacy and survival is improved when the same payload dose is distributed more homogeneously throughout the tumor; targeting more cells with a lower payload dose[13]. Building on the previous results, we apply the protocol to three other well-characterized proteins, EGF, cetuximab, and anti-A33 antibody, both *in vitro* and *in vivo* to demonstrate the wide applicability of the technique for the measurement of cellular degradation and tissue distribution of other novel protein therapeutics. The method is based on the different residualization properties of two NIR fluorescent dyes, which are used to distinguish intact versus degraded protein. NIR wavelengths have low tissue autofluorescence and high tissue penetration, reducing optical artifacts[32, 33]. NIR fluorescence combines the whole animal and biodistribution capabilities of radiolabels[34, 35] with the tissue and cellular kinetic measurements of fluorescence[36]. We also provide an alternative dye pair (utilizing a visible light dye) to measure degradation with greater sensitivity for lower expressing targets. The ability to track the delivery of therapeutic proteins from whole animal to subcellular resolution

enables investigation of the multi-scale distribution of lead compounds *in vitro* and *in vivo* and facilitates the development of predictive models for lead compound selection.

2.4 Results

For dual labeling, the method requires two NIR fluorescent dyes that have substantially differing residualization rates[30] and do not overlap spectrally (Figure 2-1).

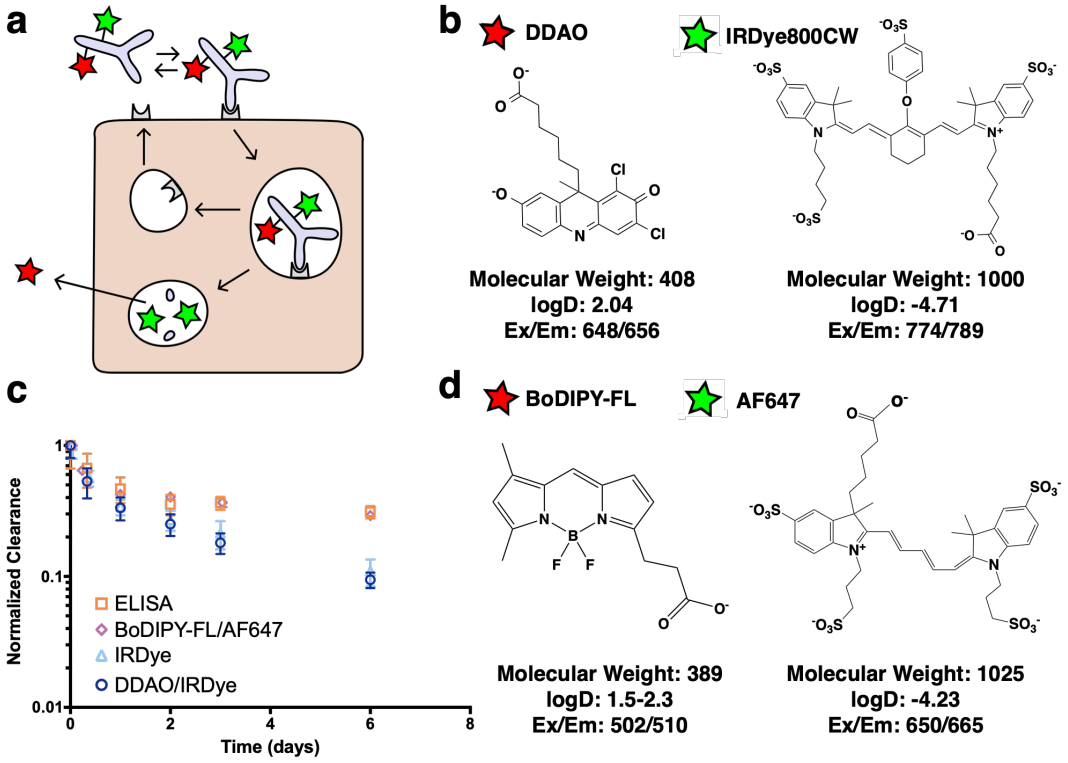

Figure 2-1. Dual label near-infrared (NIR) fluorescence imaging technique concept

(a) Graphic depiction of dually labeled antibody binding the cell, internalizing, and degrading. The non-residualizing DDAO (red star) leaks out of the cell following protein degradation, while the residualizing IRDye (green star) is trapped. (b) DDAO and IRDye dye chemical structures, molecular weights, maximum excitation/emission, and logD (pH 7.4) calculated by MarvinSketch. (c) The plasma concentration over time of trastuzumab-IRDye, dually labeled (DDAO/IRDye or BoDIPY-FL/AF647) trastuzumab and trastuzumab (Ab, measured by ELISA). Trastuzumab DDAO/IRDye is cleared at the same rate when compared to trastuzumab-IRDye800 (which is equal to unlabeled trastuzumab over 3–4 days). The impact of BODIPY-Fl and AF647 is negligible over 6 days. (d) Structure and optical properties for AF647 and BoDIPY-FL with BoDIPY-FL. DoL, degree of labeling.

In this work we discuss two spectrally compatible fluorescent dye pairs IRDye800CW/DDAO and AF647/BoDIPY-FL. (The non-residualizing dye Atto-740 did not have

adequate stability *in vivo* in our hands for reliable measurements.) After the labeled protein binds to a surface receptor, it is internalized, and subsequently degraded. Low molecular weight degradation products labeled with DDAO/BoDIPY-FL and IRDye/AF647 are released. The low molecular weight, lipophilicity, and moderate pKa allow non-residualizing dyes (DDAO/BoDipy-FL) to passively diffuse out of the cell upon protein degradation, while the larger, highly charged, hydrophilic residualizing dyes (IRDye/AF647) remain trapped in lysosomes (Figure 2-1B). DDAO/BoDIPY-FL therefore approximates the intact protein, since it is cleared upon degradation, while IRDye/AF647 approximates the cumulative uptake in the cell, since it is 'trapped' within the cell. This method was chosen over alternative mechanisms, such as pH effects[37] or quenching/FRET, because it is irreversible (unlike pH effects) and does not require a high degree of labeling or larger dye-quencher conjugate. Antibodies can be labeled with IRDye800CW/AF647 while having a negligible impact on clearance over the first few days[38], and the additional DDAO/BoDIPY-FL label does not change the clearance (Figure 2-1C). Previously, the dual technique was applied to the ADC T-DM1[13]; to further demonstrate the utility of this technique we applied it to three other model compounds with widely differing internalization rates (Figure 2-2). EGF is rapidly internalized and degraded with a 17 minute half-life[39], cetuximab and T-DM1 are slower at approximately 2 and 6 hour half-lives, respectively[39, 40], and the tight-junction associated A33 target and antibody is the slowest with a 56 hour half-life[41]. (Note that EGF and cetuximab both target the same receptor, highlighting how the protein and receptor both influence the overall internalization rate.)

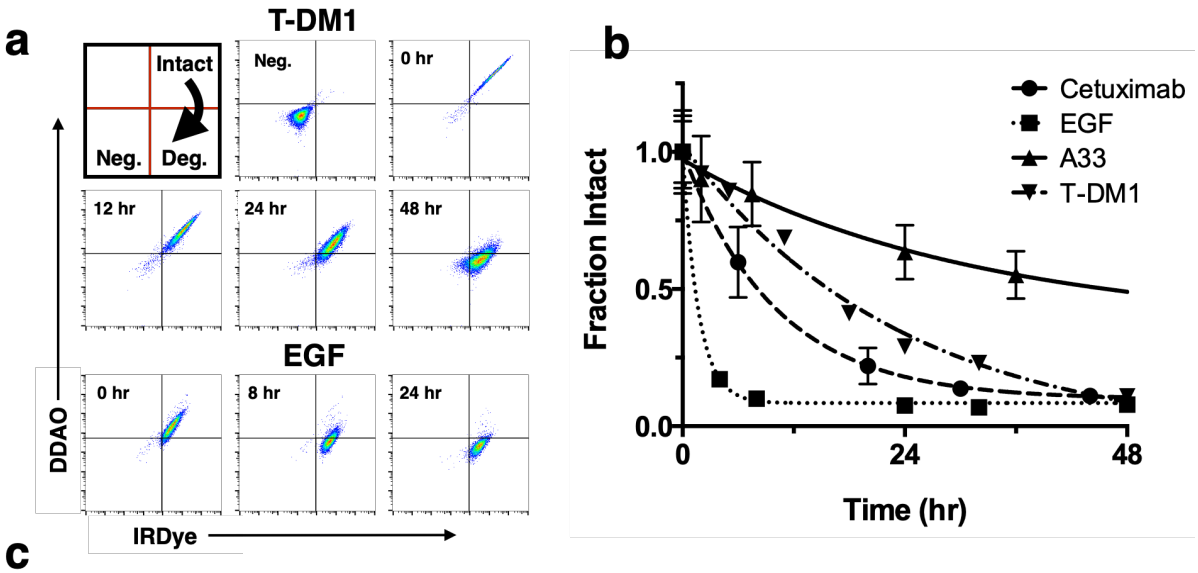

c

Agent	MW (kDa)	Cell Line	Receptors/ Cell	Internalization Half-life
EGF	6.4	A431	4×10^6	17 min
cetuximab	152	A431	4×10^6	1.7 hr
T-DM1	149	NCI-N87	2×10^6	5.8 hr
anti-A33	150	LS174T	5×10^5	56 hr

Figure 2-2. In vitro flow cellular degradation

(a) Representative Log-Log flow cytometry plots of dually labeled T-DM1 and EGF gated on cells. Intact protein appears in the DDAO(+)/IRDye(+) quadrant. Over time as the biologic is degraded, there is a gradual shift towards DDAO(-)/IRDye(+). (b) Fraction of intact protein for four agents over time. EGF shows rapid internalization and degradation, while A33 maintains signal over several days. Cetuximab and T-DM1 decrease at a moderate rate as expected. (c) Model system for validation of dual channel technique. For each model protein the molecular weight and plasma clearance is listed. The associated cell line used for xenografts, receptor density, and internalization half-life.

To demonstrate application of the method with several biologics *in vitro*, T-DM1[13], cetuximab, and A33 were dually labeled with DDAO and IRDye, while a 1:1 ratio of EGF-DDAO to EGF-IRDye was used. Figure 2-2A shows example flow cytometry plots at various times for T-DM1 and EGF following a 30-minute cell labeling. As protein is degraded, the DDAO/IRDye ratio decreases as the intact signal approaches zero. In Figure 2-2A the intact protein appears in the DDAO(+)/IRDye(+) quadrant and, as it is gradually degraded, shifts to DDAO(-)/IRDye(+). To

measure the intact fraction, the cells were analyzed on flow cytometry and the median fluorescence intensity for each channel (DDAO and IRDye) was measured at different times (Figure 2-2B). Then each channel was normalized to the initial time point, and the fraction intact was calculated from the DDAO to IRDye ratio. This value yields the approximate ratio of intact protein to cumulative uptake. EGF showed rapid internalization and degradation, cetuximab and T-DM1 were degraded at a moderate rate, and A33 maintained strong signal over several days. These degradation rates agreed well with the internalization half-lives of these proteins (Figure 2-2C)[39-41].

To visualize the dual label technique *in vitro*, cells were imaged using a confocal microscope at similar time points. Figure 2-3(A-D) shows separate and merged channels for DDAO (red) and IRDye (green) for EGF, A33, Cetuximab, and T-DM1. All four agents showed similar behavior but differed in the time scale for degradation (which matched flow cytometry, Figure 2-2). IRDye signal is initially at the surface but as the protein is internalized and degraded, it becomes trapped in endosomes and lysosomes, resulting in the formation of punctate spots[30]. Similarly, DDAO labels the surface initially; however, as it is degraded, the dye leaks out of the cells as seen by a drop in signal. Although DDAO does lose some fluorescence due to pH effects (pKa = 5)[42], lysed cells show very low levels of DDAO within the cell lysate indicating that the loss of the DDAO dye from the cell dominates over pH effects[30]. The ability to detect protein degradation with the BoDIPY-FL/AF647 dye pair was also tested with several antibodies. Cetuximab, T-DM1, and Trastuzumab all displayed a rapid drop in non-residualizing fluorophore (Bodipy-FL, red) and endosome/lysosome trapped residualizing fluorophore (AF647, green) for these systems (Figure 2-3 E-G).

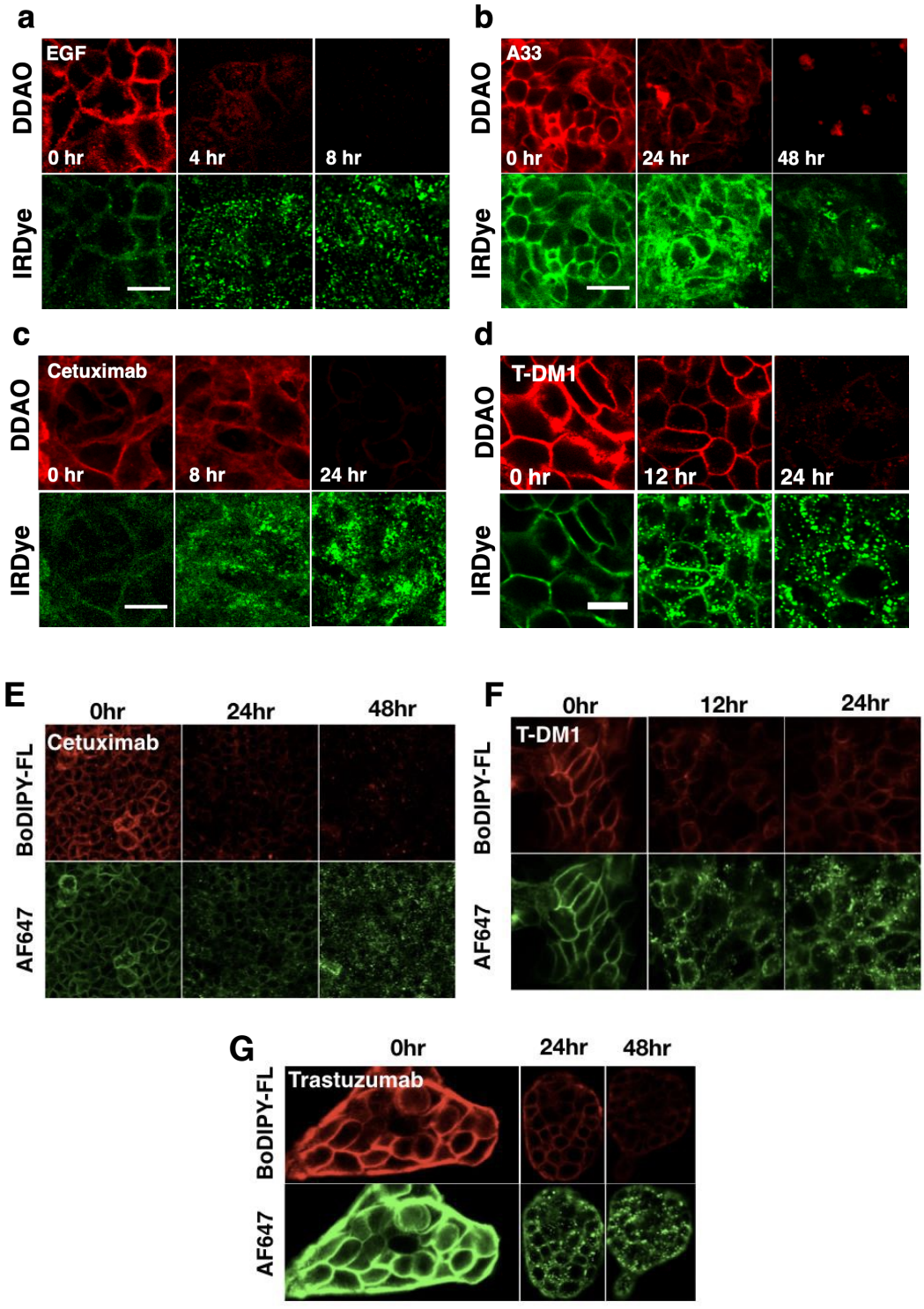

Figure 2-3. In vitro confocal microscopy of dually labeled proteins

(a) EGF, (b) A33, (c) Cetuximab, and (d) T-DM1. DDAO (red) shows cell surface labeling with a loss of signal over time. IRDye (green) shows initial cell surface labeling followed by the formation of punctate spots as it is trapped in the lysosomes. Scale bar is 10 μm. E-G display similar trends for BoDIPY-FL as a non-residualizing fluorophore and AF647 as a residualizing fluorophore.

Applying the dual NIR labeling technique (DDAO/IRDye) to EGF, T-DM1, and cetuximab *in vivo* yielded insight into the single-cell and tissue distribution of these proteins *in vivo* (Figure 2-4). For example, the clinical dose of T-DM1 (3.6 mg/kg) does not fully penetrate the tumor tissue[10, 13, 38] and only targets approximately 10% of cells by flow cytometry[13]. This penetration depth did not change after 7 days[38] indicating that the therapeutic drug likely never reaches all the tumor cells. However, T-DM1 is clinically approved and effective in breast cancer, indicating that despite this heterogeneity, it still shows a clinical response.

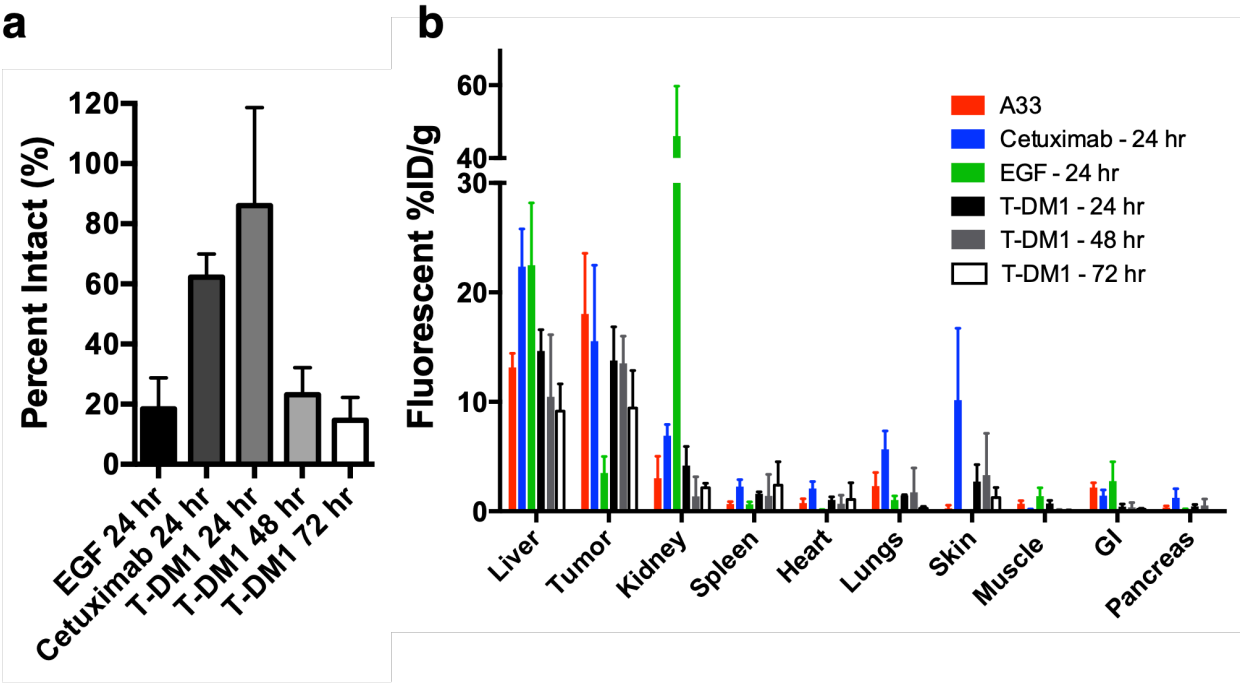

Figure 2-4. In vivo cellular degradation and distribution

(a) T-DM1, EGF, and cetuximab degradation in tumor cells. At 24 XAb EGF (a rapidly clearing protein), is mostly degraded in the tumor. However, the slowly clearing cetuximab and T-DM1 show mostly intact protein. Over 48–72 XAb, after maximum uptake is reached, T-DM1 is increasingly degraded. Data plotted as mean ± standard deviation. (b) Fluorescence biodistribution of EGF, cetuximab, and A33 at 24 XAb and T-DM1 at 24, 48, and 72 XAb.

Examining the DDAO/IRDye ratio *in vivo* through flow cytometry shows how the systemic delivery of the protein plays an important role in the intact versus aggregate degraded probe. EGF, which is cleared rapidly from the blood (Figure 2-5) and internalized rapidly *in vitro*, shows little intact protein at 24 hours post-injection (Figure 2-4A).

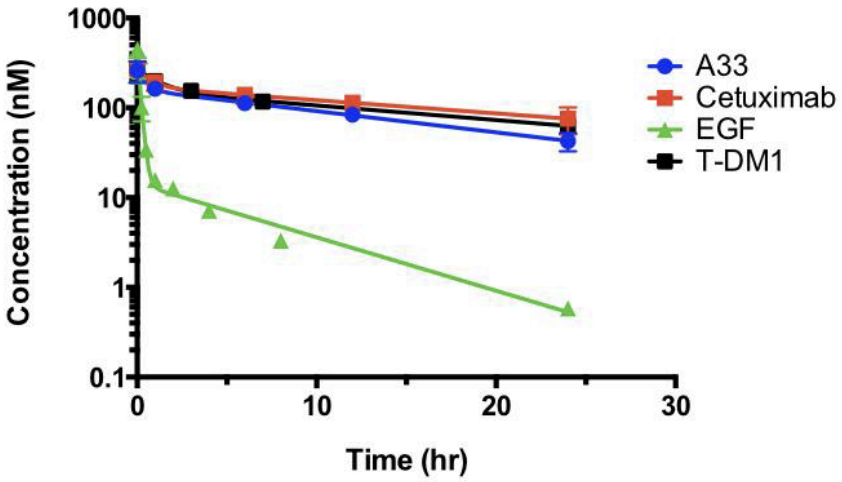

Probe	alpha (hr^{-1})	beta (hr^{-1})	fraction alpha (%)
EGF	6.141	0.14	96.8
cetuximab	1.29	0.03	36.7
A33 MAb	2.08	0.05	39.8
Kadcyla	0.76	0.04	43.1

Figure 2-5. Plasma Clearance for Probe over 24 hours

Biexponential fits were performed using PRISM and the fitted alpha, beta, and fraction alpha parameters are listed

However, the slowly clearing antibodies cetuximab and T-DM1 show mostly intact protein (a ratio of ~1) at 24 hours post-injection (Figure 2-4) from having a constant intact supply from the blood and an initial time to accumulate in the tumor, even though *in vitro* the fraction intact decreased significantly after 24 hours (Figure 2-2B). Only at 3 days, once the plasma concentration is lower and after maximum tumor uptake (Figure 2-5), is the majority of the ADC degraded (Figure 2-4B) corresponding to maximum payload release. Understanding these kinetics is crucial for many ADCs since they only release their toxic payload after degradation, and cell trafficking is a potential mechanism of resistance[43]. When administering a similar dose of dually labeled cetuximab (100 µg, ~4 mg/kg), fluorescence microscopy shows the tumor distribution is

heterogeneous and perivascular in A431 tumor xenografts (Figure 2-6A). As expected, the small protein EGF, which is below the renal filtration cutoff and accumulates in the kidneys (Figure 2-4B) localized in the renal cortex (Figure 2-6B). For smaller therapeutic proteins, the dual label technique can track the distribution in the kidneys, an important clearance organ.

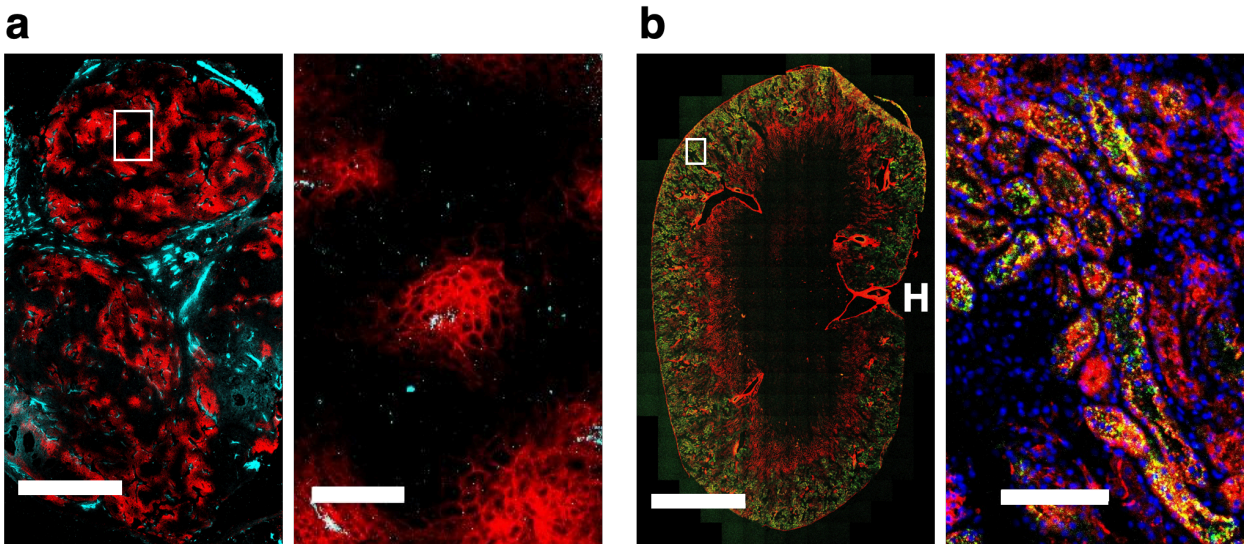

Figure 2-6. Whole organ immunofluorescence histology

(a) High resolution images of A431 xenograft frozen sections 24 XAb post-injection of 100 µg (~4 mg/kg) of dual labeled cetuximab (DDAO, red). Sections were stained with anti-CD31-AF488 (cyan) ex vivo. Left scale bar is 1 mm and right is 100 µm. (b) High resolution images of kidney frozen sections 24 XAb post-injection of EGF-DDAO (red) and EGF-IRDye (green). High magnification sections were stained with Hoechst 33342 (blue) ex vivo. Left scale bar is 2 mm and right is 100 µm. XAb = hilum of kidney.

2.5 Discussion

The complex pharmacokinetics and pharmacodynamics of biologics requires a detailed understanding of the distribution in animal models to better translate results to the clinic. Currently there is a wide array of tools used to study protein distribution at multiple length scales[20]. For example, basic measurements of plasma clearance can be determined using radiolabels, fluorescent labels, ELISA, and mass spectrometry to give blood concentration over time. Using radioactive labels and/or nuclear imaging, the organ uptake and whole animal distribution can be measured in the form of percent-injected dose per gram measurements as well as real time imaging with

PET/SPECT. Histology can be performed using autoradiography, immunohistochemistry, and immunofluorescence to understand the tissue scale distribution. Flow cytometry and *in vitro* measurements are used to quantify fluorescence at the single cell scale. However, these methods have several limitations. Biochemical and biophysical techniques, such as ELISA and mass spectrometry, have limited spatial resolution (ELISA) and/or difficulty in measuring low concentration proteins in complex samples (e.g. mass spectrometry imaging). Radiolabels cannot achieve cellular and subcellular resolution and are more cumbersome to use than fluorescent labels due to radioactive half-life time constraints and safety/licensing issues. Immunohistochemistry has a limited ability to measure cellular kinetics, and most immunofluorescence techniques only measure intact protein, meaning the cumulative degradation of a therapeutic cannot be quantified. The residualization properties of other visible light dyes, such as FITC, have been used to study protein degradation[25]; however, the greater autofluorescence in this region of the visible spectrum can reduce sensitivity for organ biodistribution and *in vivo* imaging. None of these methods are capable of measuring cellular kinetics *in vivo*, and a combination of different techniques with several animals is needed to obtain data on all the relevant length scales.

A major strength of this dual-labeled fluorescence technique (Fig. 2-1) over conventional nuclear imaging is the ability to readily quantify protein uptake with single cell resolution and absolute quantification (proteins per cell) *in vivo* using flow cytometry. Although techniques with radiolabeled probes are approaching the single cell level[44], the path length of the positron and/or imaging equipment intrinsically limits the resolution. Also, with therapeutic proteins and antibodies, the *in vivo* rate of degradation is a critical design characteristic[45]. The rate at which the protein is degraded *in vitro* and *in vivo* determines how long the active intact protein can achieve

its therapeutic effect on the cell surface and in endosomes[46], or, in the case of ADCs, the small molecule (i.e. payload) release rate.

Applying the dual label technique to our model proteins *in vitro* showed differences in cellular uptake and degradation as quantitated through flow cytometry (Figure 2-2) and visualized through fluorescence microscopy (Figure 2-3). By flow cytometry the intact fraction of protein, or degradation rate, was measured and agreed well with other reported internalization rates of the proteins (Figure 2-2B&C). Specifically, the rapidly internalized EGF had the fastest degradation rate, followed by cetuximab, T-DM1, and anti-A33. Visualizing the technique *in vitro* through fluorescence microscopy agreed with these results (Figure 2-3). Examining the cell lysates by gel electrophoresis confirmed that the proteins were degrading over time and lysine-IRDye adducts were released.

In vivo, we used the dual label technique to study protein distribution from cellular to organ scale, as well as cellular scale tumor degradation. When T-DM1 was administered at the clinical dose of 3.6 mg/kg we previously found that only around 10% of cells in the tumor were targeted with ADC[13]. Additionally, we found that maximum T-DM1 uptake in the tumor was reached around 24 hours post injection (Figure 2-4B), indicating most of the tumor did not receive therapeutic. Examining the cells targeted by the ADC showed that most ADC in the tumor was still intact 24 hours post injection. Only after 48 and 72 hours was most of the ADC in the tumor degraded (Figure 2-4A) corresponding to toxic DM1 payload release. Similarly, the slowly clearing cetuximab was mostly intact 24 hours post administration (Figure 2-4A) and exhibited a highly heterogeneous distribution in A431 tumor xenografts (Figure 2-6A). EGF, which is cleared

more quickly than the antibodies and is rapidly internalized (Figure 2-2B), was mostly metabolized in the tumor by 24 hours (Figure 2-4A) and localized to the cortex in the kidney (Figure 2-4D, Figure 2-6B). Taken together, these examples show how dually-labeled biologics can provide systemic (plasma) clearance data, organ biodistribution, tissue-level heterogeneity, and single-cell uptake measurements.

The current method has several limitations and potential areas for improvement. Similar to radiolabeling, NIR fluorescence measures the distribution of the dye and not the protein itself[47]. These dyes could be subject to drug transporters following degradation and release, similar to small molecule drugs and ADC payloads. Excessive surface labeling with fluorophores can change the physicochemical properties of the protein, thereby changing the plasma clearance and/or distribution[48, 49]. Although significant differences in plasma clearance do not occur at early times for several antibodies that have been tested[50], following the antibodies over days to weeks can result in faster clearance rates[38]. For longer PK studies, we previously found that the clearance of antibodies singly labeled with AF680 at a dye to protein ratio of 0.3 or less was similar to unlabeled; however, the single label does not have the ability to discriminate intact from degraded protein. Therefore, the dual label technique is better suited for shorter studies. As with negatively charged and/or radiolabeled antibodies[51, 52], care must be taken to not over-label the protein. In this study, the degree of labeling was kept very low, around 0.3 for IRDye and 0.7-1.0 for DDAO to minimize the impact of the dyes and better approximate the true protein distribution[34, 38]. Basic quality control measures must be performed to ensure the labeling efficiency, lack of free dye, and no loss in binding affinity. Finally, the fluorescence intensity of DDAO was not large enough to measure the bulk organ biodistribution accurately. DDAO was selected based on its rapid washout

rate from cells following degradation[30]. However, its optical brightness is lower than the cyanine-based dyes. The IRDye signal is much higher than the background at this wavelength, but for DDAO, the higher 650 nm autofluorescence and lower dye brightness results in low signal. Specifically, the trends behaved as expected in the homogenized organs (e.g. the ratio of DDAO to IRDye was low in the kidney of mice injected with EGF), but the contrast to noise ratio was too low for useful bulk measurements. The DDAO signal is therefore limited to flow cytometry and fluorescence microscopy of cells and tissues.

The use of a residualizing dye is helpful to quantify the total payload uptake when studying the cellular distribution of ADCs. However, it is important to note that the non-site specific lysine conjugation chemistry provides a 'bulk' measurement of protein degradation. While this is useful for some applications, such as ADCs with non-cleavable linkers like T-DM1 that require whole antibody degradation, ADCs that utilize cleavable linkers may require specific labeling chemistries to mimic the linker cleavage. Designing surrogate fluorescent linkers can provide a direct measure of linker cleavage in real-time[53].

The organ-level biodistribution using a residualizing NIR fluorescent label matches the values used in radiolabeling[54]. However, the method is more labor intensive (e.g. organ homogenization) and less sensitive than radiolabeled biodistribution measurements. As mentioned above, the DDAO signal was not sufficient to measure the biodistribution for this non-residualizing label. In addition, the high tissue scattering, even with NIR light, results in low resolution whole animal fluorescence imaging. Therefore, radiolabeling is much better suited for measurements solely focused on organ level distribution and/or whole animal imaging.

The sensitivity of the technique (e.g. lowest number of proteins/cell that can be detected) is highly dependent on the equipment used for the experiment. The specific excitation and emission wavelengths and bandwidths, type of detection, optical path properties, etc. all impact the signal to noise ratio (SNR). However, we have included results on these dye pairs due to the relatively common 635 nm (and 488 nm) lasers used in flow cytometry and confocal microscopy. This often results in 647 nm dyes providing high sensitivity. The autofluorescence and variability of blue-shifted dyes (e.g. green-fluorescence) and the often lower quantum yields on common detectors in the NIR range (e.g. beyond 800 nm) can lower sensitivity above and below the wavelengths used for 647 nm dyes. With the equipment used in this work, the limit of detection For IRDye800CW was ~20,000 antibodies/cell, while AlexaFluor 647 was ~5,000 antibodies/cell. This level of sensitivity is needed for some targets given the > 100-fold differences in expression in ADC targets, for example[55]. Because of the spectral overlap of DDAO with the higher sensitivity AF647 dye and instability of Atto740, we selected a visible light dye for a non-residualizing partner. BODIPY-Fl was chosen due to the bright fluorescence and lack of pH effects in the endosomal pathway that are prevalent for fluorescein (pKa ~ 6.4). It also has a substantial spectral separation from AlexaFluor 647 compared to red dyes and can readily be excited by common 488 nm laser lines. However, with an appropriate excitation source and controls for overlap, other visible light dyes that demonstrate high membrane permeability, such as TAMRA[56], may be useful for dual labeling.

2.6 Conclusion

The dual label NIR fluorophore technique provides absolute protein uptake and degradation with single cell resolution *in vivo* using widely available flow cytometry equipment, an achievement currently not possible with other imaging modalities. In addition, it enables multi-scale understanding of distribution in the *same* animal. Antibodies are known to distribute heterogeneously throughout tumors[57, 58], and combined with tumor microenvironment heterogeneity, such as differences in vascularization, macrophage infiltration, and necrosis, and animal-to-animal variability, this can make comparisons between animals especially difficult. In tumors that have differing vascular density, the overall delivery of the antibody will change and could significantly influence the clinical outcome. Using this technique, *in vivo* degradation at the cellular scale and distribution at the cellular, tissue, organ, and whole animal scales is done in the same animal. The combination of flow cytometry data for single-cell degradation and uptake with the tissue distribution better informs how novel protein therapeutics acting at the microscopic scale affect the tissue distribution and ultimate response.

2.7 Experimental Methods

Cell Culture and Animals

A431, NCI-N87, and LS174T cells were cultured 2-3 times per week up to a maximum passage number of 50 and grown in RPMI 1640 or DMEM supplemented with 10% (v/v) FBS, 50 U/mL penicillin, and 50 μg/mL streptomycin at 37°C with 5% CO_2 based on ATCC recommendations. Annual use of the Mycoalert Testing Kit (Thermo Fisher Scientific, NC9719283) confirmed the absence of mycoplasma. All animal studies were approved and conducted in compliance with the Institutional Animal Care and Use Committee (IACUC) of the

University of Michigan and Association for Assessment and Accreditation of Laboratory Animal Care International (AAALAC). Pharmacokinetic and *in vivo* tumor distribution animal studies were conducted in 4–6 week old homozygous female nude (RRID: 2175030, Foxn1nu/nu, Jackson Laboratories) mice. For *in vivo* tumor distribution and growth studies, the nude mice were inoculated in the flank with 1×10^6 cells in Matrigel (Fisher Scientific, CB40234A).

Plasma Clearance

The impact of dye conjugation on the observed pharmacokinetics was measured via blood sampling. At each timepoint, 10µL of blood was collected via retro-orbital blood sampling and added to 15µL of PBS-EDTA (10mM). The mixture was centrifuged at 3000xg for 1 minute and then 18µL of supernatant (Plasma) was collected and stored at -80°C until all samples were collected. After completion of blood sampling, samples were thawed and scanned on the Odyssey CLx scanner or Biotek plate reader. Fluorescent values were normalized to the 1-minute time point for individual mice to determine the relative impact of dye conjugation on plasma clearance.

Protein Fluorophore Conjugation

All proteins were conjugated via NHS ester reaction chemistry. Proteins (>2mg/ml) were buffered with 10% (v/v) sodium bicarbonate (7.5% in PBS) to slightly increase pH of reaction for optimal labeling. Dyes were added in molar ratios approximately 1.5-2x the desired degree of labeling (e.g. 0.5 molar ratio to achieve 0.3 DoL). Reactions reached completion at 4 hours and were then purified using P-6 Biogel. Briefly, 800µL of P-6 Biogel was added to a Costar Spin-X column and centrifuged at 3500xg for 1 min. The filtrate (PBS) was removed and 100µL of reaction mixture was added to the top of the column. The column was centrifuged for 1 min at

3500xg and the purified protein fluorophore conjugate was collected. The protein was then confirmed to be pure after running the purified protein on an SDS-PAGE gel and scanning the gel on the Odyssey CLx.

Degradation Assay In Vitro

Cells were stripped from culturing flasks and plated in 96 well plates (for flow cytometry) and in 8 well chamber slides (for microscopy) at ~90% confluency then allowed to adhere to the plate overnight. During the experiment, media was replaced daily to reduce buildup of fluorescent byproducts. At each timepoint 40nM dual labeled protein solution at a volume of 100µL for 96 well plate or 300µL for chamber slides was incubated for 30 minutes at 37°C. The incubated wells were then aspirated and washed 2x with complete media and then the media was replaced. After the final timepoint, all cells were washed 1x with complete media and then 1x with PBS to remove all fluorophore that had leaked out of the cell. The chamber slides were then immediately imaged on a confocal microscope while each well of the 96 well plate was incubated in 100µL of 0.05% Trypsin-EDTA until cells were detached (~10 min). Cells were gathered from each well and subsequently washed 2x with PBS/BSA before resuspending in PBS, passing through a 40µm filter to remove cell clumps, and running on the Attune flow cytometer.

Degradation Assay Ex Vivo

Once tumor xenografts reached a volume of ~300-500mm^3, 3.6 mg/kg of dual labeled T-DM1 was injected via tail vein. Mice were sacrificed at 24, 48, or 72 hours after injection and the tumor was resected. The tumor was cut into small pieces and then incubated in 5 ml of 5 mg/ml collagenase IV-PBS solution for 25 min at 37°C. After incubation, 5 ml of RPMI 1640 complete

media was added to the cell suspension, the cells were pelleted at 300xg for 5 minutes and the supernatant was removed. The cell pellet was resuspended in PBS and passed through a 40μm filter to remove clumped cells then analyzed on the Attune flow cytometer.

Chapter III

Increased Tumor Penetration of Single-Domain Antibody Drug Conjugates Improves In Vivo Efficacy in Prostate Cancer Models

3.1 Publication Information

Nessler, I., Khera, E., Vance, S., Kopp, A., Qiu, Q., Keating, T.A., Abu-Yousif, A.O., Sandal, T., Legg, J., Thompson, L., Thurber G.M. Increased Tumor Penetration of Single-Domain Antibody Drug Conjugates Improves In Vivo Efficacy in Prostate Cancer Models. Cancer Res (2020).

Modifications have been made to the published document to adapt the content to this text. The previous chapter identified multiple NIR fluorescent labels that could be used to monitor PK as well as tumor uptake and distribution. This chapter builds on the previous work by applying the generated methods to proteins of various size and features to identify key protein characteristics in tumor efficacy.

3.2 Abstract

Targeted delivery of chemotherapeutics aims to increase efficacy and lower toxicity by concentrating drugs at the site-of-action, a method embodied by the five current FDA approved antibody-drug conjugates (ADCs). However, a variety of pharmacokinetic challenges result in relatively narrow therapeutic windows for these agents, hampering the development of new drugs.

Here, we use a series of PSMA-binding single-domain (Humabody®) ADC constructs to demonstrate that tissue penetration of protein-drug conjugates plays a major role in therapeutic efficacy. Counterintuitively, a construct with lower *in vitro* potency resulted in higher *in vivo* efficacy than other protein-drug conjugates. Biodistribution data, tumor histology images, spheroid experiments, *in vivo* single-cell measurements, and computational results demonstrate that a smaller size and slower internalization rate enabled higher tissue penetration and more cell killing. The results also illustrate the benefits of linking an albumin binding domain to the single-domain antibody drug conjugates. A construct lacking an albumin binding domain was rapidly cleared leading to lower tumor uptake (%ID/g) and decreased *in vivo* efficacy. In conclusion, these results provide evidence that reaching the maximum number of cells with a lethal payload dose correlates more strongly with *in vivo* efficacy than total tumor uptake or *in vitro* potency alone for these protein-drug conjugates. Computational modeling and protein engineering can be used to custom design an optimal framework for controlling internalization, clearance, and tissue penetration to maximize cell killing.

3.3 Background

Antibody Drug Conjugates (ADCs) have opened a new field of targeted therapeutics based on 'hybrid' drugs combining desirable targeting properties of biologics with the potency of small molecule cytotoxic payloads. For ADCs, the protein carrier is typically a monoclonal antibody that specifically binds to a target antigen expressed on cancer cells, increasing the delivery of the small molecule payload to the site of action *in vivo*. To date, five ADCs have been FDA approved[5, 59], with a large pipeline of >70 in clinical trials. However, one drawback of antibodies is slow tumor penetration. The tumor uptake of antibodies is limited by their extravasation rate, and they tend to

penetrate only a few cell layers outside of blood vessels due to their rapid antigen-binding rate relative to intratumoral diffusion[8, 9]. In the clinic, unconjugated antibodies are often well tolerated, such that they can be delivered at very high doses that saturate receptors on cell layers closer to the blood vessel, enabling the antibody to diffuse farther through the tumor. However, the payload toxicity of ADCs limits the dose and frequency of administration, restricting tumor penetration depths and allowing regrowth between doses (typically given every 3 weeks for current therapies)[7]. Therefore, devising design and treatment strategies that increase tumor penetration may yield greater efficacy and improve clinical success rates for ADCs and other protein-drug conjugates.

Previous work based on co-administration of trastuzumab with the ADC T-DM1 (ado-trastuzumab emtansine) demonstrated that higher tissue penetration could yield better efficacy in a mouse model of HER2 positive cancer[13]. Based on a literature review of studies involving ADCs with a range of drug-to-antibody ratios (DAR)[10], ADCs that delivered the same payload dose at a lower DAR (i.e. higher protein doses) generally yielded an increase in efficacy in animal models with moderate to high expression, likely as a result of better tissue penetration[60]. Although bystander effects can help mitigate transport challenges by allowing the payload to diffuse deeper into the tissue following release from the protein, analysis of literature data and predictive simulations indicated that higher tissue penetration is more efficient at improving efficacy even when using bystander payloads[60]. When the ADC is more uniformly distributed, the same total amount of cytotoxic payload delivered to the tumor is spread more homogeneously, so cells adjacent to vessels that receive an overdose of payload with heterogeneous ADC distribution now receive fewer payloads. Therefore, implicit in this approach is that the amount of payload delivered per cell exceeds the intrinsic potency of the payload, thereby maintaining a lethal cellular dose

while increasing penetration to reach more cells. Based on these and other results[61], tumor tissue penetration is critical for the overall efficacy of ADC treatment and should be analyzed when optimizing protein-drug conjugates for maximum effectiveness.

Besides increasing the dose or co-administering the ADC with unconjugated antibody, there are protein engineering approaches to develop scaffolds for improved tissue penetration[62-65]. This may be particularly advantageous for highly expressed targets that would require very large antibody doses to saturate the tumor or for targeting metastases with varying expression levels. Reducing affinity is one method of increasing tissue penetration[66]. However, for large, bivalent IgGs, the intrinsic affinity of each Fab arm must be very low to penetrate tissue with highly expressed antigens (e.g. 270 nM K_d)[67]. Instead, lower molecular weight proteins can penetrate tissue farther before being immobilized through target binding[68] because of their faster diffusion coefficient (which is the dominant mode of transport in tumors due to elevated interstitial pressure[69]). Some smaller scaffolds are already being tested in the clinic, such as caplacizumab - a bivalent single-domain antibody (~30kDa) used to block platelet aggregation[70], providing precedent for these formats. A major limitation for these smaller scaffolds is their rapid renal clearance[62, 71, 72]. However, fusion to albumin binding domains can extend plasma half-life and avoid glomerular filtration by increasing the effective molecular weight while still enabling better tissue penetration[73-77].

Humabodies are fully human, single heavy chain variable (V_H) domains generated using Crescendo Biologics' proprietary transgenic mouse platform. The Crescendo mouse generates variable heavy-chain-only antibodies, comprising human germline V_H domains, in a background

where all three endogenous antibody loci (heavy chain, κ light chain and λ light chain) are functionally silenced. This *in vivo* maturation in the absence of light chains results in fully human V_H domains with high target affinity, desirable biophysical properties (e.g. stability), and eliminates the necessity for subsequent humanization steps. As the use of alternative molecular formats for multi-specific antibodies grows[78], the small size (~15 kDa), absence of light-chain pairing, and excellent developability characteristics makes Humabodies highly amenable building blocks for generating a large array of mono- and multi-functional therapeutics. These multi-V_H domain Humabodies can be designed with a range of functionality for optimal target engagement to improve therapeutic benefit, while still retaining the advantages of small protein therapeutics.

In this work we investigated the tumor tissue pharmacokinetics and efficacy of 3 different PSMA-binding single-domain antibody (Humabody) drug conjugates and an IgG drug conjugate (referred to collectively as antibody drug conjugates or simply antibodies/antibody constructs if no drug is present). The first antibody construct (V_{H1}-HLE, MW = 31.1 kDa) consists of a monovalent PSMA binding domain (V_{H1}) connected via a linker to an albumin-binding domain ('half-life extender,' HLE) resulting in the V_{H1}-HLE construct. The second construct (V_{H2}-V_{H1}-HLE, MW = 44.7 kDa) is a fusion between three domains: two PSMA binding domains to different epitopes (V_{H1} and V_{H2}) conjugated to an HLE domain to yield V_{H2}-V_{H1}-HLE. The third construct (V_{H2}-V_{H1}, MW = 29.7 kDa) is identical to V_{H2}-V_{H1}-HLE except without the HLE domain to compare the impact of different clearance rates. For efficacy/potency studies, these antibody constructs were conjugated via a C-terminal cysteine addition to a potent DNA-alkylating agent (DGN549, an indolinobenzodiazepine DNA-alkylating monoimine[79]). To track the kinetics and distribution *in vitro* and *in vivo*, these antibody constructs were conjugated via a sortase tag to

Alexa Fluor 680, Alexa Fluor 647, or Alexa Fluor 488 near-infrared and visible light dyes. The fluorescent antibody constructs (also referred to as fluorescent antibodies in this paper) were used to determine the overall tumor uptake (%ID/g), tumor tissue distribution, *in vitro* spheroid penetration, and *in vivo* single-cell pharmacokinetics for comparison with the *in vitro* and *in vivo* efficacy. Combined with a computational model, these results demonstrate that smaller monovalent protein scaffolds can increase tissue penetration enhancing *in vivo* efficacy in mouse models of prostate cancer.

3.4 Results

The *in vitro* toxicity of DU145-PSMA cells was measured after 6 days using a PrestoBlue viability assay (Figure 3-1). V_{H1}-HLE-DGN549 had the lowest potency, followed by both V_{H2}-V_{H1}-HLE-DGN549 and V_{H2}-V_{H1}-DGN549. The J591-DGN549 ADC had the highest potency based on protein concentration, likely due to the multiple payloads per antibody, Figure 3-3A. Potency based on *payload* concentration was similar for V_{H2}-V_{H1}-DGN549, V_{H2}-V_{H1}-HLE-DGN549, and J591-DGN549 (Figure 3-1B). These results are consistent with the internalization rates for these ADC constructs, with the biparatopic Humabodies (V_{H2}-V_{H1}-HLE-AF680 and V_{H2}-V_{H1}-AF680) capable of inducing surface-crosslinking and driving internalization[80] (Figure 3-2), the J591 ADC inducing internalization[81], and V_{H1}-HLE having the slowest cellular uptake.

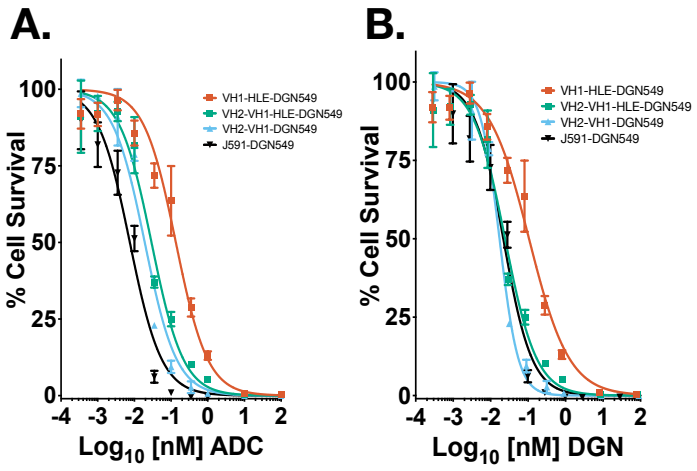

C.

ADC	IC50 (pM Protein)	IC50 (pM DGN549)
VH1-HLE-DGN549	135	106
VH2-VH1-HLE-DGN549	29	24
VH2-VH1-DGN549	19	18
J591-DGN549	8	22

Figure 3-1. In vitro cytotoxicity.

DU145-PSMA cells were seeded at a density of 8,000 cells per well in 96-well plates for cell viability assays. The cell survival was plotted against protein concentration (A) and toxin concentration (B). The measured IC50s are displayed based on protein concentration and toxin concentration (C).

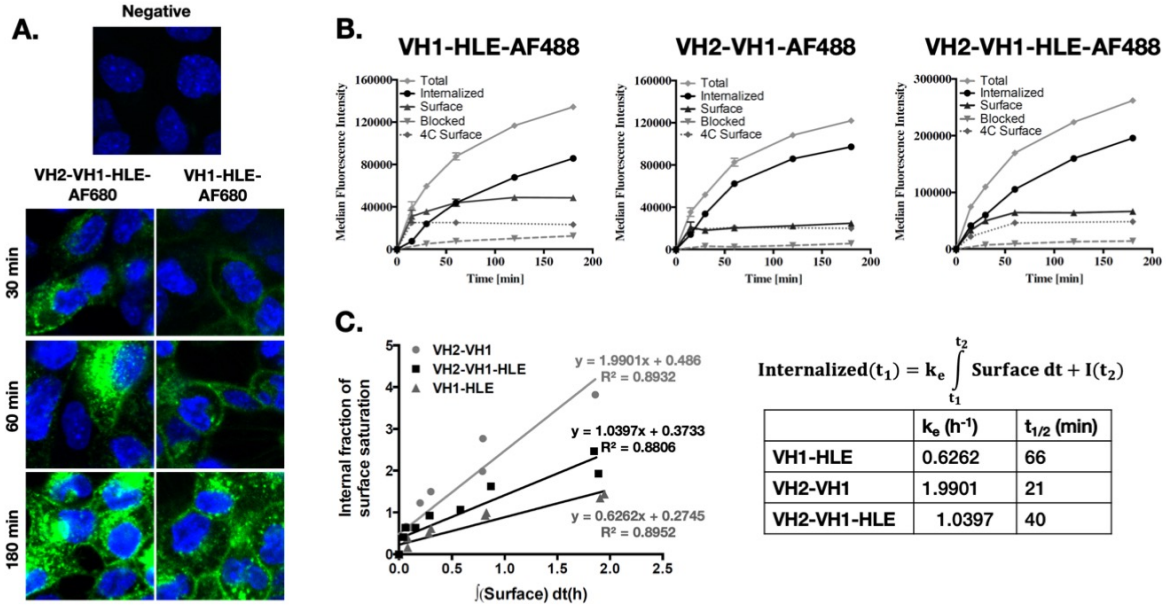

	k_e (h^{-1})	$t_{1/2}$ (min)
VH1-HLE	0.6262	66
VH2-VH1	1.9901	21
VH2-VH1-HLE	1.0397	40

Figure 3-2. Internalization Kinetics.

Internalization rates were measured qualitatively with microscopy (A), and quantitatively through flow cytometry (B). The rate of internalization was then calculated for the three fluorescent Humabodies (C) and was previously measured for J591.

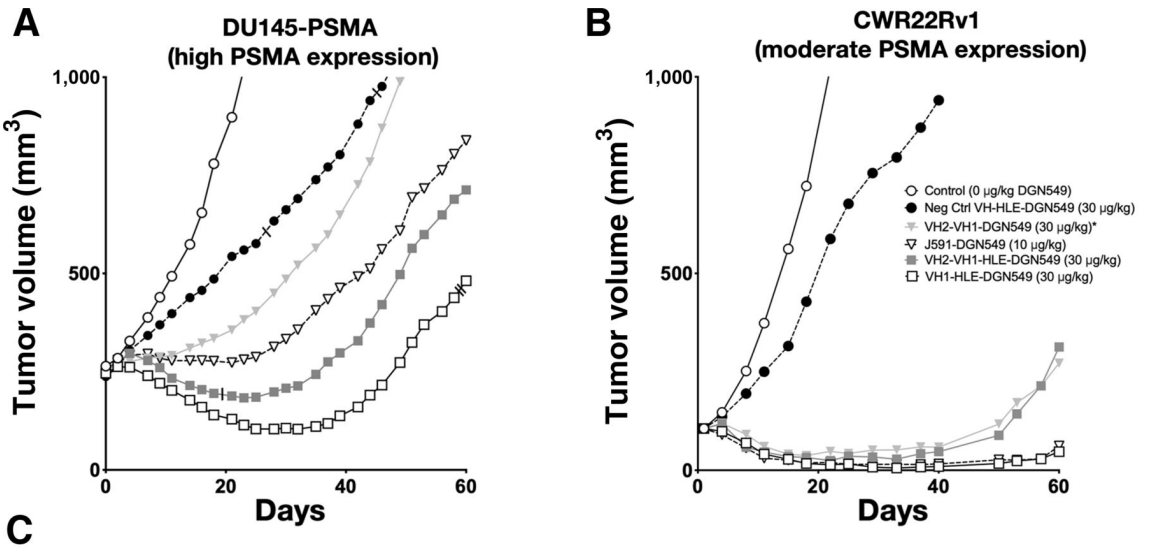

C

Drug	VH2-VH1-HLE-DGN549	VH1-HLE-DGN549	VH2-VH1-DGN549	J591-DGN549
Internalization	Fast	Slow	Fast	Slow
Clearance	Slow	Slow	Fast	Slow
Structure	VH_2-VH_1-HLE-☆	VH_1-HLE-☆	VH_2-VH_1-☆	☆☆☆
IC_{50} (pmol/L protein)	29.3	135.0	19.2	7.5

☆ = DGN549, AF647, or AF680 (HLE) = Albumin-binding domain

Figure 3-3. In vitro and in vivo efficacy of ADCs

A) and B), The ADCs were used in two separate tumor inhibition studies involving nude mice with either a high expression DU145-PSMA xenograft (A) or a moderate-expressing CWR22Rv1 xenograft (B). C, the table displays relative internalization and clearance rates alongside ADC structures (all conjugations occurred at the C-terminus) and the *in vitro* potencies. The IC_{50} for monovalent and biparatopic antibody conjugates with and without an albumin-binding HLE was determined in DU145-PSMA cells. *VH2-VH1-DGN549 was dosed every other day for three total doses at a 10 µg/kg DGN549 per dose for the CWR22Rv1 study and as a single bolus dose of 30 µg/kg DGN5459 in the DU145-PSMA study. Slashes mark mice removed early from the study (Supplementary Methods).

Tumor growth studies done in athymic nude or SCID mice with PSMA-expressing xenografts showed significant growth inhibition for all PSMA-targeted ADCs relative to untargeted controls. In the xenograft model with higher PSMA expression (DU145-PSMA), V_{H1}-HLE-DGN549 shows the greatest efficacy among all experimental groups ($p<0.05$, Figure 3-4G). V_{H2}-V_{H1}-HLE-DGN549 showed better efficacy than V_{H2}-V_{H1}-DGN549 given in a single bolus

dose as a result of V_{H2}-V_{H1}-HLE's prolonged circulation and tumor exposure. Individual DU145-PSMA growth curves for all mice in each treatment group are displayed in Figure 3-4.

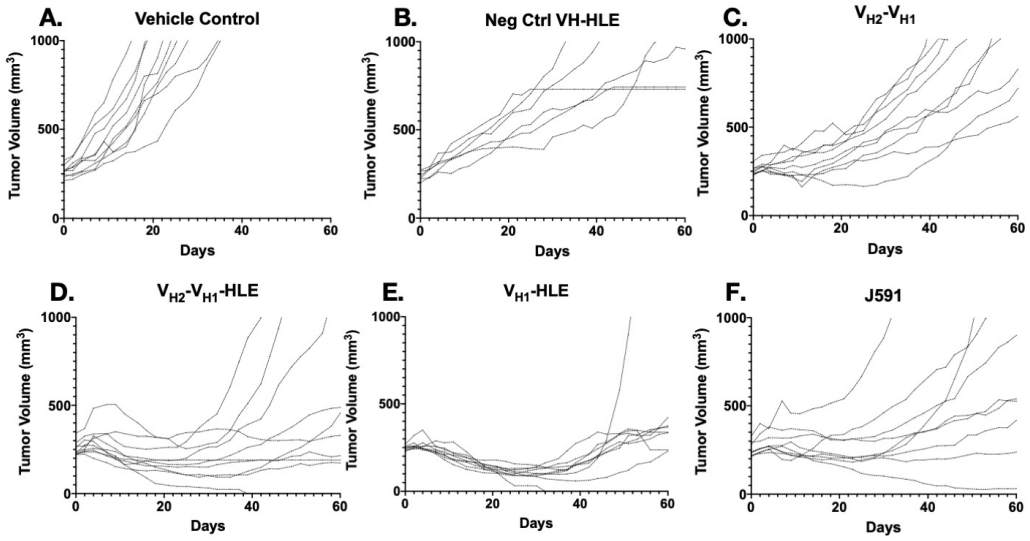

G		V_{H1}-HLE	V_{H1}-V_{H2}-HLE	V_{H1}-V_{H2}	J591
Vehicle Control	Statistically significant?	Yes	Yes	Yes	Yes
	P-value	<0.0001	0.0001	0.0006	0.0002
VH-HLE Neg Control	Statistically significant?	Yes	Yes	Yes	Yes
	P-value	0.0002	0.0002	0.0275	0.0025
V_{H1}-HLE	Statistically significant?	--	Yes	Yes	Yes
	P-value	--	0.025	<0.0001	0.0099

Figure 3-4. Individual tumor growth curves and statistical analysis of tumor growth

Following intravenous administration of ADC construct or control, tumor volumes were measured and plotted for each treatment group in the DU145-PSMA xenograft model: Vehicle control (A), V_H-HLE-DGN549 negative control (B), V_{H2}-V_{H1}-DGN549 (C), V_{H2}-V_{H1}-HLE-DGN549 (D), V_{H1}-HLE-DGN549 (E), and J591-DGN549 (F). (G) An unpaired, two-sided t test with Welch's correlation was used to determine statistical significance at day 25, where the maximum therapeutic effect occurred. All treatment groups (V_{H2}-V_{H1}-DGN549, V_{H2}-V_{H1}-HLE-DGN549, V_{H1}-HLE-DGN549, and J591-DGN549) showed statistical significance compared to non-binding control and vehicle control groups ($p<0.05$). V_{H1}-HLE-DGN549 showed statistical significance compared to all other treatment groups ($p<0.05$).

Overall, tumor growth inhibition was generally lower in the DU145-PSMA tumors compared to CWR22Rv1 xenografts, likely due a combination of the larger starting size (250 vs.

100 mm^3) and higher PSMA expression resulting in greater heterogeneity in intratumoral distribution. In CWR22Rv1 tumors, V_{H1}-HLE-DGN549 and J591-DGN549 were equally effective. Fractionated dosing of the rapidly cleared V_{H2}-V_{H1}-DGN549 in the CWR22Rv1 model to mitigate rapid renal clearance resulted in similar efficacy as the more slowly cleared V_{H2}-V_{H1}-HLE-DGN549, further highlighting the benefit of prolonged exposure. In contrast to the observed trend for *in vitro* potency of the Humabody drug conjugates, V_{H1}-HLE-DGN549 had surprisingly higher efficacy than either V_{H2}-V_{H1}-HLE-DGN549 or V_{H2}-V_{H1}-DGN549 in both tumor models (Figure 3-3B&C). To better understand this effect, a detailed study of the distribution at the systemic, organ, tissue, and cellular level was initiated using near-infrared fluorescence to delineate the contribution of the multiple ADC delivery and processing steps *in vivo* towards efficacy.

To study distribution, fluorescent antibodies were injected into nude mice bearing antigen positive DU145-PSMA cells in the left flank and DU145 (PSMA negative) cells in the right flank. (The clearance of the fluorescent antibodies was similar to non-fluorescent antibody (Figure 3-5C) and ADCs fluorescently labeled via lysine side-chains (Figure 3-5D).The slowly cleared V_{H1}-HLE-AF680, V_{H2}-V_{H1}-HLE-AF680, and J591-AF680 antibody had similarly high tumor uptake in the antigen positive tumor as expected (~30%ID/g) with no statistically significant differences, while the more rapidly cleared V_{H2}-V_{H1}-AF680, had much lower uptake (~7% ID/g), Figure 3-5A. Rapid plasma clearance of V_{H2}-V_{H1}-AF680 also resulted in lower uptake in the antigen negative tumor and all other organs compared to V_{H1}-HLE-AF680, V_{H2}-V_{H1}-HLE-AF680, and J591-AF680 (Figure 3-5B). Because the tumor uptake, plasma clearance, and *in vitro* toxicity did not sufficiently explain the trends in tumor growth inhibition, further studies on the intratumoral distribution of these agents were performed.

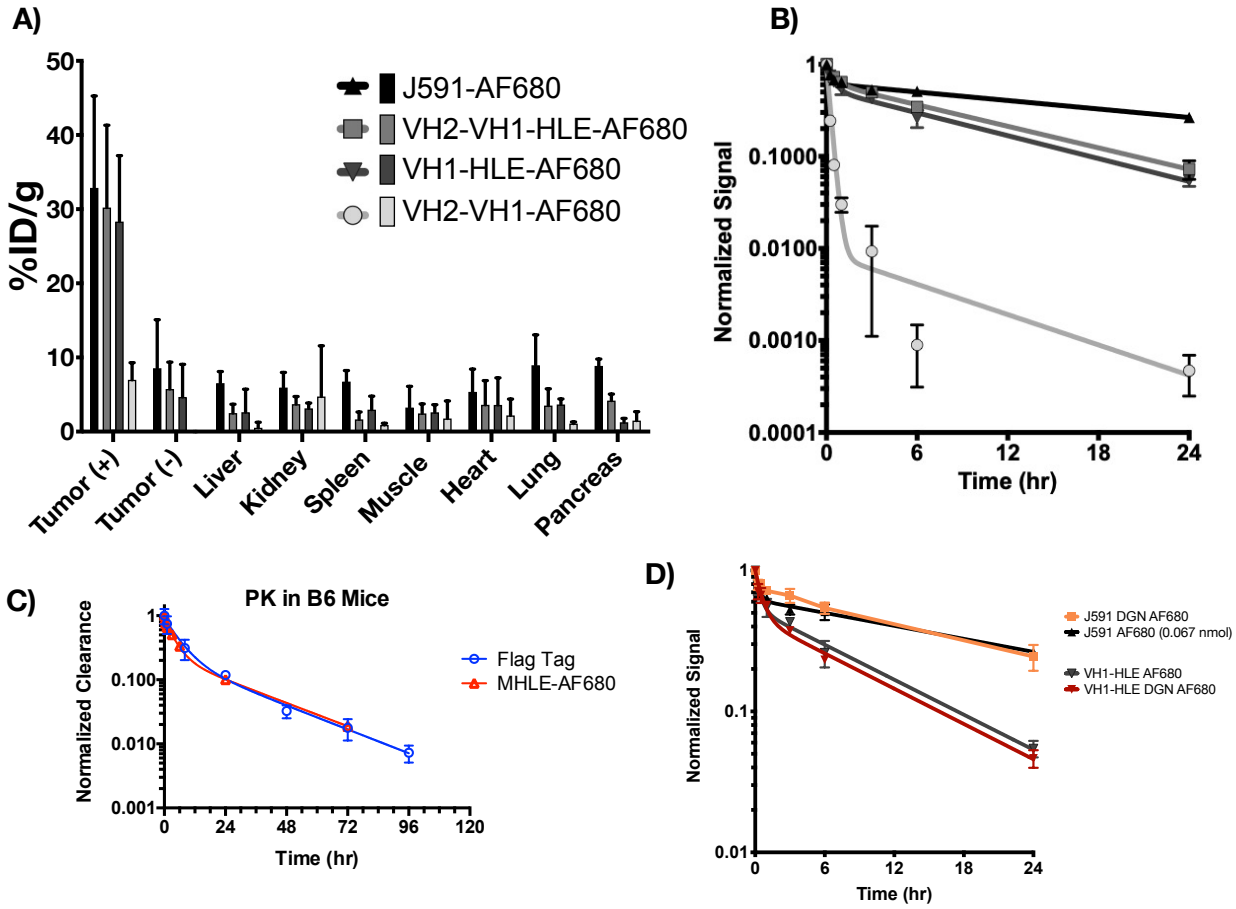

Figure 3-5. Biodistribution and Plasma Clearance of Alexa Fluor 680 Antibody Constructs

The ADC biodistribution %ID/g (A) and Plasma clearance normalized signal (B) are displayed as a mean value with error bars for each conjugate representing standard deviation. Sample sizes were as follows: VH2-VH1-HLE-AF680 (n=5), VH1-HLE-AF680 (n=5), VH2-VH1-AF680 (n=3), and J591-AF680 (n=3). (C) The plasma clearance of V_{H1}-HLE (measured by ELISA via a C-terminal Flag tag) was similar to the fluorescently labeled V_{H1}-HLE-AF680 (measured via fluorescence) in Black 6 mice. (D) The plasma clearance of J591 and J591-DGN (both labeled with AlexaFluor 680 via NHS ester lysine chemistry) were similar in mice. The plasma clearance of V_{H1}-HLE-AF680 (site specifically labeled at the C-terminus) was similar to V_{H1}-HLE DGN (where the DGN payload was site specifically attached at the C-terminus and the AlexaFluor dye was attached via lysines).

Previous work in the literature indicates that smaller protein scaffolds result in higher tissue penetration (e.g. [66, 68, 70, 82]). We adapted the Krogh cylinder model for a spherical geometry and, after gathering parameters on binding kinetics, plasma clearance, and receptor expression, conducted simulations of tissue and spheroid distribution after 24 hours as depicted in Figure 3-6A. The computational model predicted the smaller V_{H1}-HLE would exhibit the greatest tumor penetration, and that the rapidly internalizing V_{H2}-V_{H1} and V_{H2}-V_{H1}-HLE would only target a few

cell layers into the spheroid, similar to the J591 antibody. Notably, this model assumes that the specific, reversible albumin binding of HLE does not reduce the diffusion into tissue in contrast to non-specific albumin sticking from lipophilic agents[83].

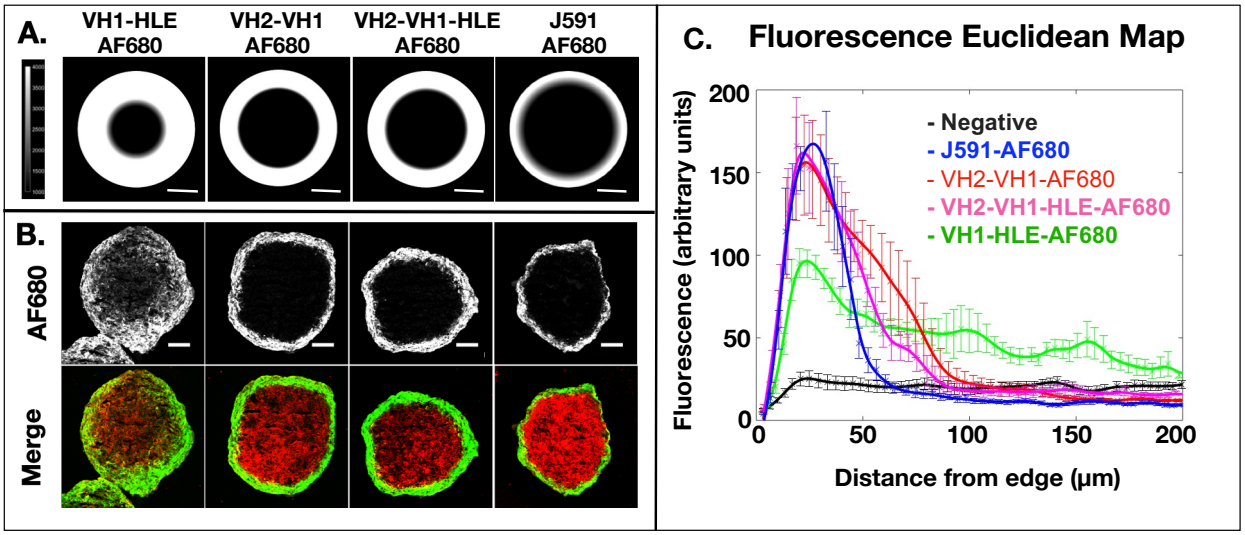

Drug	VH1-HLE AF680	VH2-VH1 AF680	VH2-VH1-HLE AF680	J591 AF680
Kd (nM)	0.9	0.119	0.243	2.5
Kon * 10^5 (1/Ms)	4.03	4.57	1.743	0.153
Internalization half-life (min)	66	21	40	90

Figure 3-6. Computational and Experimental Tissue Penetration of Fluorescent constructs.

Simulations based on the molecular weight, binding kinetics, affinity, and internalization rate predict penetration depths for antibody constructs (A). Tumor spheroids incubated with the Alexa Fluor 680 antibody constructs represent experimental penetration depths for each construct in 50% mouse serum while ex vivo staining of PSMA (red) displays available antigen (B). These images were analyzed with a Euclidean map to semi-quantitatively depict penetration depths (C, n = 6 - 13 spheroids per group). The table displays binding affinity, on rates and the net internalization rate for these antibody constructs (which accounts for trafficking effects such as recycling and down-regulation).

These predictions were validated *in vitro* using spheroids made up of DU145-PSMA cells. Histology images of the spheroids are shown in Figure 3-6B. Ex vivo staining of the tissue slides indicated uniform PSMA expression throughout the spheroids (red), and incubation with antigen negative DU145 spheroids showed rapid and uniform distribution (which was only detectable at high concentrations due to a lack of binding, Figure 3-7A&B). The absolute penetration distances

were dependent on the cell packing, with spheroids seeded at lower cell density (2000 vs. 3000) and grown for longer periods of time (14 days vs. 7 days) resulting in lower penetration (Figure 3-7C), likely due to higher cell density/lower void fraction, but the relative pattern of penetration remained consistent.

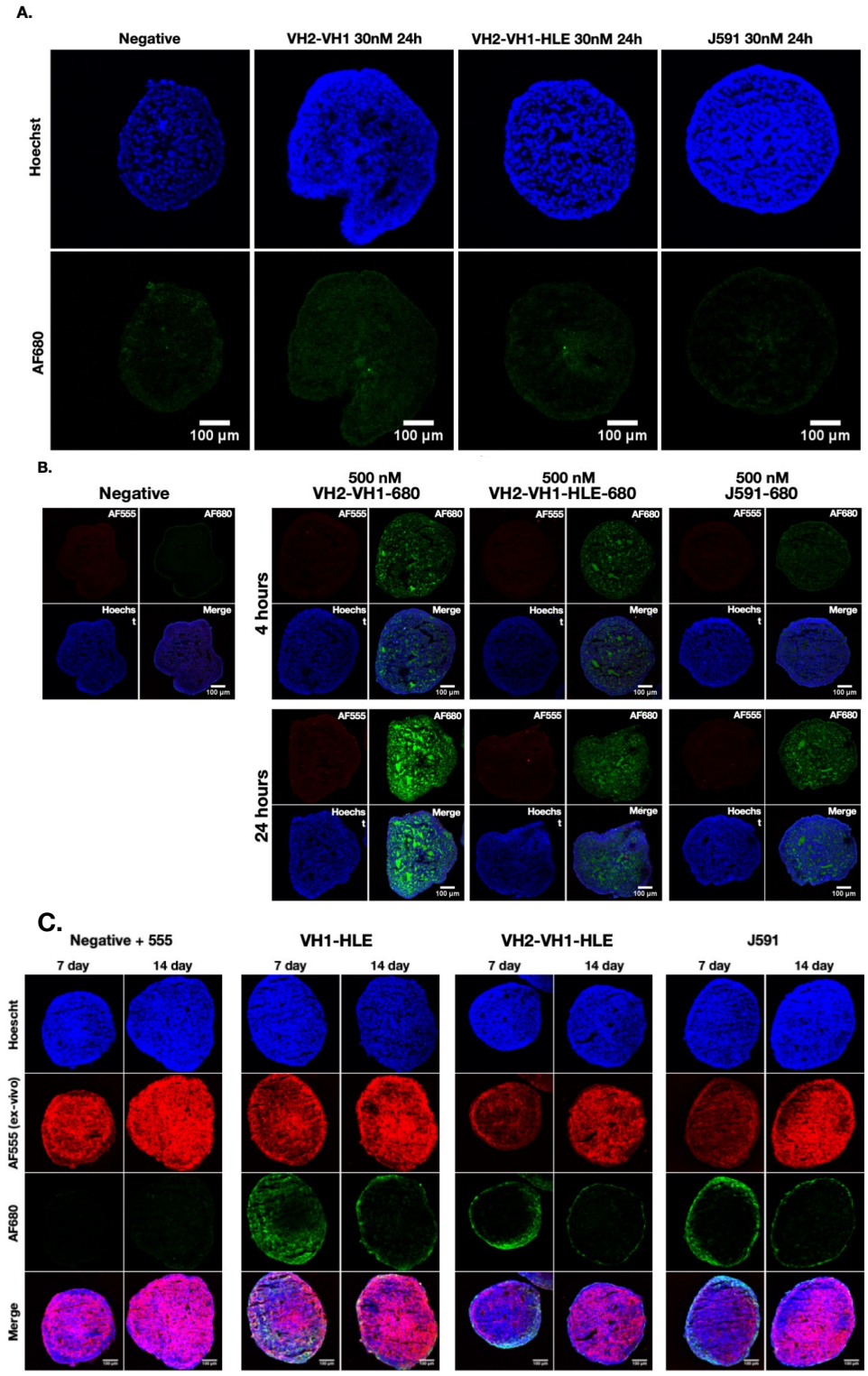

Figure 3-7. PSMA-negative DU145 spheroids display homogenous distribution.

Binding of PSMA targeting agents was analyzed with PSMA-negative DU145 spheroids incubated at either 30nM (A) or 500 nM (B). (C) Histology images of tumor spheroids grown for 7 vs 14 days compared for negative, V_{H1}-HLE, V_{H2}-V_{H1}-HLE, and J591 antibody constructs.

These results were maintained across ~10 independent experiments (each done on separate days) containing ~25 spheroids per fluorescent antibody (Figure 3-8). Quantitative image analysis confirmed the higher penetration of V_{H1}-HLE-AF680 relative to the other fluorescent antibodies (Figure 3-6C). The experimental data complements the computational predictions as V_{H1}-HLE-AF680 was demonstrated to distribute farther than any of the other antibodies tested.

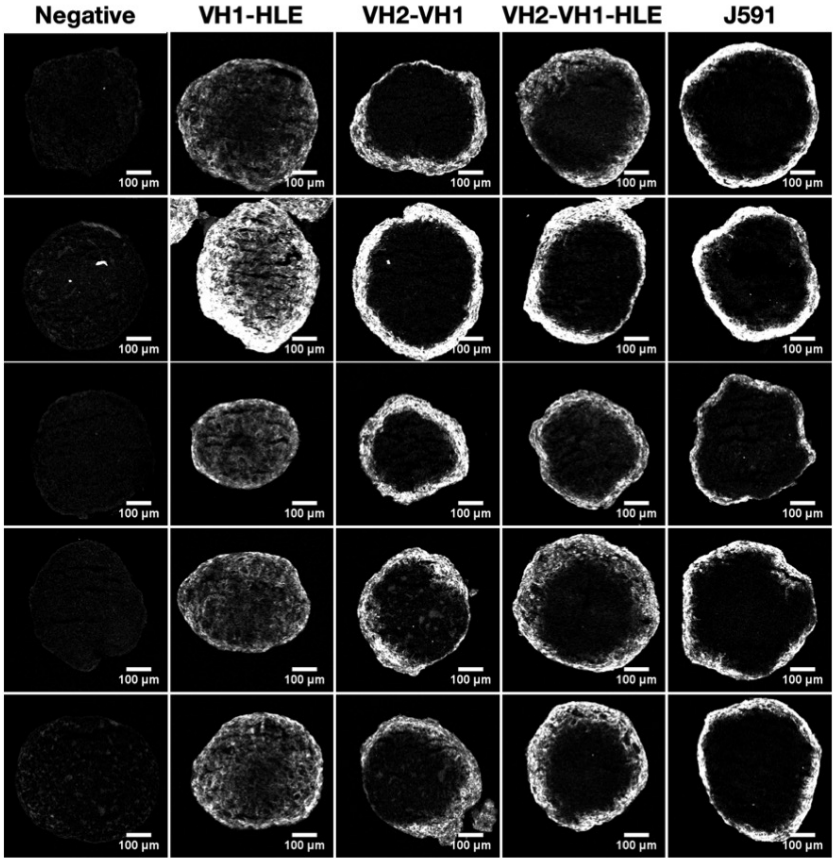

Figure 3-8. Robust spheroid penetration measurements

Histology image of tumor spheroids were gathered over multiple days and separate tumor spheroids.

The spheroid experiments provided a high-throughput, well-controlled, and robust environment to quantify tissue penetration. To account for additional considerations *in vivo,* such as plasma clearance and extravasation, tumoral distribution was further analyzed in DU145-PSMA xenografts.

Tumor histology images captured the overall fluorescent antibody distribution following intravenous delivery at the same doses as the efficacy study. Similar trends were seen for *in vivo* tumor distribution as those predicted by the computational model and demonstrated in the spheroid experiments. V_{H2}-V_{H1}-AF680 and V_{H2}-V_{H1}-HLE-AF680 exhibited limited penetration similar to that of the perivascular distributed J591-AF680 antibody, while the V_{H1}-HLE-AF680 had greater penetration targeting more cells (Figure 3-9).

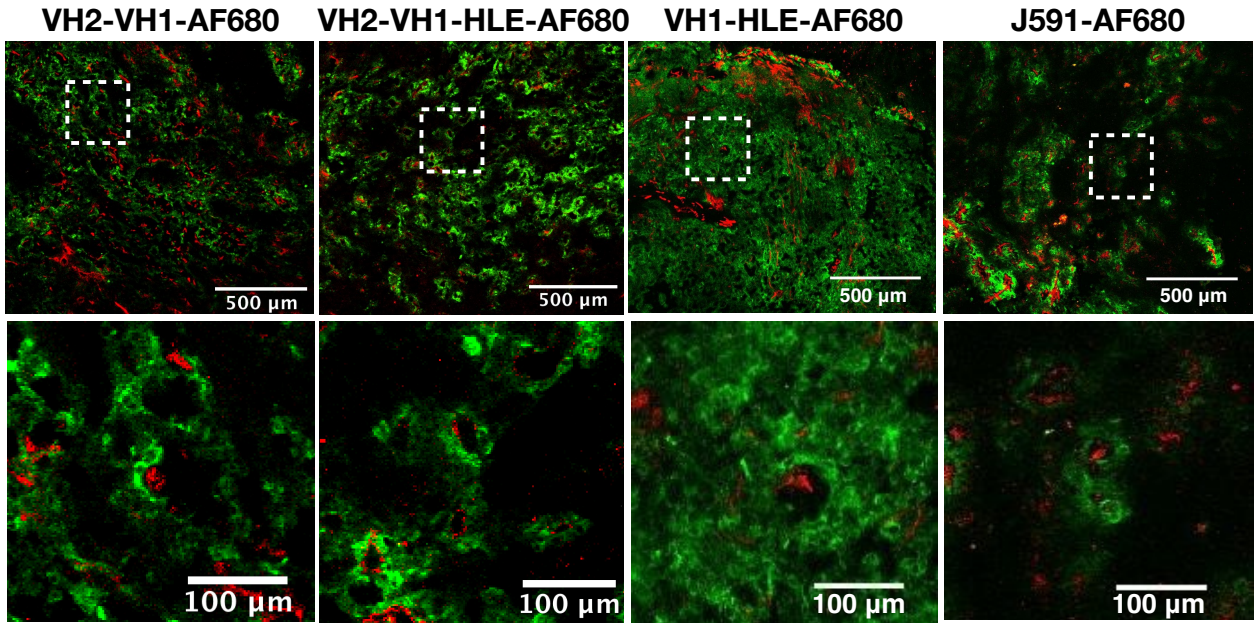

Figure 3-9. In vivo tumor tissue penetration of fluorescent proteins

24 hrs after tail vein administration of Alexa Fluor 680 antibody constructs dosed at the same level as the efficacy studies, DU145-PSMA xenografts were frozen in OCT and processed for histology. Blood vessels, shown in red, were ex vivo labeled with Alexa Fluor 555 anti-CD31 antibody while penetration of Alexa Fluor 680 antibody constructs is shown in green.

The histology images provide a semi-quantitative look at the differences in tumor penetration between fluorescent antibodies and are consistent with the *in vivo* computational predictions using the Krogh cylinder model (Figure 3-10). However, they do not provide absolute quantification of payload delivery with single-cell resolution that would allow for precise correlations between efficacy and penetration.

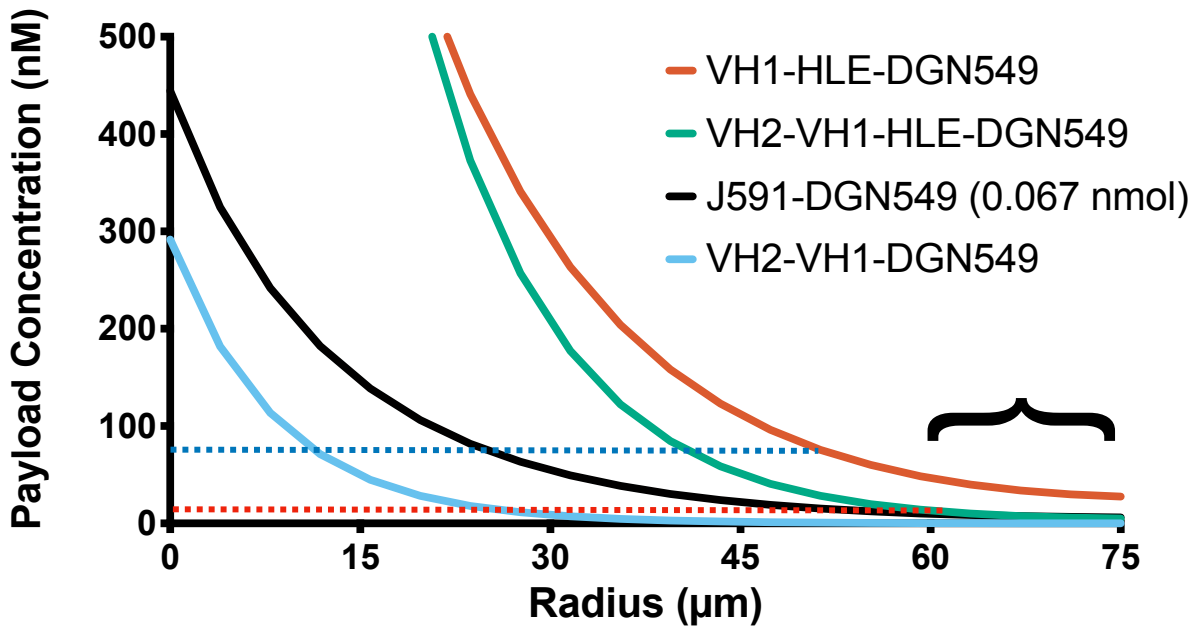

Figure 3-10. In vivo tumor tissue penetration of fluorescent proteins

The differences in tumor penetration distance for each ADC construct were simulated using the parameters in Table 3-1 and the Krogh cylinder code. (Note the J591 data has been adjusted by the DAR to display the payload concentration.) 10^5 payloads per cell was indicated as lethal to ~95% of cells based on Figure S20. This corresponds to an intracellular concentration of ~80nM (blue line) while 50% cell death would occur at ~8nM (red line). Given that tumor volume scales with the square of tumor radius, the bracketed area highlights approximately 1/3 of the tumor cells in the tumor.

The single-cell measurements using flow cytometry enabled quantification of the fraction of cells targeted in the tumor and the number of payloads per cell for the targeted fraction. V_{H1}-HLE-AF680 targeted more cells than the other antibodies ($p < 0.05$) (Figure 3-11A), consistent with the computational model and histology experiments. This finding is also consistent with *in vivo* efficacy in the same xenograft, where V_{H1}-HLE-DGN549 showed the most tumor growth inhibition of the ADC constructs tested. While V_{H1}-HLE-AF680 targeted the largest fraction of cells, the number of payloads per cell in these targeted cells was lower than V_{H2}-V_{H1}-HLE-AF680 (but not statistically significant due to high variability, Figure 3-11B), which explains the similar tumor-averaged total uptake (%ID/g). Using an AF647 tag (and its corresponding calibration curve) for higher sensitivity due to lower total uptake, we found that V_{H2}-V_{H1}-AF647 reached a slightly lower fraction of targeted cells, and the number of payloads per cell was ~1/3 compared

to V_{H2}-V_{H1}-HLE-AF680), resulting in the much lower overall %ID/g in Figure 3-5A. Note that the J591-AF680 antibody was administered at a lower payload dose, resulting in fewer payloads per cell even though it has a similar uptake efficiency (~30 %ID/g).

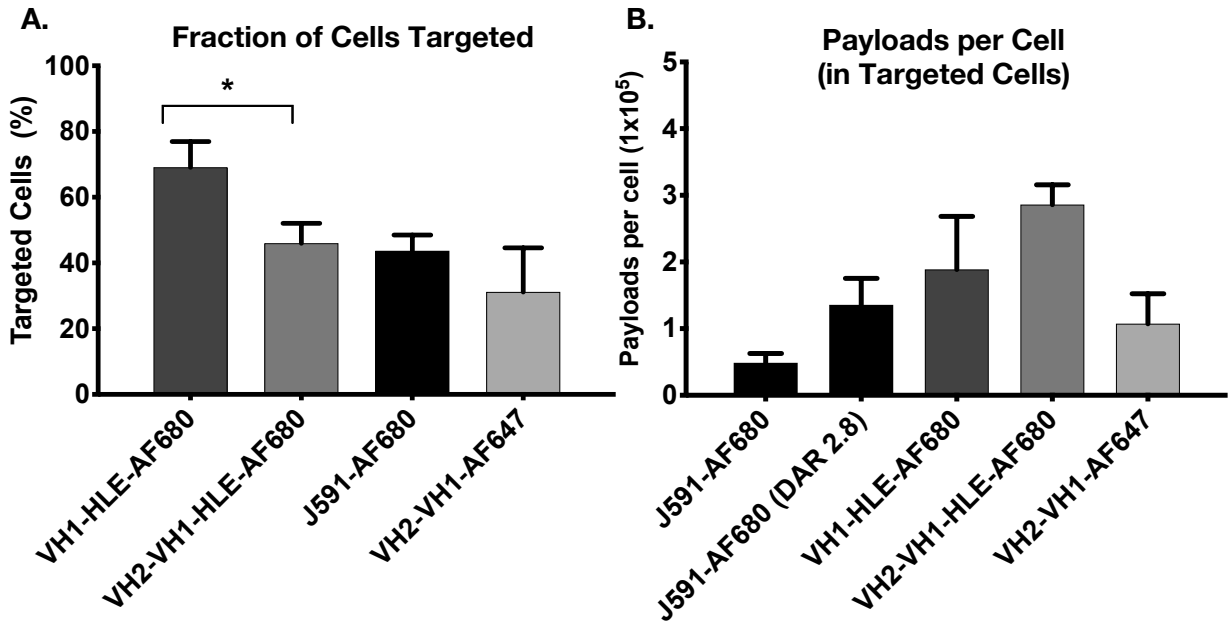

Figure 3-11. Single-Cell Payload Measurements

A fraction of the tumor resected 24 hrs after antibody fluorophore conjugate administration was processed into a single cell suspension and used with flow cytometry to determine conjugate distribution and payload uptake. J591-AF680 antibody was given at a dose of ~0.07nmols (with a DAR of 2.8, so the equivalent payload uptake is shown) while Humabodies were dosed at ~0.7nmols. Targeted cells (A) and payloads per cell (B) are represented as median values with standard deviation error bars. Payload quantification involved the single cell analysis of three separately treated and dissociated tumors for each treatment. * = $p < 0.05$differences in tumor penetration distance for each ADC construct were simulated using the parameters in Table 3-1 and the Krogh cylinder code. (Note the J591 data has been adjusted by the DAR to display the payload concentration.) 10^5 payloads per cell was indicated as lethal to ~95% of cells based on Figure S20. This corresponds to an intracellular concentration of ~80nM (blue line) while 50% cell death would occur at ~8nM (red line). Given that tumor volume scales with the square of tumor radius, the bracketed area highlights approximately 1/3 of the tumor cells in the tumor.

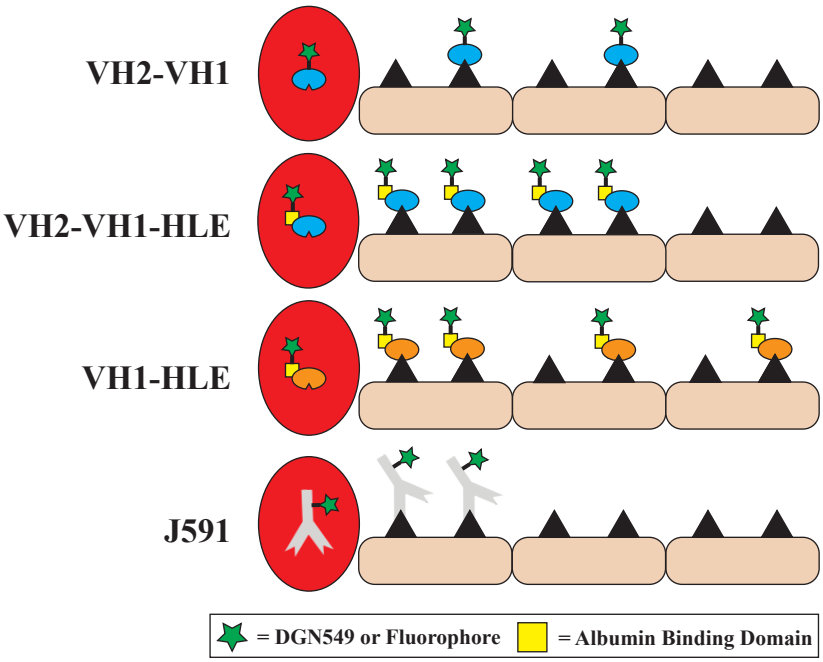

Figure 3-12. Conceptual schematic of the distribution for the panel proteins

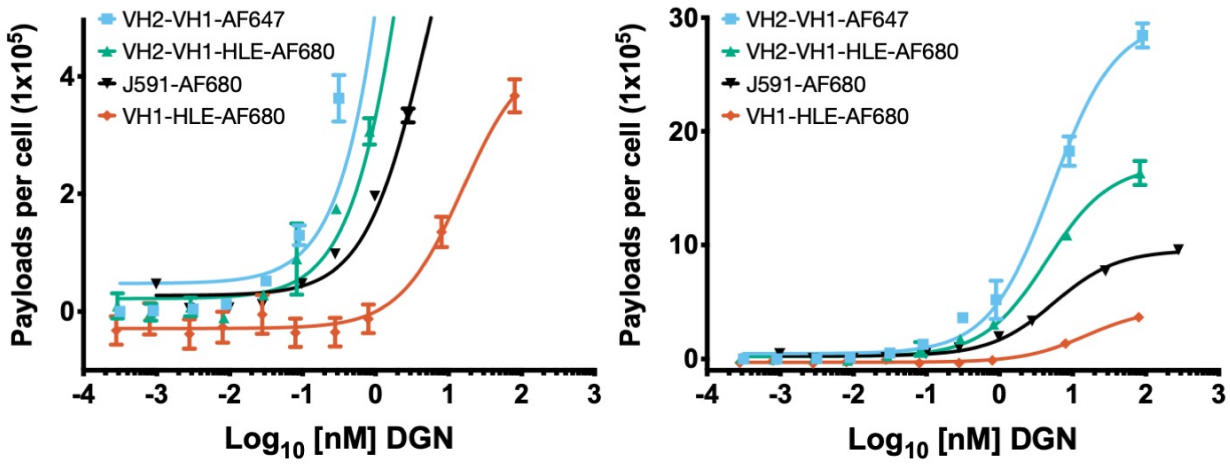

Figure 3-13. In vitro protein uptake.

An *in vitro* toxicity assay provided measurements of fluorophore uptake that was then correlated (1:1) to payload uptake. Both plots show the same data but with different XAb axis scales.

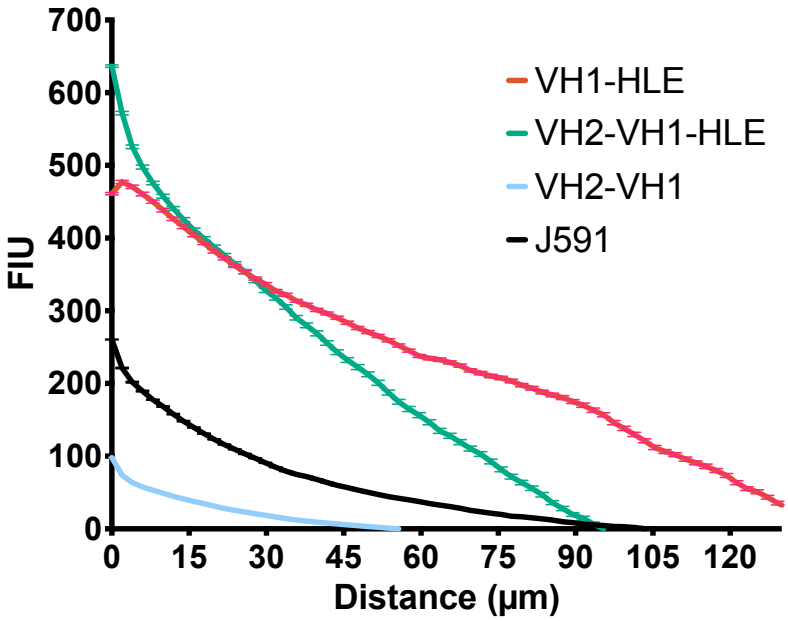

Figure 3-14. Euclidean Distance Mapping for Histology slides

The fluorescent intensity of each pixel in the histology slides was recorded along with distance from the nearest blood vessel and then plotted to display a semi-quantitative map of ADC penetration.

3.5 Discussion

Following the first wave of ADC approvals, various protein-drug conjugates are being developed based on affinity, toxicity, and stability to achieve an optimal therapeutic effect. Although the heterogeneous, perivascular distribution of these agents is well documented[84-88], the impact on efficacy is not routinely isolated and investigated. Here, we demonstrated the improved penetration of a single variable heavy chain unit conjugated to an albumin binding domain (V_{H1}-HLE-AF680) over other ADC constructs in a 3D spheroid cell culture system and *in vivo*. As a result, V_{H1}-HLE-DGN549 exhibited higher *in vivo* efficacy than the other ADC constructs despite having lower potency *in vitro*.

In vitro cellular toxicity assays indicated that the rapidly internalized biparatopic antibody conjugates (V_{H2}-V_{H1}-HLE, V_{H2}-V_{H1}) and J591 had the highest potency, followed by V_{H1}-HLE (Figure 3-1A). The greater *in vitro* potency of the biparatopic ADC constructs is likely due to receptor surface clustering that causes rapid internalization of the drug[80, 89, 90]. In monolayer cell culture, there are no mass transport/drug delivery limitations, so cellular internalization/payload release is the rate-limiting step in payload uptake and the key determinant for cell killing. However, *in vivo*, the extravasation of ADC from the blood is the rate-limiting step and determines total tumor uptake (at sub-saturating doses, which is typical for highly expressed antigens). Therefore, the faster internalization rate did not deliver more total payload to the tumor, as seen by the similar tumor biodistribution for V_{H1}-HLE-AF680 and V_{H2}-V_{H1}-HLE-AF680 (Figure 3-5A). The rapid internalization instead limited the penetration distance of V_{H2}-V_{H1}-AF680 and V_{H2}-V_{H1}-HLE-AF680 in tumor spheroids (Figure 3-6) and *in vivo* (Figure 3-9), which therefore reached fewer cells (Figure 3-11). Although the amount of V_{H1}-HLE-AF680 and V_{H2}-V_{H1}-HLE-AF680 delivered to the tumor was the same, the slower internalizing V_{H1}-HLE-AF680 was able to penetrate farther in the tumor to target and kill more cells than V_{H2}-V_{H1}-HLE-AF680 as illustrated by the diagram in Figure 3-12.

One of the main disadvantages of using single-domain antibodies or other small protein scaffolds in place of antibodies is rapid renal clearance[74]. V_{H2}-V_{H1}-AF680 demonstrated poor tumor uptake caused by this rapid kidney filtration. Conjugating an albumin binding domain to the monovalent and biparatopic constructs slowed clearance nearly 100-fold, leading to increased tumor uptake, comparable to a monoclonal antibody (Figure 3-5). Putative albumin binding within the tumor spheroid interstitium did not appear to slow down the effective diffusion/tissue

penetration. This is in apparent contrast to the use of lipophilic moieties to bind albumin, which can lower extravasation rates and diffusion coefficients[83].

Interestingly, some of the *in vivo* efficacy trends differed between the moderate and high expressing xenografts (Figure 3-3). In both models, the V_{H1}-HLE-DGN549 demonstrated the greatest efficacy, but the relative efficacy of the other agents varied between the two tumor models. In the CWR22Rv1 tumor model with lower expression, V_{H1}-HLE-DGN549 and the J591-DGN549 ADC showed almost identical tumor growth inhibition, as did V_{H2}-V_{H1}-HLE-DGN549 and V_{H2}-V_{H1}-DGN549. But in the DU145-PSMA tumor model, each protein-drug conjugate exhibited distinct efficacy. The most likely explanation for differences in efficacy between the DU145-PSMA and CWR22Rv1 tumor models is the level of PSMA expression: DU145 has relatively high expression (~10^6 receptors/cell), while CWR22Rv1 has moderate expression (<10^5 receptors/cell). With more available targets for binding in a higher expression cell line, more ADC is required to saturate the first few cell layers, thus hindering diffusion to regions distal from vasculature. Cell death often correlates with intracellular concentration[91], and V_{H1}-HLE-DGN549 maintained efficacy (even exceeding V_{H2}-V_{H1}-HLE-DGN549 *in vivo*, Figure 3-3) with a lower (but still lethal) number of payloads per cell than V_{H2}-V_{H1}-HLE-DGN549 based on *in vitro* measurements (Figure 3-11, Figure 3-13). This is consistent with V_{H2}-V_{H1}-HLE-DGN549 delivering more of the potent DGN549 payloads than needed to kill targeted cells (i.e. overkill) in this model. Another contributing factor for the differences in degree of response between tumor models could be the starting tumor size. Treatments were generally less efficacious in the DU145-PSMA tumor model, where doses were administered at an average tumor size of 250 mm^3, versus 100 mm^3 in the CWR22Rv1 tumor model.

The slower clearance due to the presence of a half-life extension domain (i.e. higher plasma AUC) was expected to increase efficacy in the mouse model of prostate cancer based on greater drug exposure. Previous studies have demonstrated that exposure (i.e. plasma AUC) correlates with tumor uptake and response to ADCs (e.g. [92, 93]). This is supported by the improved *in vivo* efficacy of V_{H2}-V_{H1}-HLE-DGN549 compared to V_{H2}-V_{H1}-DGN549 (Figure 3-1) in the DU145-PSMA tumor model (single dose each). The plasma clearance and biodistribution data confirmed that V_{H2}-V_{H1}-HLE-AF680 is cleared more slowly and has significantly higher tumor uptake than V_{H2}-V_{H1}-AF680 (Figure 3-2). According to single-cell measurements, V_{H2}-V_{H1}-HLE-AF680 targeted a higher number of cells than V_{H2}-V_{H1}-AF647 with more payloads per cell in each targeted cell (Figure 3-5). Alternatively, V_{H2}-V_{H1}-HLE- DGN549 and V_{H2}-V_{H1}-DGN549 showed almost identical efficacy in the CWR22Rv1 tumor model with lower PSMA expression where V_{H2}-V_{H1}-DGN549 was administered in three fractionated doses of 10 μg/kg. Fractionated dosing of the faster cleared V_{H2}-V_{H1}-DGN549 increased tumor exposure time compared to a single bolus dose. The similar efficacy of V_{H2}-V_{H1}-HLE-DGN549 and V_{H2}-V_{H1}-DGN549 in this system further highlights the significance of extended tumor exposure to *in vivo* efficacy.

Taken together, the differences seen with the *in vivo* efficacy studies cannot be explained solely by total tumor uptake or *in vitro* potency, given that V_{H1}-HLE outperformed V_{H2}-V_{H1}-HLE and J591 *in vivo* with similar tumor uptake (Figure 3-2) and lower *in vitro* potency (Figure 3-1). The best correlate for efficacy was the delivery of a lethal cellular dose of payload to the maximum fraction of cells within the tumor. The *in vitro* spheroid and *in vivo* histology images agreed with

a predictive computational model based on the fundamental binding kinetics, tumor physiology, target specific expression/internalization, and biophysical properties (e.g. diffusion) of the ADCs.

These results can be used to help design more effective ADCs for efficient payload delivery and cell killing. Importantly, while this work demonstrates that the V_{H1}-HLE-DGN549 is the most effective in this system, it does not indicate that monovalent binding agents are *always* the most efficacious agents *in vivo*. Rather, the work highlights the need to customize the construct based on the target properties (expression, internalization), payload (with or without bystander effects, maximum tolerated dose), and properly scale these results to the clinic (i.e. clearance rates). Likewise, the PSMA expression in these animal models was moderate to high, and the payload used is extremely potent. Under these conditions, the constitutive internalization rate of PSMA was sufficient for tumor cell killing in these animal models without the need to drive more rapid internalization through biparatopic clustering. However, driving faster internalization could be very useful under circumstances with lower expression or slower constitutive turnover. In fact, it raises the intriguing possibility of driving internalization of targets that are internalized too slowly for efficient payload delivery generally considered 'non-internalizing'. Because biparatopic clustering uses a different internalization mechanism, in theory it could also be used to overcome resistance mechanisms due to poor cellular internalization/trafficking[90]. These data could be compared with truly 'non-internalizing' ADCs that release their payload outside the cell[94, 95].

3.6 Conclusion

In summary, single-domain antibodies provide a promising platform for controlling the internalization kinetics, binding affinity, size, and plasma clearance of these ADC constructs.

While the use of a variable heavy chain binding domain provides improved transport characteristics (e.g. blood vessel permeability, diffusion), rapid clearance from the blood through the kidneys results in short plasma half-lives that limit therapeutic potential. The addition of a small albumin binding domain improved plasma half-lives without significantly impacting the extravasation and tissue penetration of the agents, allowing 'antibody-like' targeting efficiencies. The investigation of four ADC constructs (V_{H1}-HLE, V_{H2}-V_{H1}, V_{H2}-V_{H1}-HLE, and J591) showed markedly different *in vitro* potencies, tissue penetration, plasma clearance, and efficacy. Interestingly, neither plasma clearance/AUC nor *in vitro* potency correlated with tumor response. The systemic, organ, tissue, and single-cell pharmacokinetic data indicated that the ability to reach a maximum number of cells with a lethal payload dose was the driving factor in efficacy. These results were corroborated by a computational Krogh cylinder model. This combination of computational modeling and experimental quantitative pharmacology can be used to scale these results to other targeting systems and the clinic for more efficient design of highly efficacious agents.

3.7 Experimental Methods

Computational model – Krogh Cylinder

The Krogh cylinder model has been validated for tissue distribution of antibodies as well as smaller molecules by our group and others[8, 87, 96-98]. A 1-D cylinder model consisting of only radial gradients was used to represent the distribution of antibody constructs because they are permeability limited. The model tracked the concentration of free target as well as free, bound, and internalized antibody. Equations and parameters used for simulations are in **Appendix A**. The equations describe the rate of antibody extravasation from a blood vessel, the diffusion and

subsequent binding to a PSMA receptor in the tissue, at which point the therapeutic is internalized and degraded. Modifications were made to parameters based on the size of the single-domain antibody tested. All parameters used in the Krogh cylinder were gathered from the literature or measured independently (i.e. not fit to tissue distribution data).

Single-Domain Antibody Constructs and Imaging Agents

Alexa Fluor 680 (AF680), Alexa Fluor 647 (AF647), or Alexa Fluor 488 (AF488) (ThermoFisher Scientific) were conjugated to each antibody through sortase labeling of the LPTGX motif present at the C-terminus. Briefly, NHS ester dyes were reacted with propargyl amine in aqueous solution buffered with 7.5% sodium bicarbonate for 30 minutes at room temperature, followed by purification on reverse-phase HPLC. The alkyne-dye was then reacted with a GGGX peptide (synthesized on a CEM Liberty Blue peptide synthesizer), where X is the non-natural amino acid azidohomoalanine, via copper-catalyzed click chemistry similar to previously published protocols[99, 100] to generate GGGX-dye. The peptide-dye product was purified on reverse-phase HPLC and reacted with the antibody constructs (5:1 ratio) for 10 minutes with 2μM sortase and 5mM calcium chloride in aqueous HEPES buffer. The reaction mix was filtered with a Costar® spin-x centrifuge tube filter (ThermoFisher Scientific) containing 300μL of HisPur™ Ni-NTA Resin (ThermoFisher Scientific) to remove unreacted protein (containing a His-tag) and the His-tagged sortase and then purified via size exclusion chromatography/FPLC. The fluorescent constructs were concentrated with AMICON molecular weight spin filters to 10-40μM with a degree-of-labeling (DoL) ~0.7 dyes/protein as confirmed with absorption readings from a NanoDrop 1000 spectrophotometer (ThermoFisher Scientific). After purification, Native-PAGE gels were scanned on an Odyssey CLx to ensure all free dye was removed.

Cell Culture and Animals

The DU145 cell line (RRID: CVCL_0105, PSMA negative) and PSMA transfected DU145 cell line generated by Kampmeier et al. (DU145-PSMA)[101] were received from Crescendo Biologics in September. Cells were cultured 2-3 times per week up to passage number of 50 and grown in RPMI 1640 supplemented with 10% (v/v) FBS, 50 U/mL penicillin, and 50 µg/mL streptomycin at 37°C with 5% CO_2. Mycoplasma testing was performed annually using the Mycoalert Testing Kit (Thermo Fisher Scientific, NC9719283). All animal studies were approved and conducted in compliance with the Institutional Animal Care and Use Committee (IACUC) of the University of Michigan and Association for Assessment and Accreditation of Laboratory Animal Care International (AAALAC). Pharmacokinetic and *in vivo* tumor distribution animal studies were conducted in 4–8 week old homozygous female nude (RRID: 2175030, Foxn1nu/nu, Jackson Laboratories) mice. For *in vivo* tumor distribution and growth studies, the nude mice were inoculated in both flanks with 5×10^6 cells, one flank with DU145-PSMA and the other with DU145 cells. For tumor growth studies, tumor volume was measured with calipers 3x per week using the formula volume = 0.5*length*width^2. Corrected sample size for each treatment group was calculated as 10 based on an *a priori* power test.

Plasma Clearance

Plasma clearance was measured after tail-vein injection of 0.7 nmol of fluorescent antibody. Plasma samples were obtained through retro-orbital sampling 10 µL of whole blood, then mixed with 15 µL of PBS-EDTA (10 mM) and centrifuged at 3000*g* for 1 min. 18 µL of the resulting plasma was frozen at -80°C until further analysis. The antibody concentration was

determined by scanning 15 μL of plasma in a 384-well black-walled plate (Corning) on the NIR Odyssey CLx Scanner (LI-COR) and comparing the signal intensity to a calibration curve of known antibody concentration to signal intensity at the same DoL and scan settings. The plasma concentration at each time point was normalized to the initial concentration, and then the clearance was fit to a biexponential decay using PRISM (GraphPad). Absolute plasma concentrations at 1 min were compared with theoretical initial concentrations calculated based on the dose and estimated plasma volume of the mouse.

Biodistribution

The biodistribution of fluorescent antibody was conducted as previously described[10, 38, 102]. Briefly, 24 XAb after tail-vein injection of 0.7 nmol of fluorescent antibody, animals were euthanized, and organs were resected. Organs were then homogenized by mechanical disruption, incubated with 1:1 RIPA buffer (Fisher Scientific)/PBS solution supplemented with 5 mg/mL collagenase IV (Fisher Scientific) for 1.5 XAb, disrupted using a FB-120 Sonic Dismembrator, and incubated in 1:1 RIPA buffer/0.025% trypsin-EDTA solution for 1.5 XAb. After homogenization, organs were serially diluted and scanned on the Odyssey CLx scanner to ensure fluorescence detection was in the linear range. The signal intensity was compared to a calibration curve and normalized to organ weight and homogenate volume to calculate the percent injected-dose per gram (%ID/g).

Fluorescence Histology for Imaging Antibody Tumor Distribution

As previously described[10, 38, 98], the tumor distribution of fluorescent antibody was analyzed using fluorescence microscopy 24 hours post-injection. Briefly, 0.7 nmol fluorescent

antibody (or 0.067 nmol of J591 anti-PSMA IgG) was administered via tail-vein injection once the tumor volume was ~250mm^3. The animal was imaged 24 hours post-injection. Hoechst 33342 (ThermoFisher Scientific) was administered 15 minutes before euthanasia via the tail-vein at 15 mg/kg to label functional vasculature in the tumor. Tumors were then resected, flash frozen in OCT using isopentane chilled on dry ice and sectioned for histology on a cryostat (10-μm slices). Before imaging, tumor slices were stained for 30 min with anti-mouse CD31 (BioLegend, 102402) conjugated to Alexa Fluor 555. Microscopy was performed using an upright Olympus FV1200 confocal microscope equipped with a 20× objective and 405, 543, and 635 lasers. High resolution tumor images were obtained by stitching smaller images with the Olympus software. Images were exported and analyzed using ImageJ image analysis software as described previously[10, 38, 98].

Flow Cytometry

Resected tumors were digested into a single-cell suspension using a tumor dissociation kit (Miltenyi Biotech, 130-096-730) and passed through a 40 μm filter to remove clumped cells. The suspension was washed 2x with PBS and then analyzed using an Attune Acoustic Focusing Cytometer (Life Technologies).

In vitro Toxicity Assay

ADC constructs with a C-terminal cysteine residue were conjugated to a potent DNA-alkylating agent (DGN549) via maleimide chemistry similar to previous reports[79], in a reaction buffer containing 25% N,N-Dimethylacetamide and 75% 50mM potassium phosphate-5mM EDTA, pH 6.0 for 3 hours at 25°C and then purified by Illustra NAP-25 columns (GE Healthcare) to achieve an average DAR of ~1.0. The potency of these ADC constructs was then assessed by

seeding DU145-PSMA cells at a density of 8,000 cells per well in 96-well plates for cell viability assays. Titrations of DGN549-conjugated antibodies were replaced daily for 6 days. At the endpoint, cells were washed twice with media and then incubated with PrestoBlue Cell Viability Reagent (ThermoFisher Scientific, A13261) for 25 minutes at 37°C in a 1:10 dilution in media. The fluorescence (560/590, Ex/Em) of each well was then measured using a Biotek Synergy plate reader to measure final cell viability. Background signal from wells without cells was subtracted from all samples, and then, viability was normalized to untreated cells.

In vivo Tumor Growth Curves

For the high expression DU145-PSMA xenografts, female homozygous Fox1n nude mice (Jackson Laboratories) were injected in the left flank with 5 x 10^6 DU145-PSMA cells. Mice were assigned into six treatment groups: PBS vehicle control (n=9), non-binding control VH-HLE-DGN549 (n=6), V_{H1}-HLE-DGN549 (n=9), V_{H2}-V_{H1}-HLE-DGN549 (n=10), V_{H2}-V_{H1}-DGN549 (n=9), and J591-DGN549 (n=9). Treatments were administered in a single dose as tumors reached an approximate volume of 250 mm^3. Doses were matched to the amount of payload delivered for the maximum tolerated dose (30 μg/kg for Humabody drug conjugates, 10 μg/kg for J591). The J591 ADC was given at a 3-fold lower payload dose to match the toxicity between the agents as estimated from weight loss. In general, the Humabody drug conjugates were better tolerated, enabling a higher payload dose. Tumor sizes were monitored three times per week until the study endpoint.

Similarly, for the moderate expression CWR22Rv1 xenografts, male CB.17 SCID mice were implanted subcutaneously on one flank with 1 x 10^7 CWR22Rv1 human prostate carcinoma

cells. After 20 days, animals with individual tumor xenograft volumes of 75 to 126 mm^3 were sorted into groups (n =10) with a group mean tumor volume of 106 mm^3 and dosing was initiated. Half-life extended (HLE) Humabody drug conjugates were administered in a single dose on day 1 of the study. Non-HLE Humabody drug conjugate was administered in three, 10 μg/kg doses, administered on day 1, 3 & 5 of the study. Tumor size in mm^3 was monitored individually and a group median tumor volume calculated. Animals reaching the endpoint volume of 1000 mm^3 or the end of the study were euthanized.

Tumor Spheroid Experiments

Tumor spheroids were cultured using custom-made 384-well plates developed described previously[103]. Briefly, 3000 cells suspended in 25μL of seeding media comprising 19.5μL complete RPMI culture media, 5μL of 1.2% (XAb/v) methocellulose (Dow Corning), and 0.5μL matrigel were added to alternate wells of the 384-well hanging drop plate. The edges of the 384-well plate were lined with sterile gauze soaked in sterile distilled water (Gibco) containing 0.1% penicillin/streptomycin. The 384-well plate was sandwiched in a 96-well clear well plate containing sterile water to minimize media evaporation from the hanging drops. Media changes were made every 2 days by removing 9μL media from the drop and adding in 10μL of fresh media (to adjust for evaporation), repeated twice for each drop. Spheroids were cultured for 7 days until they attained a diameter of 400-500μm.

To study distribution, the hanging drops were incubated in the 384-well plate with V_{H1}-HLE-AF680, V_{H2}-V_{H1}-HLE-AF680, V_{H2}-V_{H1}-AF680, or J591-AF680 at a final concentration of 30nM, by replacing 10μL of the 25μL of the spheroid media with 10μL of 75nM (2.5X

concentration) fluorescent antibody. The drug concentration in the media was assumed to be constant over the course of the incubation (i.e. no depletion effects). After 24 hours of incubation, the spheroids were individually extracted from the wells and washed 2X with PBS before being fixed with 4% formaldehyde, frozen in OCT, and stored at -80ºC until further processing. Frozen OCT blocks were sectioned for histology on a cryostat (16-µm slices), and sections were stained ex-vivo with Hoechst 33342 (ThermoFisher Scientific) for 5min and J591-AF555 for 30min before imaging on the Olympus FV1200 confocal microscope. Multi-channel imaging of spheroid sections was performed with a 20X objective with 405 (Hoechst-33342), 543 (AF555), and 635 (AF680) lasers. Image analysis was performed to generate a Euclidean distance map (Figure 3-14).

Statistical Analysis

Plot values are shown as mean +/- standard deviation. Data were analyzed for statistical significance (p values <0.05) with an unpaired, two-tailed t-test with Welch's correction using GraphPad Prism 8 for macOS.

Chapter IV

Key Metrics to Expanding the Pipeline of Successful Antibody-Drug Conjugates

4.1 Publication Information

Nessler, I., Menezes, B. & Thurber, G.M. Key Metrics To Expanding The Pipeline Of Successful Antibody-Drug Conjugates. *Trends Pharmacol Sci* **42**, 803-812 (2021).

Modifications have been made to the published document to adapt the content to this text. The previous chapter applied NIR fluorescent methods to identify key protein characteristics in tumor efficacy. This chapter builds on the previous work by analyzing successful, FDA approved antibody-drug conjugates and identifying key features for future protein-drug conjugates.

4.2 Abstract

Although the recent FDA approval of six new antibody–drug conjugates (ADCs) is promising, attrition of ADCs during clinical development remains high. The inherent complexity of ADCs is a double-edged sword that provides opportunities for perfecting therapeutic action while also increasing confounding factors in therapeutic failures. ADC design drives their pharmacokinetics and pharmacodynamics, and requires deeper analysis than the commonly used Cmax and area under the curve (AUC) metrics to scale dosing to the clinic. Common features of current FDA-approved ADCs targeting solid tumors include humanized IgG1 antibody domains,

highly expressed tumor receptors, and large antibody doses. The potential consequences of these shared features for clinical pharmacokinetics and mechanism of action are discussed, and key design aspects for successful solid tumor ADCs are highlighted.

4.3 Background

Antibody drug conjugates (ADCs) are entering an unprecedented period of success with the FDA approval of six additional ADCs in the past two years. ADCs are complex biologics made up of three main components: an antibody backbone, the payload, and a connecting linker. The ADC structure is highly customizable, offering opportunities to tailor an ADC to a particular target, but also increasing the complexity of their design. As of 2021, six ADCs are indicated for hematological tumors and four ADCs for solid tumors. However, before 2019, only a single ADC was approved for solid tumors, and many have failed during clinical development.

Quantitative pharmacology approaches have a critical role to play given the complex and often counterintuitive ADC pipeline. Many drugs that appear efficacious *in vitro* and in preclinical models ultimately fail in clinical trials. Perhaps even more consequential, evidence suggests some drugs that fail traditional *in vitro* and preclinical tests could potentially be successful in the clinic. As anecdotes of poor preclinical performance of successful ADCs, Trodelvy potency is difficult to quantify *in vitro* due to the role of hydrolyzed drug[104], and Enhertu shows no response in a nude mouse model using a syngeneic line despite efficacy in immunocompetent mice[105]. Understanding the similarities between currently approved solid tumor ADCs can yield insights toward rational solid tumor ADC design and continued clinical success.

Despite recent clinical success, antibody drug conjugates have a longer history than monoclonal antibodies themselves. Embodying Ehrlich's Zauberkugeln or 'Magic Bullets,' proposed at the turn of the previous century, researchers first treated mouse leukemia with amethopterin-gamma-globulins in 1958[106]. Even more avant-garde, Ghose and colleagues treated a melanoma patient by intra-tumoral and intravenous injection of chlorambucil-anti-melanoma-globulin in 1971 where 'all metastatic nodules regressed'[107]. With the advent of monoclonal antibodies by Kohler and Milstein in 1975, the modern concept of an ADC, with a specific target and controlled payload linkage, was born. A polyclonal vindesine-anti-CEA conjugate was the first target-specific ADC tested in several patients in 1983[108].

It's impossible to capture the accelerating ADC research over the interim between this trial and the current 10 FDA-approved ADCs in brief. Several notable highlights from this and related fields include the humanization of antibodies to avoid immune reactions[109], understanding antibody delivery issues including the 'binding site barrier'[110], elevated tumor interstitial pressure[111, 112], protein engineering advances[113], and their impact on delivery[114]. Within the ADC field, some of the early payloads lacked the potency required for ADCs, which limit cellular delivery to the internalization rate and number of receptors per cell, generating a push for more potent payloads. This led to ultra-high payload potency using some of the most toxic known (and synthetic) compounds. The higher potency also generated a push towards 'cleaner' targets with less healthy tissue expression. However, these targets tend to have lower tumor expression, and ultimately the higher potency payloads ran into non-target mediated toxicity limitations[115]. As discussed here, the current successful agents, particularly for solid tumors, have utilized high-

expression targets (10^5 to 10^6 receptors/cell) with moderately high payload potency[104, 116] delivered with large antibody doses (3.6 to 20 mg/kg over a 3-week period).

In terms of generating approved drugs, the trajectory has been rocky. After the first FDA approval of Mylotarg in 2000, the drug was removed from the market 10 years later, going from 1 to 0 approved drugs in a decade. During the 2010's, ADCs re-entered the market, including the first solid tumor ADC, Kadcyla in 2013. However, a string of high-profile failures dampened enthusiasm among many companies. It wasn't until the approval of 6 ADCs in a span of 2 years, including 3 for solid tumors, that enthusiasm has again returned. It's important we apply the lessons of the past to ensure a bright future for the field.

Recent FDA-approved ADCs follow three design criteria

The three recently approved solid tumor ADCs highlight important design criteria. While several components of the ADC show significant variability, the shared features are noteworthy. The structure of the four FDA-approved ADCs for solid tumors are very different and include diverse linker types (cleavable vs. non-cleavable, different mechanisms of release, varying stability), specific and non-specific conjugation, different targets, cancer types, and drug to antibody ratios (DARs). Intriguingly, the three common features between these therapies are 1) highly expressed targets (10^5 to 10^6 receptors/cell), 2) high antibody doses (3.6 mg/kg or larger doses over a 3-week period), and 3) an IgG1 isotype antibody backbone (**Table 1**). This last feature provides long circulation half-life in addition to providing the greatest potential for immune response through Fc interactions.

The three shared features have a significant impact on the drug delivery and distribution. In fact, because ADCs use known cytotoxic payloads (e.g. microtubule inhibitors) with known targeting agents (antibodies), a key feature to their clinical success is delivery – targeting efficacious amounts of payload for each tumor cell at tolerable doses. These shared design features each have individual impacts on the tumor targeted delivery of payload.

High Target Expression

Her2, Nectin-4, and Trop-2 are highly expressed tumor antigens with greater than 10^5 receptors per tumor cell and significantly lower healthy tissue expression. A high expression target can provide a greater therapeutic window due to a larger target sink. Since drug delivery to healthy tissue is often more efficient than delivery to tumors, a high antibody dose with a high expression tumor target may quickly saturate uptake in lower expression healthy tissue while still maximizing uptake in the tumor. The payload toxicity and/or DAR can then be modified to ensure delivery to tumor cells above a therapeutic threshold while maintaining a sub-therapeutic threshold in healthy tissue (to avoid target-mediated healthy tissue toxicity). In contrast, targeting a lower expressed tumor antigen requires a more potent payload to achieve a therapeutic concentration in targeted cells. Increasing payload potency typically results in higher toxicity, lowering the tolerated ADC dose. These lower ADC doses reduce tumor uptake but may not decrease healthy tissue uptake by the same amount (e.g. if target-mediated healthy tissue uptake remains saturated), potentially reducing the therapeutic index. Notably, this trade-off is very different than small molecule drugs, which often equilibrate with the plasma concentration such that a lower dose results in lower healthy tissue exposure. In stark contrast to small molecules, lower doses of more potent ADCs can limit tumor penetration, lowering efficacy more than toxicity.

High Antibody Doses

Developing ADCs against solid malignancies is difficult since solid tumors suffer from leaky, tortuous blood vessels and poor lymphatic drainage, leading to negligible convection and elevated interstitial pressure[117]. These features coalesce to form an adverse environment for the delivery of large biologics. The most direct way of increasing both antibody delivery and tissue penetration is to administer higher doses of the antibody. This is the second shared feature among currently approved agents.

Kadcyla was the only FDA-approved ADC for solid tumors for many years, having achieved FDA approval status in 2013 with the use of Human IgG1 scaffold, a moderate DAR (3.5 drugs per antibody), non-cleavable linker, and a potent microtubule inhibitor. Despite this success, it is difficult to extrapolate from a single example to provide guidance for designing new agents. In particular, the success of Herceptin, the antibody backbone of Kadcyla, makes it challenging to separate the role of the payload, antibody, and any potential synergy between them in the clinic[118]. With the approval of new agents that do not have apparent activity from antibody receptor blockade alone, the success associated with high dosing of these agents appears to extend beyond receptor signaling blockade. Current solid tumor therapeutics dose more antibody over a three-week period than Kadcyla and significantly more than many approved hematological ADCs (e.g. ~0.02 and 0.15 mg/kg for Besponsa and Zynlonta), ranging from 3.75 to 20 mg/kg (Table 4-1). These doses are needed to overcome high expression and efficient internalization which drives payload delivery into the cell.

Table 4-1. Structural components for the FDA-approved ADCs for solid tumor indications

FDA-approved ADCs for solid tumors (year)	Kadcyla (2013)	Padcev (2019)	Enhertu (2019)	Trodelvy (2020)
Target	Her2	Nectin-4	Her2	Trop-2
Antibody isotype	IgG1	IgG1	IgG1	IgG1
Clinical dose over 21 days[b] (mg/kg)	3.6	3.75	5.4	20
Linker	Non-cleavable (**SMCC**)	Cleavable (**VC**)	Cleavable (tetrapeptide)	Cleavable (**CL2A**)
Payload	Microtubule inhibitor (DM1)	Microtubule inhibitor (MMAE)	Topoisomerase inhibitor (exatecan derivative)	Topoisomerase inhibitor (SN-38)
Drug-to-antibody ratio	3.5	4	8	7.6
ADC clearance half-life (days)	4	3.4	5.7	0.67
Payload clearance half-life (days)	Not measured	2.4	5.8	0.75

These ADCs display differences in selected payload, linker, DAR, and conjugation. By contrast, the antibody isotype, large doses, and the high-expression target are shared by all these therapies. [b]Kadcyla, 3.6 mg/kg Q3W; Padcev, 1.25 mg/kg D1, D8, D15 of 28-day cycle; Enhertu, 5.4 mg/kg Q3W; Trodelvy, 10 mg/kg D1 and D8 of 21-day cycle.

Other Design Criteria

Payload selection is crucial to ADC development. The payload directly impacts the therapeutic window, which often plays a major role in clinical ADC attrition. Today most payloads belong to one of three classes: 1) DNA damage inducers, 2) microtubule inhibitors, and 3) topoisomerase inhibitors. DNA damaging payloads are often extremely potent (calicheamicin, pyrrolobenzodiazepine PBD) while microtubule (DM4, MMAE) and topoisomerase (exatecan, SN-38) inhibitors are more moderate. Identifying optimal payloads requires case by case analysis. A lower potency payload affords a greater maximum tolerated dose (MTD). However, for indications with lower antigen presentation, the amount of payload delivered might not exceed the therapeutic threshold, and so higher potency payloads would be necessary. In addition to *in vitro* potency, recent studies have identified multiple payloads as immunogenic cell death (ICD) inducing agents[105, 119, 120]. The ability of some payloads to cause an immune response after cell death is a new avenue of research that may have a broad impact on next generation ADC payload

selection, although the role of ICD versus IgG1 effector function or other mechanisms is currently unclear([105, 118, 119, 121] and Outstanding Questions).

While target expression, antibody dose, and antibody isotype are common to currently approved ADCs in solid tumors, there are important differences in the approved designs. For example, each linker is unique - some approved linkers are cleavable while others are non-cleavable. These differences can have a significant impact on the resulting distribution as well as treatment tolerability. Non-cleavable linkers are generally more stable in the plasma, although advances in linker chemistry have made significant improvements (e.g. Kadcyla's non-cleavable linker loses 18.4% of the DM1 payload in 4 days[122] versus Enhertu's cleavable linker loses 2.1% of its payload in 21 days[123]). Even if a linker can reduce ADC payload loss in circulation, a more difficult challenge is encountered after systemic uptake and degradation of the ADC itself. Since most of the ADC dose does not reach the tumor, the ADC will be metabolized somewhere else in the body, releasing the payload in an undesired location. The payload, linker, and conjugation site can all influence where non-specific release occurs in the body and the dose-limiting toxicity.

The current FDA approved drugs show variability across several of these other design features, demonstrating a need to individualize ADCs for their specific target. However, the similarities in dosing and target expression, combined with preclinical evidence, suggest that tissue penetration and tumor saturation are key components to solid tumor efficacy. Although tumor tissue penetration and saturation are linked to traditional measures of pharmacokinetics, such as C_{max} and exposure (area under the curve, or AUC), the unique distribution of ADCs may limit the association between AUC and efficacy often found with small molecule chemotherapeutics[124, 125].

Advancing ADCs to clinical trials without fully delineating tumor tissue penetration and saturation characteristics may be a significant factor in clinical attrition. In short, we need to move beyond C_{max} and AUC and account for tumor tissue penetration and tumor saturation to design the next generation of ADCs (Figure 4-1A).

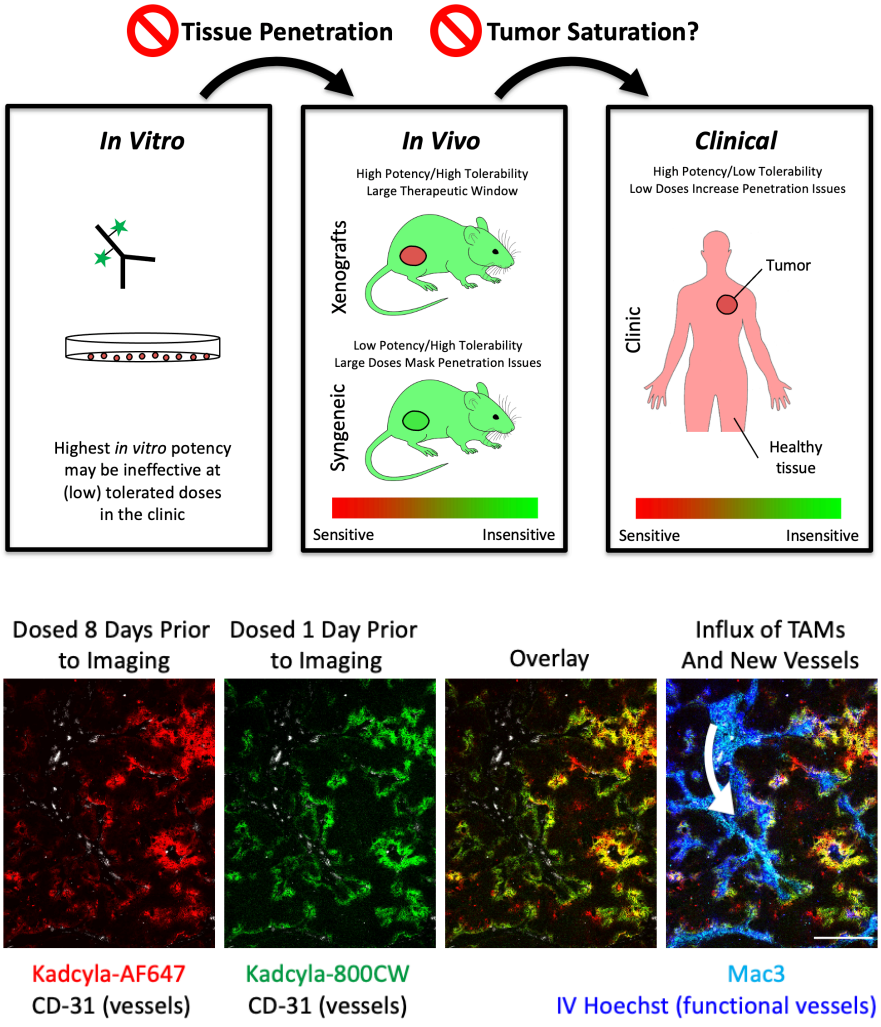

Figure 4-1. Scaling ADCs to the Clinic

A) Many reasons exist for the failure of animal models to capture clinical results in drug development. In the case of ADCs, two specific reasons include tissue penetration and tumor saturation. *In vitro* assays do not capture delivery issues, and highly potent compounds selected *in vitro* often increase toxicity, lowering tolerable doses *in vivo*. The lower doses result in less tissue penetration, reducing efficacy *in vivo* (left arrow). Mice often tolerate higher doses than humans, and mouse tumor lines are sometimes less sensitive to the payload. Both of these factors can result in higher doses administered in preclinical animal models (better tissue penetration), which sometimes results in tumor saturation. Notably, trends identified using saturating doses can be the opposite of those at subsaturating doses commonly encountered in the clinic (right arrow), making it critical to

understanding the saturation level in preclinical models and predicted level in the clinic. B) Nude mice bearing NCI-N87 xenografts were administered 1.2 mg/kg of AlexaFluor647 labeled Kadcyla on Day 0 and 1.2 mg/kg of IRDye800CW labeled Kadcyla on Day 7. Tumors were resected on Day 8, frozen in OCT, processed and imaged. Hoechst 33342 was injected 5 min before tumor resection to label functional vasculature. The first dose (red) shows strong colocalization with the second dose (green). A couple collapsed vessels were seen (data not shown) where perivascular signal from the first dose lacked Hoechst or signal from the second dose. Regions with a large number of macrophages (cyan) and functional vessels (blue) showed slightly stronger staining for the second dose, consistent with neovasculature forming (white arrow) following treatment[13].

ADC Delivery Challenges

Large biologics like ADCs suffer from two major delivery challenges: little ADC reaches the tumor and what does make it is poorly distributed. These challenges stem from multiple factors. After infusion, the ADC must travel from the injection site through the vasculature to the tumor. The large size of ADCs limits extravasation, so vascular permeability and vessel density/surface area are the rate-limiting factors in tumor uptake (versus blood flow for small molecules) [72] . While tumor vasculature is leaky, it is also tortuous and poorly distributed, resulting in lower tumor delivery compared to healthy tissue. This fact has been exploited in preblocking approaches (Zevalin [126], Bexxar, [127]). It's only through binding and retention that the tumor concentrations slowly rise above healthy tissue over time, but most of the ADC is metabolized throughout the body. Tumor delivery of ADCs is further exacerbated by the elevated interstitial pressure that tumors experience due to poor lymphatic drainage. The high interstitial pressure limits transport by convection and leads to diffusion-dominated tumor tissue penetration[111, 112]. Under these conditions, the high binding affinity of ADCs result in a common phenomenon first described as the 'binding site barrier'[110].

Clinical antibodies and ADCs are high affinity binders leading to a more rapid rate of binding than diffusion. Upon entering the tumor tissue, the ADC binds the nearest available target receptor. For highly expressed targets, free receptors typically outnumber ADCs, and the

combination of limited uptake, slow diffusion, and high affinity leads to perivascular uptake of ADCs. For unconjugated antibodies, patients often tolerate high doses enabling receptor saturation, but these doses are too toxic for ADCs due to their payload[115]. The continual internalization of targeted cells and dynamic tumor microenvironment prevent the ADC from ever reaching cells deeper in the tissue[13] , so few cells receive treatment.

While tissue penetration has not received as much attention as other aspects of ADC design, it is arguably equally (or more) important than many well-studied rates such as plasma clearance. Successful agents like Padcev and Trodelvy have fast plasma clearance rates (3.4 and 0.7 days respectively vs. 16 days for an antibody, trastuzumab), but their dosing enables efficient tissue penetration. Although delivery issues are not the only challenge in ADC design, their common occurrence makes it imperative to measure distribution for every ADC to ensure delivery isn't serving as a confounding factor leading to misinterpretation of results.

Tumor Saturation

Another critical aspect of translating preclinical models to the clinic is tumor saturation. This is dependent on a variety of conditions including dose (i.e. C_{max}), expression (receptors/cell), internalization rate[10, 116, 128], and plasma clearance among other considerations[129]. This is important due to a combination of two factors: a greater likelihood of using saturating doses in preclinical models and opposite outcomes from saturating versus subsaturating doses. First, the doses administered to mice do not always correspond to clinically tolerable doses. Sometimes, the doses are increased to account for faster clearance in mice or a less responsive tumor model, and other times, higher doses are given because they are better tolerated in mice. This can lead to saturation

in preclinical models while clinically tolerated doses may be subsaturating. Since mouse cells are often less responsive to ADC payloads than human cells, this can be further exacerbated in syngeneic models, where large doses are necessary for response (e.g. TUBO, Fo5 models). These large doses can overshadow delivery issues in the clinic, where ADC doses (3.6 and 6.4 mg/kg) may leave cells untargeted[130] versus higher doses attainable with unconjugated antibodies (e.g. 15 mg/kg of Margenza[131]). The second factor is that the outcome of preclinical studies under a saturating dose can yield the opposite result of the outcome under a subsaturating dose in the clinic. As described in examples below, increasing the DAR is more effective if a saturating dose is given, while decreasing the DAR can be more effective when a subsaturating dose is given. Typically, doses are limited by the payload toxicity, so comparisons are done at a constant payload dose.

When the tumor is super-saturated, cancer cells receive the maximum amount of antibody, so more payloads per antibody will deliver more payload per tumor cell, resulting in greater efficacy. The opposite is true for a subsaturating dose. Here, the ADC does not reach all the cancer cells, and increasing the DAR (at a constant payload dose) will lower the amount of antibody delivered, reducing the number of cells that are targeted and killed. Instead, decreasing the DAR and/or increasing the total antibody dose under these conditions can improve tissue penetration and overall efficacy[10].

To saturate a tumor with high target expression, a large C_{max} must be achieved, particularly when combined with the efficient internalization needed for payload delivery. Since C_{max} is related to the MTD, an ADC must be well tolerated to achieve saturating doses. Trodelvy operates in this regime as an ADC for solid tumors with a high DAR and moderate potency payload. Although this design goes against many traditional strategies, the moderate potency payload provided a

greater range in tolerability for optimizing the DAR. In a 2015 study by Goldenberg et al., the DAR was varied from 1.64 to 6.89 drugs per antibody. When ADCs with varying DARs were delivered at equivalent, saturating doses of ~20 and 40 mg/kg, the higher DAR of 6.89 payloads per antibody provided a significant improvement in survival when compared to lower DAR variants[104]. This study demonstrated that a higher DAR can be beneficial for a well-tolerated, moderate potency payload when tumor saturation can be achieved.

Similarly, mirvetuximab soravtansine is capable of saturating tumors at doses of approximately 6 mg/kg[132]. In a mouse study utilizing ADCs with varying DAR, Yoder et al. demonstrated that a higher DAR (3-4 payloads per antibody) was more effective than the same payload dose delivered via a site-specific DAR2 variant. Comparisons showed 6 mg/kg of the higher DAR was more effective than 12 mg/kg of the DAR2, and 12 mg/kg of the higher DAR was more effective than 24 mg/kg of the DAR2[133]. While the linker conjugation chemistry is different, the results are consistent with the concept that a higher DAR is more effective when a saturating dose of antibody is delivered. In contrast, when a subsaturating antibody dose is delivered (< 3 mg/kg), efficacy can be improved by adding a carrier dose[116].

Based on the above comparisons, the payload MTD should be linked to a saturating dose of the antibody for maximum tissue penetration and efficacy. The payload MTD will depend on the specific payload, while the saturating antibody dose will depend on tumor and target characteristics. A potential caveat to this generalization stems from the payload itself. Depending on the physicochemical properties of the payload, the payload may be able to escape a targeted cell and diffuse to an adjacent cell to enact cell death in a process known as the ‘bystander effect’.

Role of bystander effects

The three recently approved ADCs for solid tumors all use a payload capable of bystander killing. A bystander payload can diffuse out of a targeted cell following release and into an adjacent cell. The ability to reduce one of the common resistance mechanisms, antigen negative cancer cells, with bystander payloads has drawn a considerable interest in this area. In theory, bystander payloads are also capable of improving tissue penetration beyond what is achieved by the antibody itself[60, 134]. This may explain the increased efficacy displayed by Enhertu when compared to Kadcyla in NCI-N87 mouse models despite similar cellular potencies[13, 123]. Likewise, only Enhertu has been approved for use in gastric cancer with more heterogeneous HER2 expression[135, 136]. However, increased tissue penetration from higher antibody doses still increases efficacy even when using ADCs with bystander payloads[92, 137-139]. While bystander payloads can improve distribution, the efficiency of direct delivery by an antibody is greater than bystander killing[60], which explains the greater efficacy from higher antibody doses even with bystander payloads.

4.4 Conclusions

ADCs are complex biologics with three main components that can be modified in numerous ways. While these modifications can improve the efficacy of ADCs, it has been difficult to identify key features of ADC design that lead to clinical success. Over the last couple decades, target selection, linker stability, and toxicity have been at the forefront of the design process. A failure in any of these categories would be cause for concern and likely shut down an ADC in the pipeline. Even so, many ADCs that appear promising in preclinical studies ultimately fail in clinical trials due to toxicity and/or a poor therapeutic window. Here, we argue that tissue

penetration and tumor saturation are essential measurements in the development of ADCs. The results highlighted in this work show the importance of tissue penetration and its complex relationship with dosing and ADC design. It is important to note that strategies to improve tissue penetration will only work under subsaturating conditions. While this may be common in the clinic, tumor saturation can more readily be achieved in animal models, potentially confounding efforts to scale to the clinic. Therefore, preclinical studies need to collect data regarding the most important parameters for efficacy, including tumor penetration and saturation. In an ideal design scenario at least two pieces of information would be known: the tolerable payload dose in humans and the antibody dose required to saturate the target in the tumor. With this information, an upper limit can be set on the total payload delivered which can be matched by modifying the DAR. The technique would deliver the most payload tolerable while targeting all tumor cells with the goal of maximizing efficacy at clinically tolerable doses.

Chapter V

Rapid Biparatopic Antibody Internalization Improves Efficacy in 'Non-internalizing' CEA Positive Colon Cancer Model

5.1 Publication Information

Nessler, I., A. Kopp, and G.M. Thurber. *Rapid Biparatopic Antibody Internalization Improves Efficacy in 'Non-internalizing' CEA Positive Colon Cancer Model*. In prep.

Modifications have been made to the published document to adapt the content to this text. Previous chapters 2, 3, and 4 demonstrated the importance of internalization rate for tumor penetration and efficacy under subsaturating dosing consistent with extremely potent ADCs. In this chapter, I explore lower potency ADCs that can deliver suturing doses and identify a rapid internalization rate as a way to improve efficacy for lower expression and/or slower internalizing targets.

5.2 Abstract

Solid tumor antibody-drug conjugates (ADCs) have experienced more clinical success in the last three years than the previous 17-year span since the first ADC approval in 2001. While recent advances in protein engineering, linker design, and payload variations have played a significant role in this success, high expression and readily internalized targets have also been crucial to solid tumor therapy. However, these factors are also connected to poor tissue penetration

and lower efficacy, making it unclear when faster or slower internalization will be most effective. While potent payloads may benefit from slower internalization to increase tissue penetration, less potent and more tolerable payloads can achieve saturating doses. In this work, we demonstrate the ability of a biparatopic antibody to deliver more payload to a slow (or 'non') internalizing target, carcinoembryonic antigen (CEA) resulting in improved efficacy in a colorectal carcinoma animal model. When a saturating dose of ADC can be delivered, cross-linking ADCs increase the total payload delivery on a per cell basis. Although slowly internalizing antigens have been considered by some as less desirable ADC targets, cross-linking ADCs may enable the targeting of tumor antigens that were previously deemed undesirable due to slow internalization.

5.3 Background

ADCs are complex therapeutics that combine the potent cell-killing ability of small molecule payloads to a cancer targeting monoclonal antibody. Numerous clinical failures and only one approval for solid tumors after more than two decades of effort led many companies to pull back on ADC development. However, over the past three years, ADCs have experienced rapid growth with six new FDA approvals. Four of these recent approvals are for solid tumor indications where the bulky ADC encounters many delivery challenges due to its size[8]. Recently approved solid tumor ADCs administer large doses (similar to unconjugated antibody therapeutics) and use an IgG1 isotype antibody known for its long circulating half-life, which can overcome many delivery challenges[16]. A large antibody dose is required for tumor penetration in high expression systems with rapidly internalizing targets as the antibody has to overcome cellular internalization to diffuse further into the tumor tissue[140]. The recent approval of Trodelvy exemplifies the successful application of this strategy for solid tumor ADCs.

With a total 20 mg/kg dose over a 21-day treatment cycle, Trodelvy employs the highest dosing of any FDA approved solid tumor ADC. The Trop-2 binding antibody is linked to as many as 8 payloads through a hydrolysable linker directly contradicting some of the long-held beliefs of potent payloads and stable linkages for successful ADC design[104, 141]. The mechanisms by which Trodelvy achieves a positive therapeutic window are not fully understood. The reduced linker stability may lower toxicity from target-mediated uptake in healthy tissue, while in the tumor the payload may be cleaved extracellularly to diffuse deeper for 'bystander' killing or the linker could increase intracellular cleavage rates[142, 143]. Computational and experimental work from our group indicates intracellular release is more efficient at cell killing than bystander killing[14]. Therefore, the rapid internalization rate of TROP2 and fast linker cleavage may both be required for clinical efficacy. While Trodelvy has garnered success, a similar ADC utilizing the same linker/payload and similar DAR against CEA (IMMU-130) has shown fewer responses so far in the clinic. While there are likely multiple explanations for the varied success, the difference in tumor target may play a key role. CEA, like many potential tumor targets (e.g., CD19, CD21, A33)[41, 144, 145] demonstrates a slow internalization rate reducing the direct delivery of payload. Well-tolerated ADCs can be administered at high doses, which can fully saturate slowly internalizing and/or moderately expressed tumor antigens. In this dosing regime, reducing the internalization rate to increase penetration (as shown in PSMA system, Chapter 3) to improve efficacy is not feasible can instead limit payload delivery below the required therapeutic threshold. To drive internalization and increase efficacy a cross-linking antibody scaffold with a rapid internalization rate may improve cellular delivery above a therapeutic threshold.

Previous studies have isolated the impact of receptor engagement on internalization[72, 128, 144]. In a publication by Schmidt et al.[144], the internalization rate of antibody fragments and antibodies with varied binding characteristics to CEA were analyzed. While almost all the tested proteins exhibited an internalization half-life consistent with the constitutive turnover rate of the unbound receptor (~14.5hr), a biparatopic antibody had a significantly shorter half-life for internalization (~5hr) and twice as many bound proteins at saturation. The result of this work shows the potential for a biparatopic antibody to drive faster internalization and potentially improve cellular payload delivery, consistent with our previous work on biparatopic PSMA conjugates[128].

In this study, we investigated the pharmacokinetics (PK) and pharmacodynamics (PD) of previously characterized anti-CEA antibodies (HMN-14 & M85151A) and their SN38 conjugated ADCs (IMMU-130 & Xab-SN38). Fluorescently conjugated antibodies were administered in vitro and in vivo to study the impact of biparatopic binding kinetics on tissue and cellular level delivery as well as identifying a tumor saturating dose. ADCs were then delivered at this saturating dose in a CEA expressing tumor model to compare efficacy of the biparatopic ADC to a standard ADC. The experimental results in tandem with a computational Krogh cylinder model identify the tumor conditions where biparatopic ADCs demonstrate increased efficacy.

5.4 Results

The delivery of payload under tumor saturating ADC doses, with similar clearance and molecular weight, is predicted to depend significantly on the binding and internalization kinetics. While previous work showed that fast internalization could be detrimental with potent payloads[128], the opposite trend was predicted when a saturating dose of antibody is used. To test this prediction,

we set out to explore the potential for improved efficacy against a tumor neoantigen (CEA) that is considered slow or non-internalizing by utilizing a biparatopic ADC capable of driving internalization (Figure 5-1).

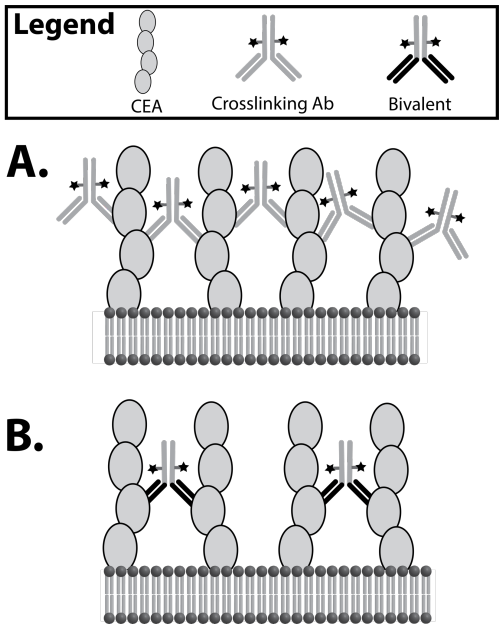

Figure 5-1. Graphic of binding for XAb and Bivalent

A+B) Crosslinking Ab can bind to two locations on each CEA receptor providing a larger binding occupancy and crosslinking while bivalent antibody can only bind to one site per receptor.

In vitro internalization, efficacy, and pharmacodynamic marker staining of ADCs

The effective cellular internalization rate constant (k_e) was determined utilizing a fluorescence quenching protocol as previously described[128, 144]. LS174T cells were incubated at 37°C in continuous presence of a saturating concentration of Alexa Fluor-488 conjugated antibodies. For both antibodies, total and surface fluorescence increased over the course of the experiment. While the surface fluorescence was expected to plateau after 1 hour due to binding equilibrium, LS174T cells can form tight junctions increasing the time for binding equilibrium and delaying surface fluorescence plateau (Figure 5-2A). The main difference between XAb and HMN-14 conjugates was measured in the internalized fluorescence corresponding to differing

internalization rates. The internalized fluorescence for XAb increased throughout the 8-hour incubation while HMN-14 internalized fluorescence tapered off towards the end of the continuous incubation.

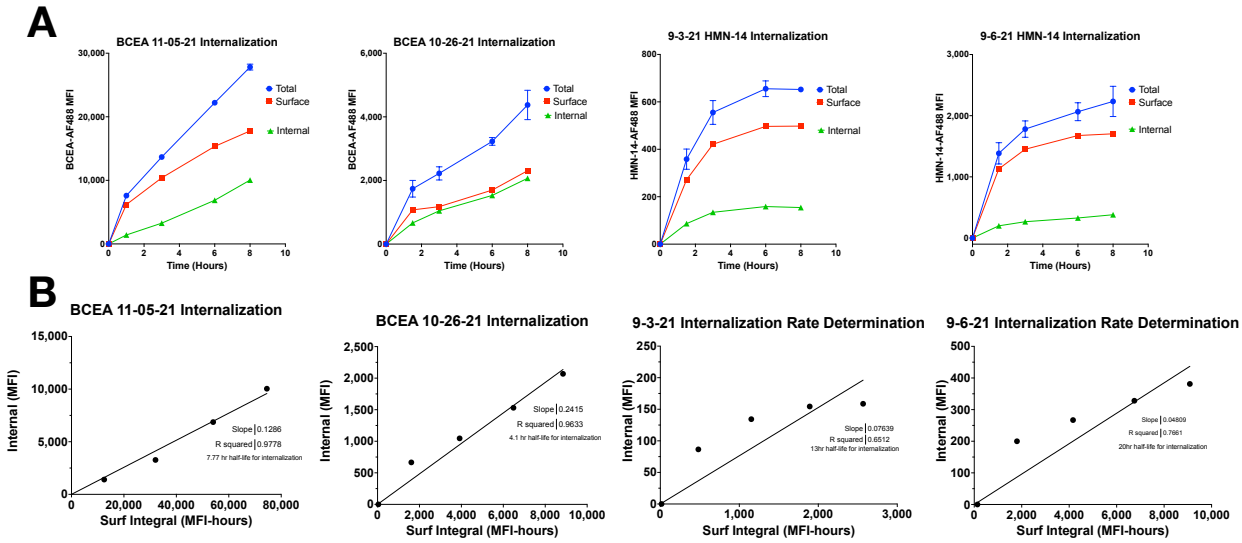

Figure 5-2. Internalization rates were measured for both XAb and HMN-14 antibodies.

A) Total, internal, and surface fluorescence was measured over time for both XAb and HMN-14. B) This data was then fitted to calculate an internalization rate. As previously described, XAb demonstrated an increased internalization rate. HMN-14 measurements were not as accurate but were in line with the constitutive turnover rate of CEA and other CEA antibodies.

The data from Figure 5-2A was used to determine the time integral of the surface fluorescence and plotted against the internal fluorescence. A linear fit (Figure 5-2B) was used to calculate the fitted slope which corresponds to k_e. The half-life is reported for each experiment where $t_{1/2}= \ln(2)/k_e$. The two antibodies differed greatly in internalization rate as expected based on the known kinetics of constitutive turnover of CEA and the biparatopic antibodies capability to drive internalization[144]. XAb internalization rate was measured in our hands to be ~6 hours while the HMN-14 antibody, demonstrated a slower internalization rate consistent with the constitutive turnover of the CEA receptor at ~16.5 hours (Figure 5-2B.).

IMMU-130 and the XAb-SN38 ADCs were tested for in vitro potency against CEA expressing LS174T colorectal cancer cells. A PrestoBlue viability assay was conducted after a 6-day incubation with either daily or no media replacement (Figure 5-3). Both ADCs demonstrated similar potency in vitro even with media replacement to remove payload released by hydrolysis in the media. This is similar to results seen with Trodelvy[104], where the in vitro results (which lacks continuous washout present in vivo) are consistent with the potency of free payload. However, previous work indicates that intracellular release is more efficient at cell killing than bystander killing[15]. We suspected that the time frame for cell death may be too slow to capture differences from in vitro internalization.

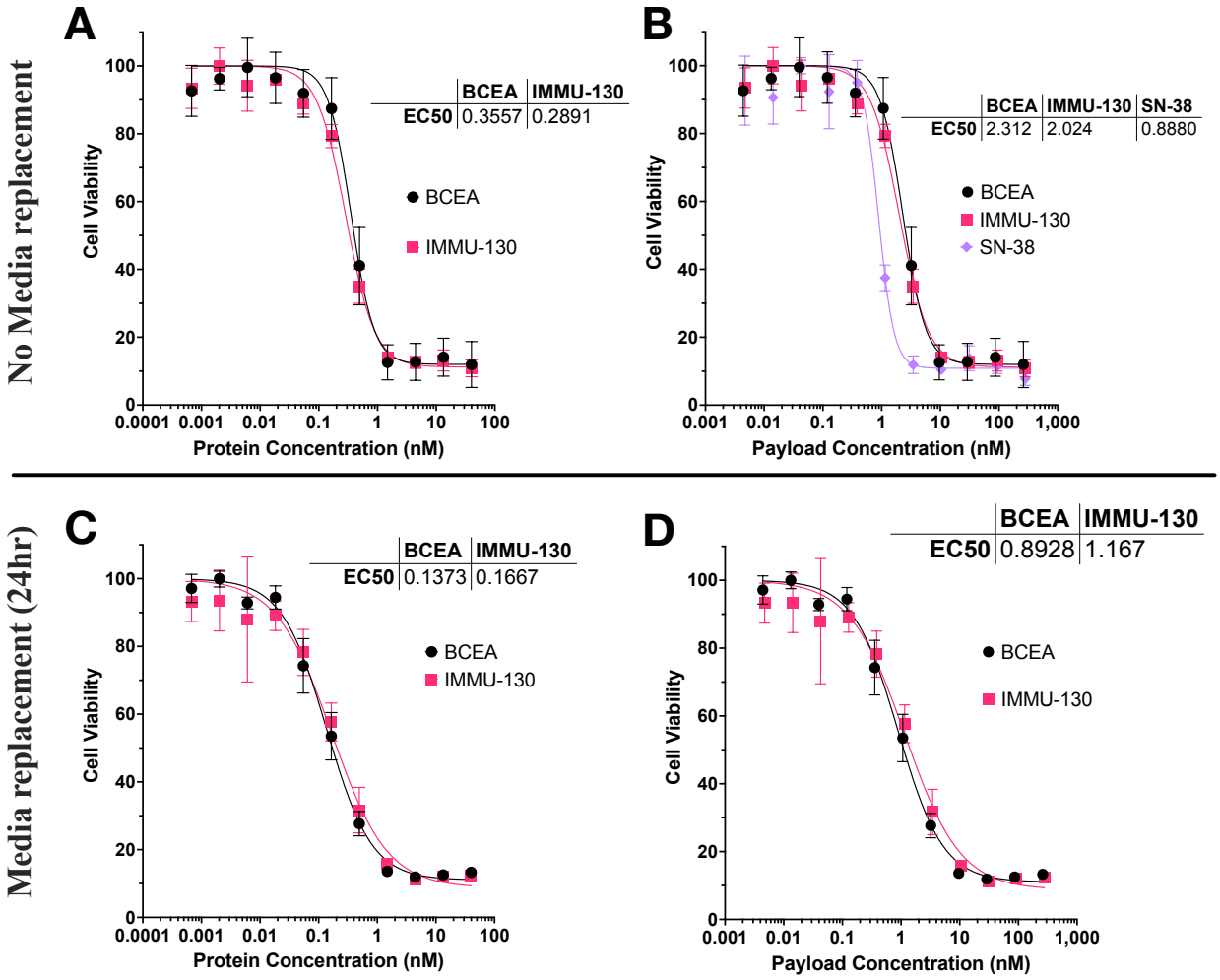

Figure 5-3. in vitro potency for XAb and IMMU-130

A+B) in vitro potency was tested over six days without media replacement. C+D) tested in vitro potency with daily media replacement.

To capture potential differences from faster internalization, a pharmacodynamic marker with a pulse-chase format was utilized. LS174T cells were seeded in 96 well plates and pulsed 4 consecutive times (2 hours each) followed by a 48-hour chase in non-ADC containing media (to avoid continuous hydrolysis of free payload). Short pulse times limited extracellular release of SN-38 in favor of direct payload delivery by the degradation of internalized ADC, thereby isolating the impact of internalization rate on PD signal. Under these saturating conditions, the PD signal was higher for the XAb-SN38 than Immu-130, and both surpassed incubation with free payload

(Figure 5-4). This experiment demonstrated the ability of XAb-SN38 to cause increased PD signal compared to IMMU-130 when the ADC targets the cell surface but is then removed (cleared) from the system.

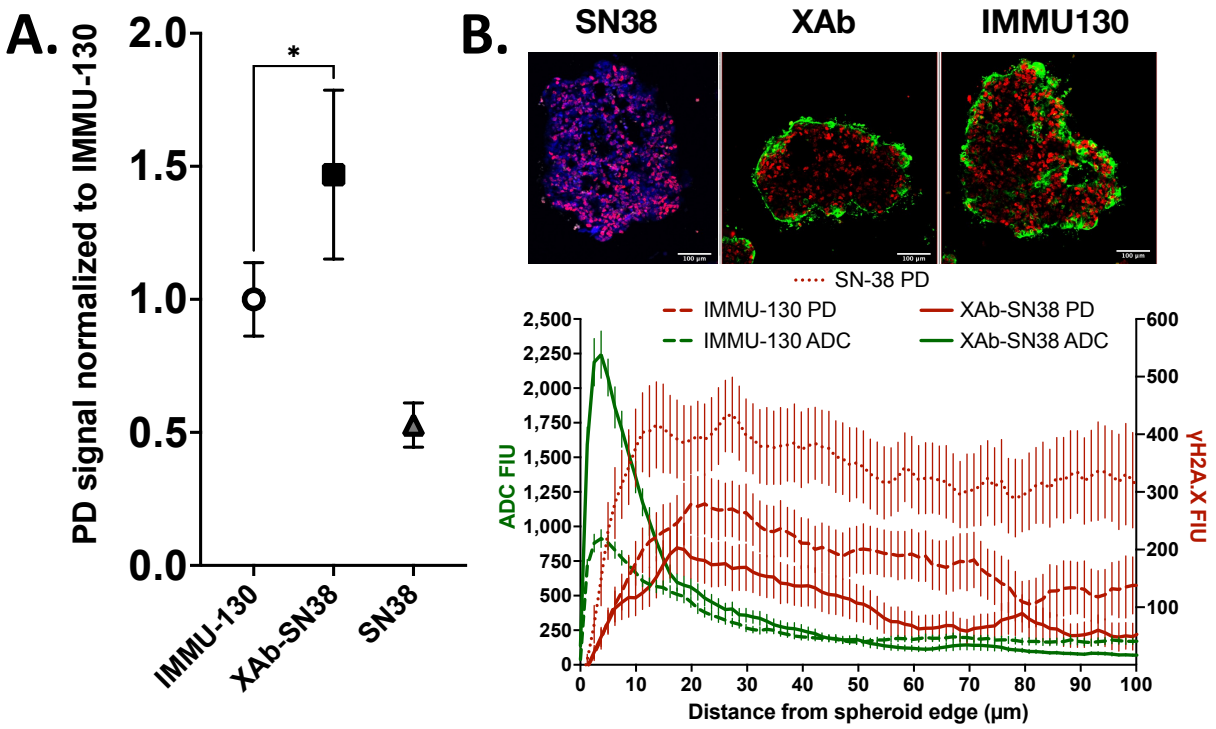

Figure 5-4. XAb-SN38 and IMMU-130 DNA damage

A) Measured DNA damage with gamma-H2AX staining in vitro. Without delivery limitations, XAb provided greater PD signal at the same incubation concentration. B) Under subsaturating conditions delivery of the XAb was hindered by binding and internalization reducing PD signal away from the spheroid periphery.

SN-38 Exhibits Bystander Killing in Spheroids

The free payload toxicity and SN-38 physicochemical properties are consistent with the ability of the payload to exhibit bystander killing. Given the hydrolysis of the CL2A linker used in both the XAb-SN38 and Immu-130 (and Trodelvy), we imaged the PD marker in spheroids following a subsaturating incubation with ADC. Under these conditions, only the peripheral cells are exposed to ADC, so PD signal in cells in the middle are indicative of bystander effects.

LS174T cells were also seeded in a 384 well hanging drop plate to form spheroids over the course of 7 days and then incubated with subsaturating ADC concentrations to study the impacts of the SN-38 bystander effect. All conditions showed some PD signal in the spheroid center, consistent with SN-38 bystander effects (Figure 5-4). Interestingly, the bystander killing of Immu-130 was greater than the XAb-SN38, which may be consistent with more efficient bystander killing when the payload is released outside the cell versus inside an adjacent cell. While the crosslinking XAb-SN38 did demonstrate improved delivery to peripheral cells, PD signal in these cells did not demonstrate a direct correlation to the improved delivery. The increased binding sites and internalization rate of XAb-SN38 greatly limited penetration but improved individual cell uptake at the periphery of the spheroid. IMMU-130 with a slower internalization rate, was able to penetrate further towards the center of the spheroid and demonstrated improved PD penetration according to the Euclidean distance map in (Figure 5-4C).

XAb-SN38 and IMMU-130 exhibit similar uptake and tumor saturation at tolerable doses

The higher PD signal from the cross-linking ADC in monolayer culture (cell saturating conditions) indicated this format may deliver more payload and increase efficacy in vivo where release payload is subject to continuous washout from the tissue. However, the lower signal in subsaturating tumor spheroid conditions indicated this could be depending on dosing. To determine if the internalization rate impacted efficacy, the tumor uptake and distribution had to first be measured to eliminate these confounding effects.

Fluorescent naked antibodies were injected into nude mice bearing CEA-positive LS174T cells in the left flank. Both the biparatopic and HMN-14 antibodies exhibited long residence times in the blood and no statistically significant differences in tumor uptake, although the median XAb

uptake was greater than the median HMN-14 uptake for both 10mg/kg and 20mg/kg doses (Figure 5-5). Comparing the two dosing schemes, tumor uptake was decreased in the 20mg/kg IV delivery when compared to the 10mg/kg dose.

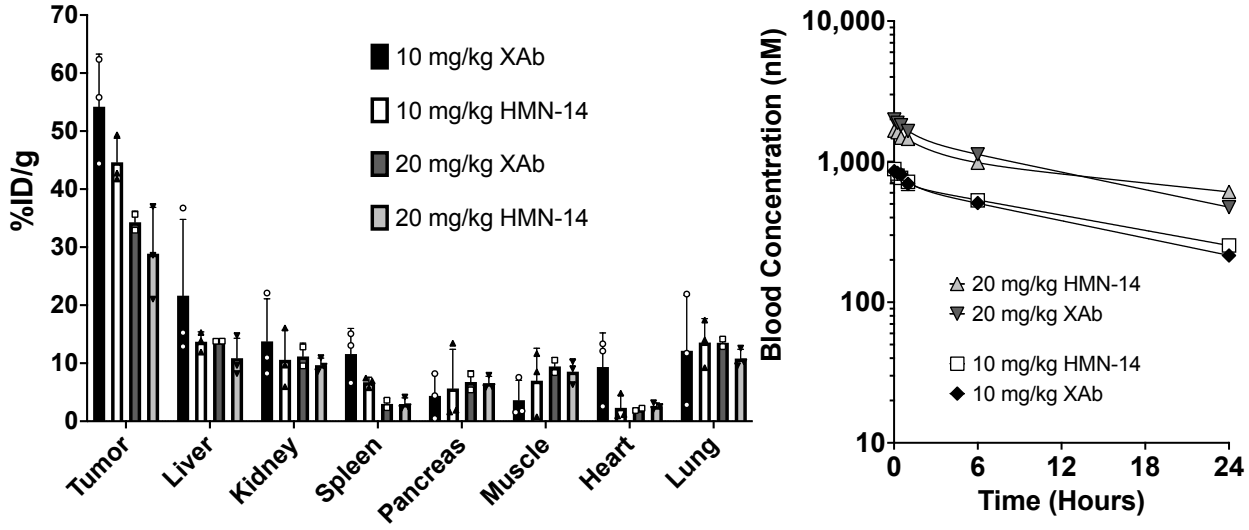

Figure 5-5. Organ level distribution

A) Organ distribution was measured 24 hours after fluorescent antibody administration. B) Pharmacokinetics was measured via retro-orbital blood sampling over the course of 24 hours.

To further analyze the distribution, ADC uptake at the tissue and cellular level was analyzed. Confocal imaging of tumor histology following 10 and 20 mg/kg showed uniform distribution throughout the tumor, consistent with target saturation (Figure 5-5A and Figure 5-6A). To confirm that the XAb was more rapidly internalized in vivo, we utilized a dual-fluorescent labeling technique to quantify antibody degradation. Using residualizing and non-residualizing near-infrared fluorophores, the non-residualizing dye washes out of the tumor faster for more quickly internalized and degraded ADCs. Consistent with the in vitro results, the intact ratio decreased more quickly for the XAb than HMN-14, demonstrating statistically faster internalization in vivo for the crosslinking antibody (Figure 5-6B)

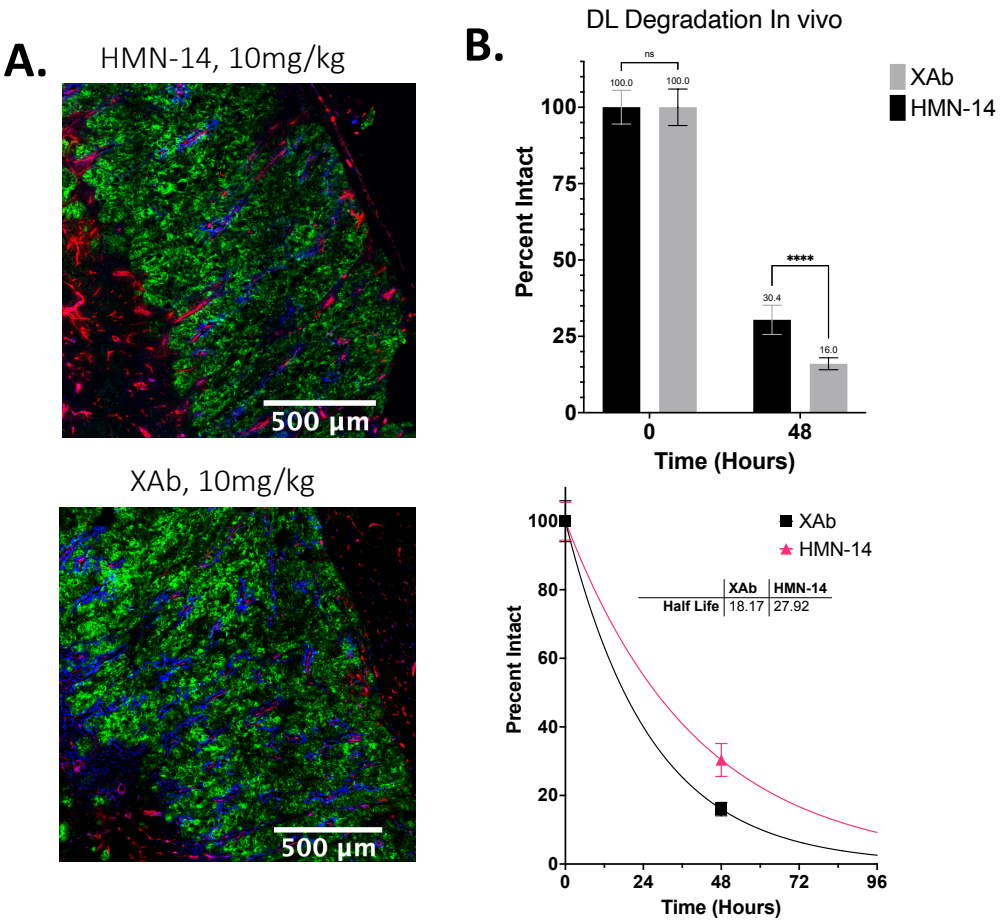

Figure 5-6. Tumor saturation and degradation

A) Confocal imaging of tumor saturation with both antibodies after 24 hours. Blood vessels in red, nuclei in blue, and antibody in green. B) In vivo degradation of XAb and HMN-14 over the course of 48 hours.

In vivo Efficacy Study

To determine if the saturating dose of XAb-SN38 was more effective than Immu-130, we conducted an efficacy study. A dose of 10 mg/kg was chosen based on the clinical tolerability of Immu-130 and tumor saturation at this dose. The high expression LS174T xenograft model was used to measure efficacy. Because of its extremely rapid growth, biweekly dosing was used instead of weekly dosing in the clinic. Following 4 doses, Immu-130 showed growth inhibition of tumors, but XAb-SN38 was able to achieve tumor regression (Figure 5-7A). Not only did XAb-SN38

demonstrate improved anti-tumor efficacy, XAb-SN38 also increased overall median survival to 36 days when compared to IMMU-130 (24 days) and the vehicle control (8 days).

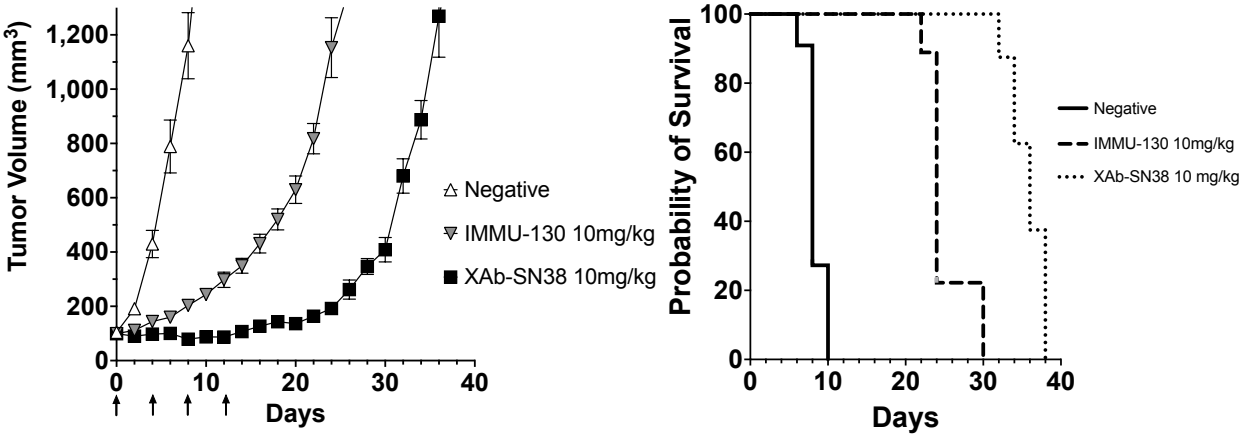

Figure 5-7. Tumor efficacy and survival

Tumor efficacy demonstrated by 10mg/kg doses of IMMU-130 displayed significant differences in efficacy compared to XAb. B) The increased tumor inhibition resulted in statistically significant increase in survival.

Mouse weights were tracked as a crude but available measure of toxicity. Both Immu-130 and XAb-SN38 had similar losses in body weight of approximately 10% (Figure 5-8). The negative control animals also had a similar loss in weight which was attributed to the large and rapidly growing tumors.

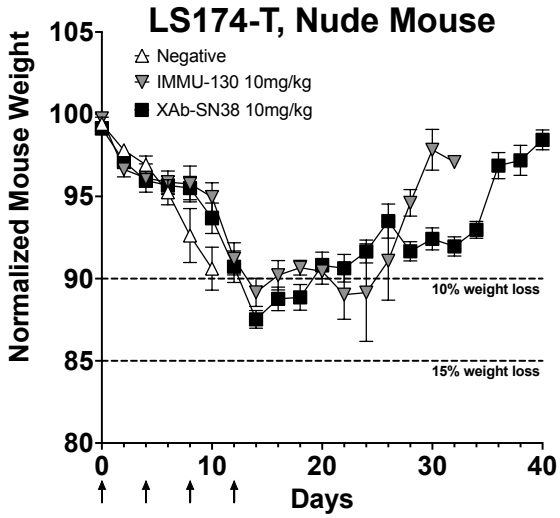

Figure 5-8. Mouse weights

Mouse weights were monitored during the efficacy study as a crude measure of treatment tolerability

5.5 Discussion

Overall delivery of solid tumor ADCs is limited by PK and extravasation while tumor penetration is further dependent on diffusion and binding kinetics. When comparing two separate ADCs that have similar PK and molecular weight, the key factor to differences in tumor penetration and cellular delivery is binding and internalization. Additionally, the differences in delivery are predicted to vary depending on whether a saturating/non-saturating dose is delivered. Previous work under non-saturating conditions with potent ADCs targeting PSMA demonstrated slower internalization rate as beneficial to improve penetration, targeting more cells with a therapeutic concentration[128]. A slow internalization rate limits the degradation and subsequent release of payload at the site of action but can aid in tumor penetration for nonsaturating doses by blocking binding sites close to the blood vessel and/or allowing for further diffusion before internalization. This potentially overcomes the binding site barrier/saturation front but at the cost of delivering a lower amount of payload per targeted cell. In contrast, rapid internalization fuels the binding site barrier and concentrates payload near the blood vessel unless a saturating dose can be delivered. If the maximum tolerated dose is high enough to saturate the tumor, a rapid internalization rate is beneficial to delivering payload. As solid tumor penetration and saturation begin to serve as metrics for clinical development, a new standard of better tolerated ADCs is emerging.

The recent FDA approved solid tumor ADCs are changing the design paradigm. In particular, the counter-intuitive design of Trodelvy consisting of a less stable linker (CL2A) and high DAR (7.6 payloads per antibody) of a moderate potency payload has challenged the dogma of increasingly stable linkages and high potency payloads. Trodely's design and dosing strategy

allows for a total of 20 mg/kg to be delivered over a 21-day treatment. While the clearance of Trodelvy is relatively rapid (0.67-day half-life), the large dose results in a large C_{max} which supports tumor penetration for extravasation limited agents like ADCs. The unconventional CL2A linker has a half-life of ~1 day in serum and is pH cleavable. This has led to a complex discussion on the main driver of efficacy and the relative impacts of extracellular SN-38 release vs. rapid linker cleavage in lysosomes. In this study, an exploration of the impact of direct payload delivery on tumor efficacy via rapid internalization was investigated for a target under clinical consideration.

The two ADCs explored in this work leverage the novel design of Trodelvy (CL2A linkage and 6-8 SN-38 drugs per antibody) but are targeted against a slowly internalizing CEA positive colorectal cancer. A slow internalizing receptor provides a longer period for extracellular cleavage of SN-38 in the intercellular space leveraging this mechanism of action. However, the known extracellular cleavage makes measuring in vitro potency of the ADCs difficult[104]. While measuring the in vitro potency of cancer therapeutics is a traditional checkpoint for progressing to preclinical models, ADCs consisting of the CL2A linker release SN-38 with a half-life of 20hr in media. Thus, long term in vitro potency assays (e.g. 6-days) tend to measure the free payload potency instead of the ADC potency. Even with daily replenishment, both the fast-internalizing XAb-SN38 and the slower internalizing HMN-14 demonstrate similar potencies in the single digit nM range (Figure 5-3). This potency was similar the free SN-38 payload potency. Potency measured in traditional in vitro assays for stable ADCs depend on the net internalizing rate, payload potency, linker, and receptor expression. However, in this experiment extracellular SN-38 dominates the measured potency (Figure 5-3).

Interestingly, in vivo Tumor growth curves depicted significant differences in efficacy (Figure 5-7) despite similar cell killing capabilities in vitro. Both IMMU-130 and XAb-SN38 were delivered in four separate tumor saturating doses of 10 mg/kg. However, IMMU-130 led only to moderate growth inhibition while XAb-SN38 demonstrated tumor regression resulting in statistically improved efficacy and survival. In monolayer cell culture, there is no removal of degradation products such that SN-38 payload, which is readily cleaved from CL2A, continues to build up over time until media replacement. In vivo, the blood can act as a sink to remove large concentration build ups of payload in the tumor interstitium via wash out potentially advantaging direct payload delivery via internalization over extracellular release.

Although HMN-14 is a human IgG1 and XAb a mouse IgG1, the clearance of these antibodies was similar over the course of 24 hours suggesting comparable tumor exposure (Figure 5-5B). Biodistributions of tumor bearing mice conducted 24 hours after fluorescently conjugated antibody was delivered at 10 and 20 mg/kg further confirmed similar tumor exposures and did not yield statistically different uptake in any tissues collected (Figure 5-5A). Although biparatopic antibody can bind twice as many antibodies per cell when compared to HMN-14 (due to the different epitope binding of each arm), the differences in total antibody delivered to the tumor was statistically insignificant. The higher, yet not statistically significant, uptake for XAb-SN38 is likely due to a combination of increased binding sites and receptor downregulation[144] that partially counteract each other to modestly increase tumor uptake. With similar overall levels of ADC delivered to the tumor, a similar amount of payload would also be delivered at the tumor level. The key difference being that IMMU-130 would theoretically release more payload extracellularly as it lingered on the cells surface due to slow internalization while XAb-SN38 would drive direct payload delivery to the cell via rapid internalization. An in vitro experiment was conducted

involving short term pulses to limit extracellular release of SN-38 and highlight the differing internalizing rates and the impact on PD signal.

To isolate internalization rate and direct payload delivery, ADC concentrations were pulsed for two hours, four total times and then replaced with fresh media and incubated an additional 48 hours. The pulsed incubation limits free SN-38 interaction and favors ADC driven PD resulting in statistically significant differences in PD signal for XAb-SN38 and Immu130 (Figure 5-4A). However, these experimental conditions are not representative of potential penetration limitations in vivo. To analyze protein and payload gradients that are present in vivo we utilized an in vitro 3D tumor spheroid model. A non-saturating concentration of each ADC was incubated for 8hrs, then media was replaced and chased for 48hrs. Anti-Fc, nuclear, and PD staining was conducted ex vivo to identify the limited penetration of the ADC and explore the potential of SN-38 to exhibit bystander effects deeper in the tumor (Figure 5-4). All tested ADCs resulted in PD signal which penetrated further than the ADC front. XAb-SN38 demonstrated improved binding and delivery of ADC to peripheral cells when compared to IMMU-130. However, IMMU-130 was able to penetrate further into the spheroid, likely due to the limited internalization rate. As seen in previous work, PD signal at the periphery was limited potentially due to the time dependent nature of peak PD signal or other undetermined reasons[14]. The Euclidean distance map demonstrated similar PD signal for both XAb-SN38 and IMMU-130 but greater PD for IMMU-130. Constant incubation in 270nM SN-38 over the 8-hour incubation resulted in greater PD signal than either ADC corresponding to SN-38 ability to enter through cellular membranes and enact DNA damage. The implications of these results were then explored in an in vivo tumor model measuring uptake and degradation.

Utilizing the dual label approach, the in vivo cellular degradation rate of XAb and HMN-14 were analyzed 48 hours after the first 10mg/kg injection in LS-174T tumor bearing mice (Figure 5-6). In accordance with the internalization rate measured in vitro (Figure 5-2), the cross-linking antibody demonstrated increased degradation relative to HMN-14. Biodistribution data (Figure 5-5) demonstrates that a similar total amount of ADC is delivered, however, given the increased degradation rate of XAb-SN38, a greater fraction of payload is delivered directly to tumor cells when compared to IMMU130. The modest increase in tumor uptake and statistically significant difference in direct delivery through ADC degradation results in the improved efficacy and median survival for LS-174T bearing mice (Figure 5-7).

5.6 Conclusion

ADCs targeting solid tumors are challenging to develop, but recent success highlights a path forward. While recent approvals highlight high expression antigens as a similar feature for success, many potential tumor targets have been avoided due to lower expression and/or slow internalization. One potential example is CEA which expresses ~388k receptors in the LS174T model and a constitutive turnover rate of ~15hr. A bivalent ADC (IMMU-130) can deliver enough payload to cause growth inhibition when delivered in multiple high dose administrations over a 12-day period. Considering the cleavable nature of the CL2A linker used in IMMU-130's design, it has been postulated that extracellular release of payload in the tumor interstitium may account for much of the efficacy seen with IMMU-130. While extracellular release of SN-38 may play a role in efficacy, increasing delivery of payload via a cross-linking ADC (XAb-SN38) with a rapid internalization rate increased survival and additionally caused tumor regression. These results do not eliminate extracellular SN-38 release as a contributor to anti-tumor efficacy but instead

highlight that increasing the direct delivery of SN-38 via antibody internalization and subsequent degradation is more efficacious.

5.7 Experimental Methods

Computational model—Krogh cylinder

The Krogh cylinder model has been validated for tissue distribution of antibodies by our group and others[8, 87, 96-98]. A 2-D cylinder model consisting of only radial gradients was used to represent the distribution of antibody constructs since depletion along the blood vessel is negligible. Free target as well as free, bound, and internalized antibody were simulated. In brief, the equations describe the rate of antibody extravasation from a blood vessel, diffusion through tumor tissue and subsequent binding to a CEA followed by internalization and degradation. All parameters used in this predictive Krogh cylinder were gathered from the literature or measured independently.

Antibody and imaging agents:

Alexa Fluor 488 (AF488), Alexa Fluor 647 (AF647), or Alexa Fluor 680 (AF680; Thermo Fisher Scientific) were conjugated to each antibody through NHS ester lysine chemistry. Briefly, NHS ester dyes were reacted with XAb (7pM[144]) and HMN-14 (8.4nM) in aqueous solution buffered with 7.5% sodium bicarbonate for 2 hours with gentle stirring at room temperature. The reaction mixture was filtered with a Costar Spin-x Centrifuge Tube Filter (Thermo Fisher Scientific) containing P6-Biogel to remove unreacted dye. The filtrate degree-of- labeling (DoL) was <0.5 for in vivo applications and approximately 1 dyes/protein for in vitro work as confirmed with absorption readings from a NanoDrop 1000 Spectrophotometer.

Cell Culture and Animals

The LS174T cell line were purchased from ATCC. Cells were cultured two to three times per week up to passage number of 25 and grown in EMEM supplemented with 10% (v/v) FBS, 50 U/mL penicillin, and 50 mg/mL streptomycin at 37°C with 5% CO2. Annual mycoplasma testing was conducted using the Mycoalert Testing Kit (Thermo Fisher Scientific, NC9719283). All animal studies were approved and conducted in compliance with the Institutional Animal Care and Use Committee of the University of Michigan (Ann Arbor, MI) and Association for Assessment and Accreditation of Laboratory Animal Care International. Antibody pharmacokinetics and in vivo organ distribution was analyzed in 4–8-week-old homozygous female nude (RRID: 2175030, Foxn1(nu/nu), Jackson Laboratories) mice. For in vivo tumor and organ distribution as well as growth studies, the nude mice were inoculated in the left flank with $1x10^7$ cells. For tumor growth studies, tumor volume was measured with calipers 3 per week using the formula: volume = $0.5*length*width^2$.

Pharmacokinetics

Plasma clearance was measured after tail-vein injection of 10 to 20 mg/kg of fluorescent HMN-14 or XAb. Over the course of 24hrs, plasma samples were collected through retro-orbital sampling 10 µL of whole blood, then mixed with 15 µL of PBS- EDTA (10 mmol/L), and centrifuged at 3,000xg for 1 minute. 18µL of the resulting plasma was removed and frozen at 80°C until further analysis. The antibody concentration was then determined by scanning 15 µL of plasma in a 384-well black-walled Plate (Corning) on a NIR Odyssey CLx Scanner (LI-COR) and comparing the signal intensity to a calibration curve (at the same scan settings) of known antibody

concentration to signal intensity of the injected stock. The clearance for each antibody was fit to using a non-linear biexponential decay fit using PRISM (GraphPad).

Biodistribution

The biodistribution of the CEA antibodies was conducted as described previously[10, 38] with a bolus dose delivered for each antibody at either 10 mg/kg or 20 mg/kg. Briefly, 24 hours after tail-vein injection of fluorescent antibody, mice were euthanized, and organs were resected. Organs were then homogenized by mechanical disruption, incubated with 1:1 RIPA buffer (Thermo Fisher Scientific)/PBS solution supplemented with 5 mg/mL Collagenase Type IV (Thermo Fisher) for 1.5 hours, disrupted using a FB-120 Sonic Dismembrator, and finally incubated in 1:1 RIPA buffer/0.025% trypsin-EDTA solution for 1.5 hours. Afterwards, organ solutions and scanned on the Odyssey CLx scanner. The percent injected dose per gram of organ tissue (%ID/g) was then calculated by comparing signal intensity of the homogenized organs to a calibration curve of known fluorescent antibody concentration and normalized to organ weight and homogenate volume. PBS injected control mice were used to account for autofluorescence and were processed in the same manner as treated mice.

Fluorescence histology for imaging antibody tumor distribution

As described previously[38], the tumor distribution of fluorescent antibody was analyzed using fluorescence microscopy 24 hours postinjection. Briefly, 10 or 20 mg/kg fluorescent antibody was administered via tail-vein injection once the tumor volume was approximately 100 mm^3. To label functional vasculature in the tumor, Hoechst 33342 (Thermo Fisher Scientific) was administered 15 minutes before euthanasia via the tail vein at 15 mg/kg. Mice were then sacrificed,

tumors resected, flash-frozen in optimum cutting temperature (OCT) compound using isopentane chilled on dry ice and sectioned for histology on a cryostat (10-mm slices). Before imaging, tumor slices were stained for 30 minutes with anti-mouse CD31 (BioLegend, 102402) conjugated to Alexa Fluor 555 and briefly rinsed with PBS then imaged on an upright Olympus FV1200 confocal microscope equipped with a 20x objective and 405 nm, 543 nm, and 635 nm lasers. High-resolution tumor images were obtained by stitching smaller images with the Olympus software. Images were exported and analyzed using ImageJ image analysis software as described previously[10].

Tumor Efficacy Studies

Female homozygous Foxn1 nude mice (Jackson Laboratories, 002019) were injected in the left flank with $5x10^6$ LS174T cells. Mice were assigned into three treatment groups: PBS vehicle control (n=12), IMMU-130 (n=8), XAb (n = 8). Once tumors were approximately $100mm^3$ the ADC was delivered at 10mg/kg via IV every fourth day for a total of four doses in 12 days. Doses were selected to fully penetrate tumor tissue (see supplemental histology) and study the relative efficacy of each ADC under saturating conditions. Tumor sizes and mouse weight were recorded every 2 days until the study endpoint.

In vivo NIR fluorescence ratio measurements and fluorescence histology

Similar to previous studies[13, 146], the cellular uptake and degradation kinetics *in vivo* were conducted on mice bearing LS174T tumor xenografts with an average tumor volume of $100mm^3$. Antibodies were labeled with DDAO and IRDye, administered to mice at 10mg/kg doses, followed by euthanasia after 24hrs and tumor resection. Tumor were subject to a single cell digest using the

Miltenyi tumor dissociation kit and protocol before passing through a 40µm filter and analyzed by flow cytometry. PBS injected negative control tumor digests established negative gates for DDAO and IRDye fluorescence as well as autofluorescent controls for background subtraction. Isolating cells that received therapy (IRDye+), the DDAO signal was divided by IRDye signal to get the DDAO/IRDye ratio. This value was then normalized to in vitro cells that were labelled on ice to determine the percent intact.

LS174T Tumor Spheroids

Tumor spheroids were cultured using custom 384-well plates described previously[103, 128]. Briefly, 3,000 cells suspended in 25 µL of seeding media comprising 19.5 µL complete EMEM culture media, 5 µL of 1.2% (XAb/v) methocellulose (Dow Corning), and 0.5 µL Matrigel were added to alternate wells of the 384-well hanging drop plate. The edges of the 384-well plate were lined with sterile gauze soaked in sterile PBS. The 384-well plate was sandwiched in a 6-well clear well plate containing sterile PBS to minimize media evaporation from the hanging drops. Media changes were made every 2 days by removing 10 µL media from the drop and adding in 12 µL of fresh media (to adjust for evaporation). Spheroids were cultured for 5 days until they attained a diameter of 400–500 µm.

To study the pharmacodynamic impact of each ADC, the hanging drops were incubated in the 384- well plate with IMMU-130 or XAb at a final concentration of 20 nmol/L, by replacing 10 mL of the 25 mL of the spheroid media with 10 mL of 50 nmol/L (2.5x concentration) antibody. The drug concentration in the media was assumed to be constant over the course of the incubation (i.e., no depletion effects). After an 8-hour pulse, 10µL of droplet media was removed and replaced with fresh media (3x) then the spheroid was chased for 40 hours before harvesting. The spheroids

were individually extracted from the wells and washed two times with PBS before being fixed with 4% BD Cytofix, frozen in OCT, and stored at -80°C until further processing. Frozen OCT blocks were sectioned for histology on a cryostat (16µm slices), and sections were stained ex vivo for gamma H2AX, Hoechst 33342 (Thermo Fisher Scientific), FITC-anti-mouse or FITC-anti-human FC for 5 minutes before imaging on the Olympus FV1200 confocal microscope.

.

Chapter VI

ADC Mechanisms of Actions and Their Role in Anti-Tumor Efficacy

6.1 Abstract

ADCs are complex biologics that act through three main mechanisms to achieve their overall therapeutic effect: payload delivery, receptor blockade, and Fc-effector functions. Although the antibody backbone of the ADC is engineered to bind tumor-specific or tumor associated antigens only a fraction of the ADC enters the intended tissue. The remaining ADC is catabolized by target and non-target expressing healthy tissue, releasing the cytotoxic payload. The resultant healthy tissue toxicity caused by payload delivery has been deemed a critical factor in many clinical ADC failures. Given the payloads direct impact on therapeutic window, focus has been placed on optimizing payload selection, drug-antibody ratios, and linker combinations. This focus potentially overlooks contributions from antibody backbone through receptor blockade and Fc effector functions. In this work, we evaluate each contributing mechanisms of action (Fc effector function, receptor modulation, and payload delivery) in multiple preclinical models by modulating overall dose, naked antibody carrier dosing, and engineering Fc mutants with attenuated Fc effector function. Initial data in a genetically engineered mouse model supports that each mechanism aids in the overall efficacy. Future work in syngeneic mouse models may elucidate the relative contribution of each mechanism.

6.2 Background

ADCs couple the properties of small molecule therapeutics with macromolecular biologics delivering efficacy through multiple mechanisms of action (MoA)[147]. These include receptor-signaling modulation, cytotoxic payload delivery, and Fc-domain mediated functions that can stimulate an adaptive immune response[148, 149] (Figure 6-1). The ADC design parameters driving each of these mechanisms include tumor target and payload selection, antibody properties (isotype, affinity, alternative scaffolds), linker, and dosing (Drug-Antibody Ratio/DAR, schedule). These properties can dramatically shape the development of new agents, however, the relative contribution of each ADC component on efficacy is rarely studied, particularly in the clinic. While more studies are needed to fully elucidate the importance of each mechanism, retroactive studies of the solid tumor ADCs can provide insight to driving features.

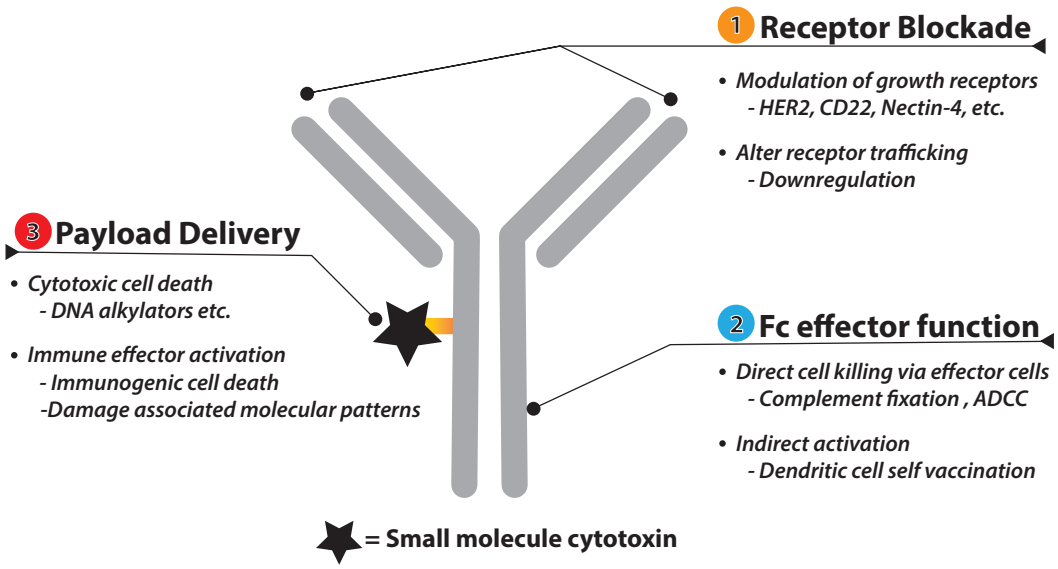

Figure 6-1. Description of the three main mechanisms of action for ADCs

Ado-trastuzumab emtansine (Kadcyla or T-DM1), the first FDA approved ADC for solid tumors, provides an illustrative example of the potential for different MoA to evoke a therapeutic response. This ADC is formed by the conjugation of DM1 (a potent tubulin inhibitor) to

Trastuzumab, an antibody that blocks HER2 signaling within target cells. Trastuzumab has been FDA approved as a single agent therapy and elicits a significant response in many high HER2 expressing cancers[150] suggesting that receptor blockade or Fc mediated functions may be the primary mechanisms for T-DM1. However, patients that have relapsed after treatment with Trastuzumab still demonstrate sensitivity to T-DM1. If HER2 receptor blockade or Fc effector function was the main driver of efficacy, it would be expected that T-DM1 would also be ineffective in cases where trastuzumab lacked efficacy. This data suggests that the payload is critical for clinical efficacy, but many ADCs against other targets have failed in the clinic; therefore, the primary MoA of the ADC is unknown. It is likely that direct payload killing is important, but immune cell activation due to payload delivery[151] may provide the response in patients that are insensitive to trastuzumab alone. For antibody-based therapies Fc-mediated functions have been shown to impart efficacy[152-154]; however, both T-DM1 and trastuzumab have functional Fc regions making it unlikely that Fc-mediated effects account for the efficacy difference between these therapies in trastuzumab insensitive patients. In summary, all three MoA may contribute to efficacy. However, the relative importance of each MoA in a particular treatment is unknown and therefore the design of ADCs is not optimized based on the primary driver of clinical response. For example, *is payload delivery to all tumor cells important (for direct cell killing from the payload) or is death of only a few tumor cells needed to prime dendritic cells and a higher antibody dose (with only a few payload molecules) more effective?* This work will isolate these mechanisms to quantify the relative contribution and potential synergies between these MoA.

Precise quantitative techniques using immunocompetent animal models provide an innovative method to isolate MoA and determine the relative importance of each MoA for a given

target. If payload delivery is the primary means of efficacy, antigen expression and payload potency can be used to determine an optimal DAR that will maximize payload-driven tumor cytotoxicity by matching cellular delivery to payload potency[155]. In a response where Fc-effector functions are a requisite for clinical response, then selecting high expressing targets/patients and/or pairing with immunomodulatory drugs[156] may be critical for clinical success[118]. In many cases it is likely that more than one MoA will contribute to the overall efficacy. Recently, we demonstrated a method for improving multiple MoA by increasing the antibody dose against highly expressed targets (at a constant payload dose) to improve payload delivery and increase Fc-domain density on the target cell surface[13], potentially increasing Fc-mediated functions. Knowledge of the efficacy imparted by each MoA will improve ADC design to combat potential weaknesses and improve upon drivers of efficacy leading to greater clinical success. In this work, we isolate individual mechanisms through protein engineer, payload conjugation, and dose modification as displayed in Figure 6-2.

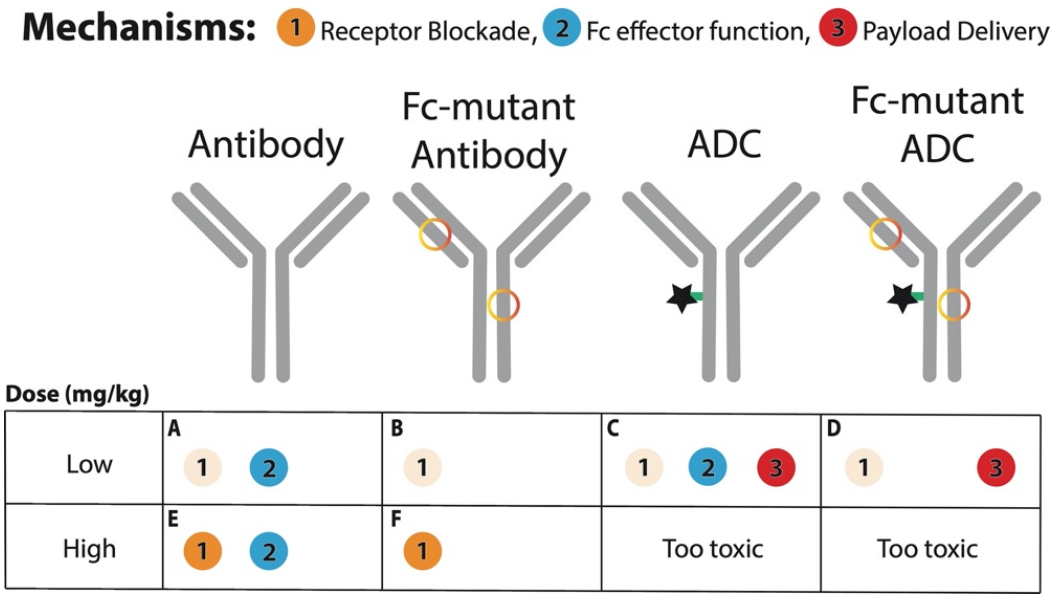

Figure 6-2. Protein modifications to isolate individual MoA

Depending on the antibody scaffold and dose, specific mechanisms can be isolated and studied. Faint orange represents the attenuation but not complete removal of receptor blockade that occurs for lower doses. Engineered Fc regions of antibody and ADC are represented by orange circle regions.

6.3 Results

In previous work, we demonstrated that ADC efficacy is not directly linked to ADC potency in vitro. Highly potent ADCs restrict the maximum tolerated dose, exposing perivascular tumor cells to the drug. Instead, maximum efficacy corresponds to the agent capable of delivering a lethal dose to the largest fraction of cells[13]. Next we tested the relative importance of each ADC MoA in a genetically engineered mouse model. This model provides one of the most representative mouse models for human cancer given the spontaneous tumor growth that develops from mutations that collect over time in a single cell. Although these models provide spontaneous, neoplastic growth similar to human disease progression, the lengthy tumor growth period and the innate variability of the model reduces the resolving power to analyze relative efficacy differences between therapies. Likewise, these models may possess fewer neoantigens, which could be important for immune activation[157]. Despite these limitations, this model demonstrated the importance of leveraging multiple mechanisms of action (Figure 6-3).

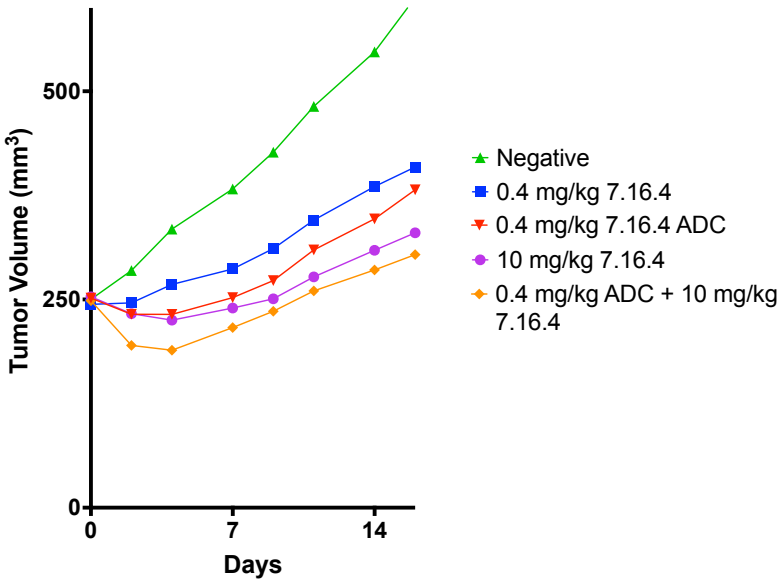

Figure 6-3. 4T1 Tumor Efficacy curves

The impacts of different mechanisms of action on measured efficacy. Low doses would limit receptor modulation, Fc-effector function, and payload delivery. Unconjugated 7.16.4 antibody only acts through receptor modulation and Fc-effector function. 7.16.4 ADC and a carrier dose of 7.16.4 acts through all three mechanisms.

An anti-HER2 monoclonal antibody (7.16.4) shows some efficacy, as expected, but adding a payload improves response (red versus blue). A higher dose of antibody can reach more cells for improved receptor blockade (purple). The most effective treatment combined 10 mg/kg of antibody with 0.4 mg/kg of ADC (orange). Despite the 25-fold 'dilution' of the ADC, the combination of a high antibody dose with the ADC resulted in the greatest efficacy. This data runs counter to conventional approaches that seek to maximize the ADC potency and avoid 'contamination' of ADC during manufacturing with unconjugated antibody (e.g. Mylotarg). Due to the variability in spontaneous tumor growth, statistical significance was not achieved long term. A grouped ANOVA comparison between therapies highlighted some trends in Figure 6-4 between therapies utilizing varied mechanisms. While not conclusive, this data supports the role of multiple MoA for maximum response.

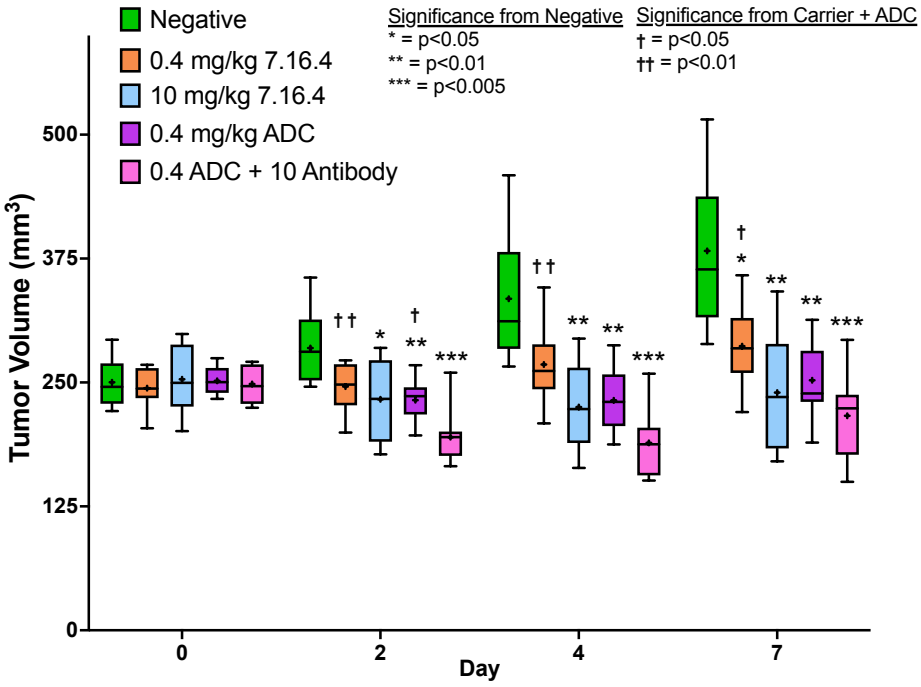

Figure 6-4. ANOVA test comparing significance between untreated and treated groups

Trials with n=10 mice were used for each therapy. Although variability rendered comparisons between most therapies to be non-significant, varying levels of statistical difference were calculated for the therapies compared to untreated 'negative' mice.

The single tumor growth curves provided in Figure 6-5 display the variability of this mouse model. Given the emphasis of this study in highlighting differences between MoA and not directly correlating the efficacy of these mechanisms to human clinical data, a less variable syngeneic mouse model was chosen for future experiments to increase statistical power.

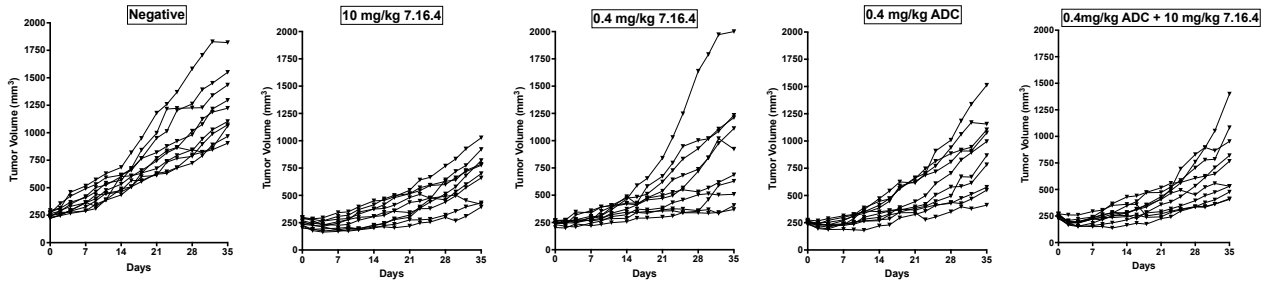

Figure 6-5. Individual tumor growth curves

Trials with n=10 mice were used for each therapy. There is a wide range of variability in the growth in negative mice as well as response to treatment for the various therapies likely due to the required random genetic mutations that spawn these spontaneous tumors potentially resulting in different inherent growth rates.

A Balb/c mouse model injected with clinically relevant 4T1 advanced metastatic breast cancer cell line was chosen based on the documented use of this cell line *in vivo* for efficacy studies as well as immune environment testing[158-160]. A cohort of 10 Balb/c mice were injected with the 4T1 cell line and the tumors were analyzed for EphA2, EpCAM, and CD45 receptors. EpCAM had the highest expression at ~400,000 receptors per cell while EphA2 expression was more moderate at ~75,000 receptors per cell. In the tumor, ~30-40% of cells were immune cells (CD45+) which provides adequate space to measure the increase or decrease in tumor infiltrating leukocytes (TILs). Previously FDA approved ADCs target high expression targets and so intial studies of ADC MoA were conducted with an anti-EpCAM ADC.

Initial cellular potency was characterized with a PrestoBlue protocol after a six-day incubation. Potency was demonstrated for EpCAM-PBD ADC and for coadministration of EpCAM antibody and EpCAM-PBD down to a dilution of 1:20 as shown in Figure 6-6.

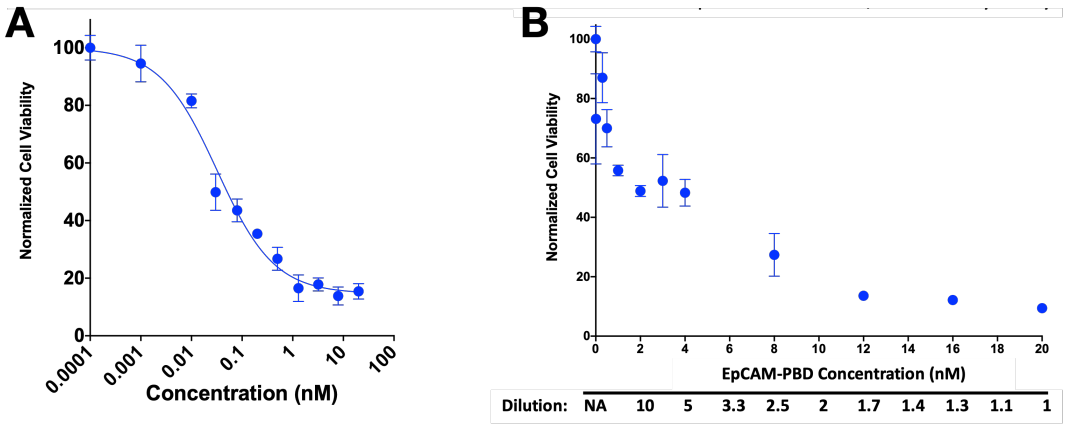

Figure 6-6. EpCAM-PBD Potency and coincubation potency in 4T1 cells

A) IC50 of EpCAM-PBD demonstrated double-digit pM potency. B) maintaining a constant antibody incubation concentration but modify how much of this constant total concentration was made up of antibody vs ADC provided a look at therapeutic thresholds for potential coadministration in vivo.

As expected, the potent PBD payload enacted significant cell death even with incubations at picomolar concentrations. Intriguingly, the ADC demonstrated potency in this cell line even under extreme dilution conditions. The EpCAM antibody and EpCAM ADC share the same binding regions and presumably binding kinetics meaning there is no selective pressure for one protein to outcompete the other for binding. In this experiment both ADC and antibody will bind to the cells surface in a ratio identical to the incubation ratio. This means at the 20nM ADC incubation only ADC binds while at a 2nM incubation 10x more naked antibodies will bind the cells surface than ADC. While the total antibody concentration is maintained, the reduction in antibody carrying payload reduces cell death, increasing cell viability as the ADC:antibody ratio decreases. Understanding the changes in in vitro potency with a dilution of naked antibody

provides more information on dynamics of cell killing in vivo. However, there are additional ADC parameters related to efficacy such as tumor uptake which was explored in Figure 6-7.

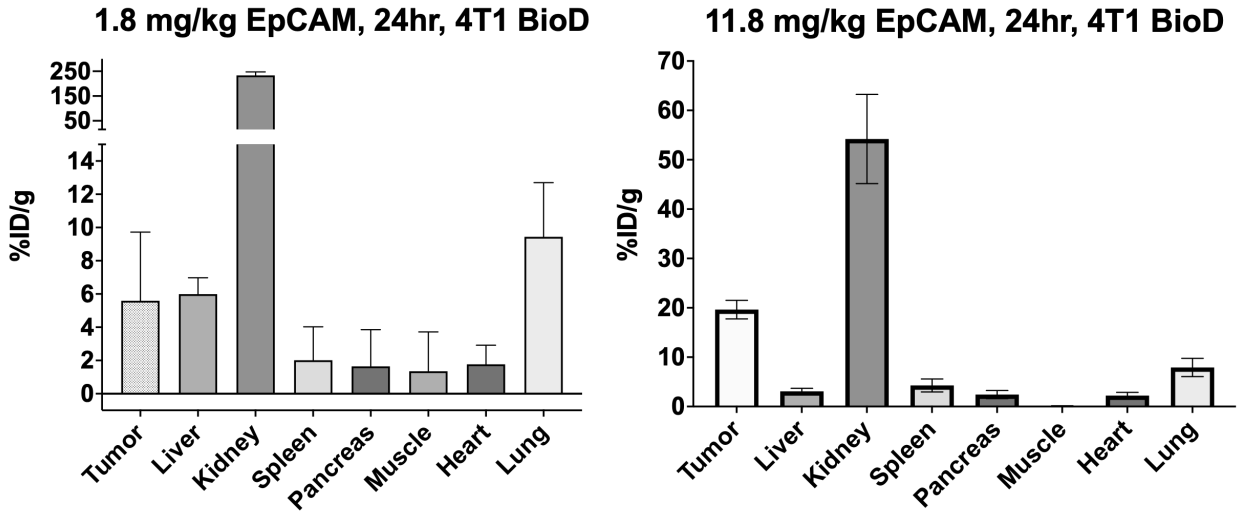

Figure 6-7. EpCAM organ level distribution

A) Lower doses of EpCAM experienced rapid clearance in the blood and uptake in the kidney, resulting in poor tumor uptake B) Higher doses resulted in saturation of on-target clearance in the kidney and a higher tumor uptake.

Surprisingly, the fluorescent EpCAM antibody demonstrated significant targeting to the kidney for both the low and high dose albeit significantly reduced for the higher dose. At the low dose of EpCAM kidney targeting increased clearance of the antibody and thus decreased tumor exposure. A higher dose was able to saturate the kidney and provided a longer residence time in the blood resulting in greater tumor targeting. To confirm tumor distribution as well as investigate the large renal uptake confocal images of tissue histology slides were gather and analyzed.

In Figure 6-8, the 11.8 mg/kg dose of EpCAM is shown to be near saturation. Individual regions of the tumor were examined in more detail depicting the overall heterogeneity of the 4T1 tumor model. The highly vascularized tumor resulted in decent penetration throughout. At this

dose we were also able to critically analyze the regions of EpCAM uptake in the Kidney to determine whether uptake was likely nonspecific or target mediated.

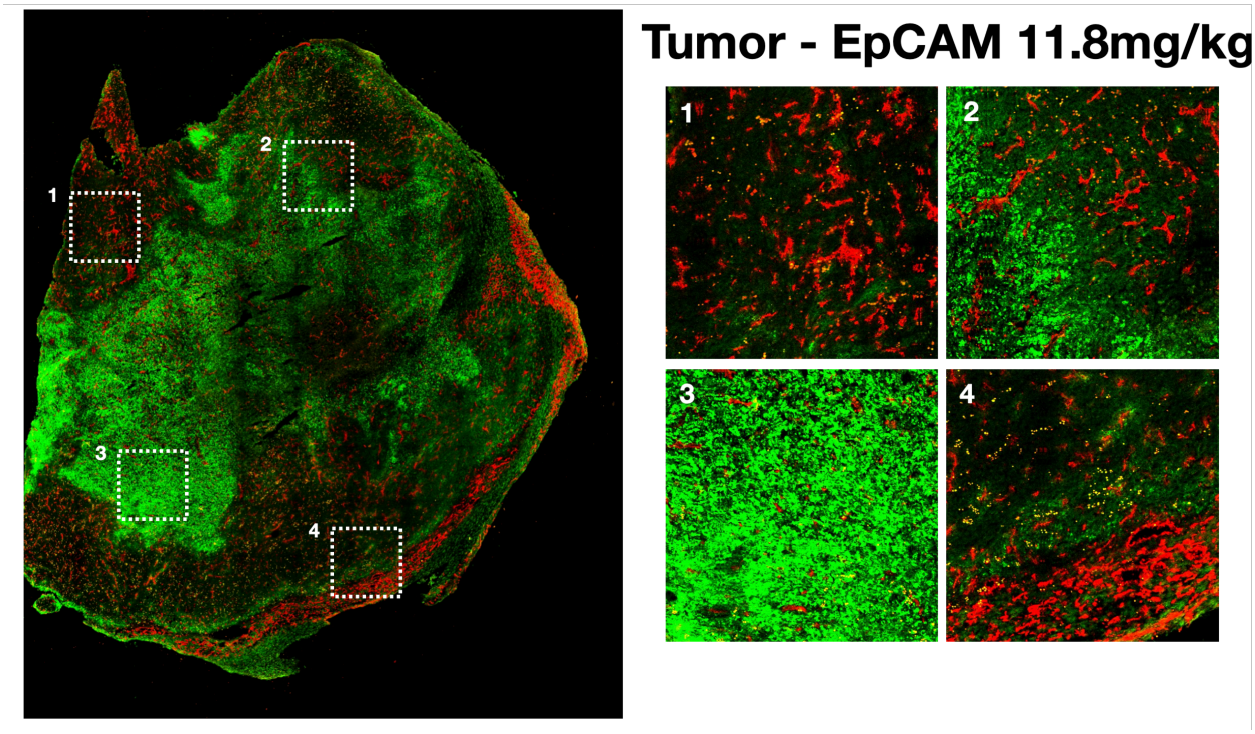

Figure 6-8. EpCAM Tumor histology slides

At the higher doses (11.8mg/kg) tumor delivery is almost saturated. Highly heterogenous tumor microenvironment expression of EpCAM is shown by panels 1-4.

In Figure 6-9 the resected kidney of a 4T1 tumor bearing mouse was sectioned to display the distribution characteristics of the EpCAM antibody in the kidney. Limited penetration but significant uptake was seen in the renal cortex, collecting ducts, and medulla. The steep fluorescent gradients suggest a bulky intact antibody with limited penetration due to target binding and retention as opposed to a degraded antibody that released dye non-specifically.

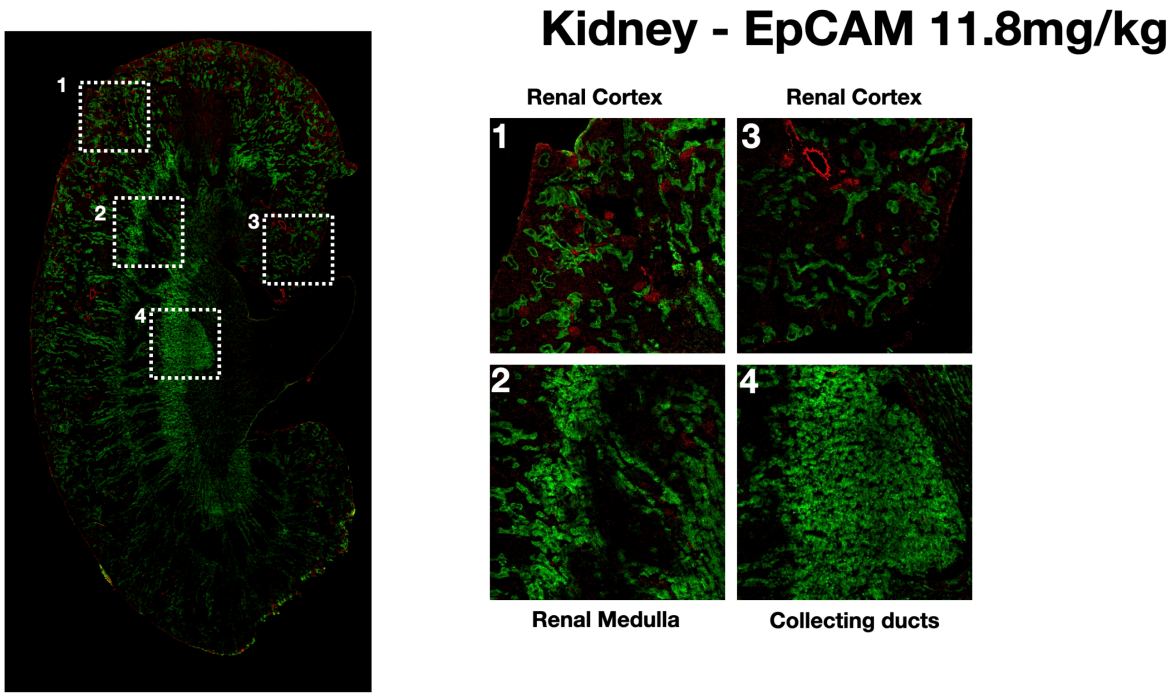

Figure 6-9. EpCAM Kidney histology slides

Mouse kidney tissue expresses mouse EpCAM resulting in significant uptake in this organ, even though the antibody molecular weight is much greater than the filtration limit of ~60kDa for renal clearance. This uptake resulted in significant target mediated drug disposition and clearance at low EpCAM doses.

Importantly, this analysis is supported by the quantitative biodistribution data (Figure 6-7) demonstrating that an increase in dose reduced overall uptake, highlighting a saturable mechanism of clearance via the kidneys. Given the specific clearance, tolerable doses for efficacy studies would likely be low and at any dose mouse weights would need to be recorded. We began testing the EpCAM-PBD ADC to determine if there would be a dynamic range of efficacy that could be used to determine the driving mechanism behind the overall efficacy shown in Figure 6-10.

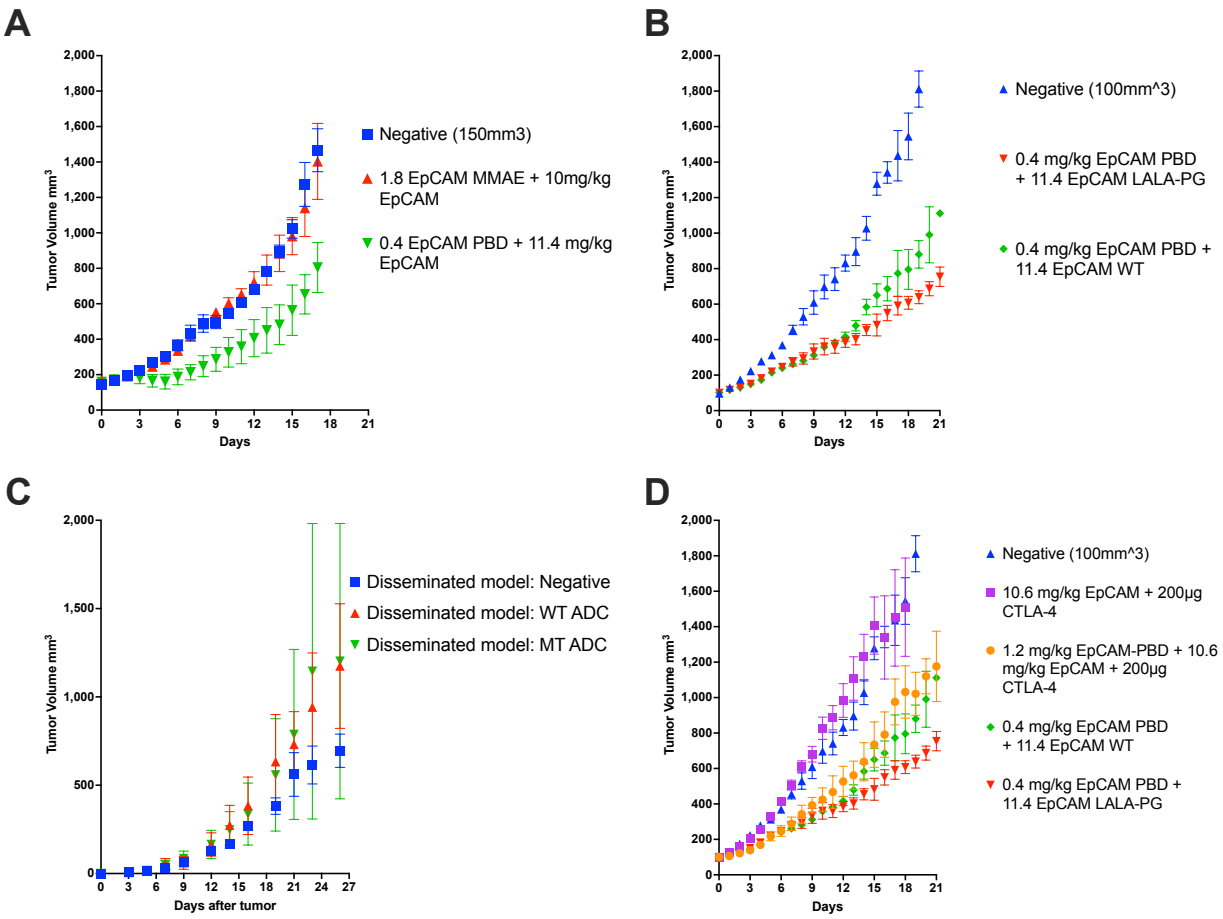

Figure 6-10. Tumor Growth Curves EpCAM ADC in 4T1 Tumor Model

Syngeneic tumor lines offer an intact immune system but require the use of host species tumor lines. Multiple iterations of various treatments were attempted to identify differences between Direct payload delivery and Fc effector function, however, treatments only succeeded in modest growth inhibition even up to 1.2 mg/kg of a PBD ADC.

Initial growth curves portrayed limited response from an EpCAM-MMAE ADC while the PBD variant delivered increased efficacy but not tumor regression (Figure 6-10A). The PBD variant had potential to offer a dynamic range for study (between greatest efficacy and no efficacy) and was thus pursued with other treatment regimens. Figure 6-10B displays a direct comparison between Fc-effector function in this system. The same ADC dose is delivered; however, the carrier dose was either a wildtype (WT) antibody with potential for Fc-effector function or a mutant (MT) antibody that lacked this capability. The resulting tumor growth curves did not differ significantly

out to two weeks. As mice were sacrificed towards the endpoint, the curves began to separate but are unexpected to be attributed to differences in treatment regimens. The same dosing was used to treat a disseminated tumor model but demonstrated no statistical difference in efficacy between therapies and the negative control (Figure 6-10C). In a final attempt to increase the dynamic range of efficacy between the negative control and the most efficacious treatment, a codosing strategy with an immune modulating agent and a higher dose of ADC was employed (Figure 6-10D). Even with a threefold increase in ADC and the additional immune modulating, tumor response was minimal. Given the difficulties experienced with this receptor system (TMDD, limited uptake, lack of immune response), a separate 4T1 tumor neoantigen, EphA2, was evaluated.

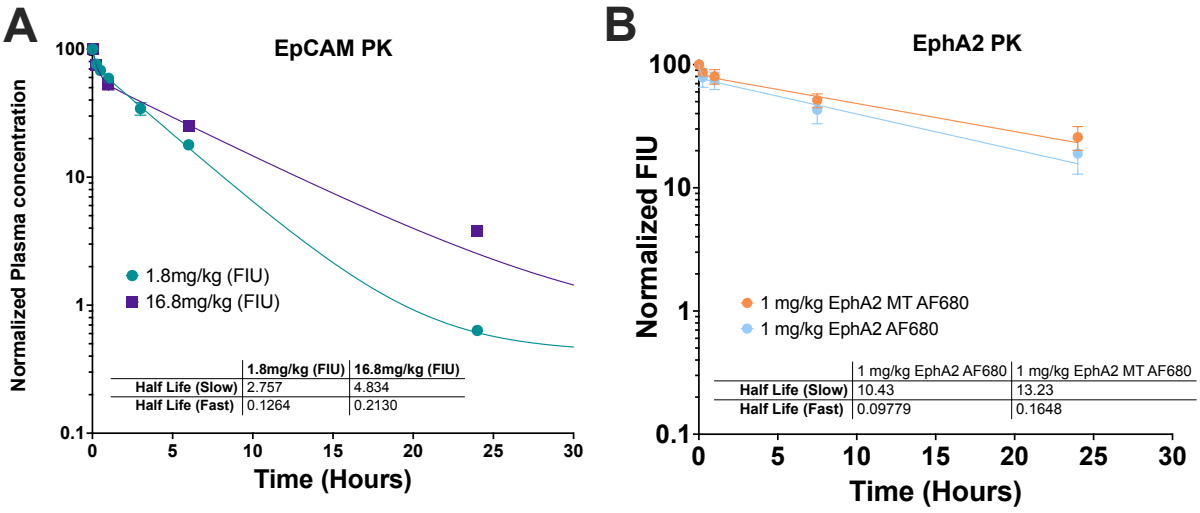

Figure 6-11. Antibody pharmacokinetic profiles

While EpCAM blood clearance was rapid due to kidney uptake causing TMDD (A), EphA2 demonstrated a more desirable PK profile even at low doses (B).

The PK profiles were compared between the unsuccessful EpCAM antibody and the EphA2 antibody exhibiting increased overall exposure for the EphA2 antibody (Figure 6-11). While the exposure of the EphA2 antibody was encouraging, lower tumor receptor expression decreased the tumor uptake of EphA2 as demonstrated in the biodistribution data (Figure 6-12).

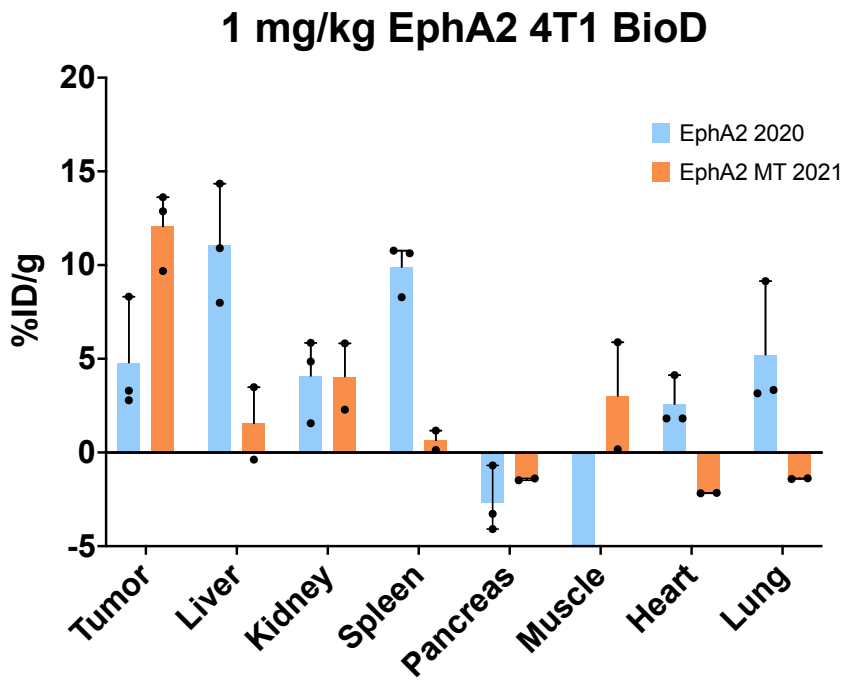

Figure 6-12. EphA2 antibody distribution profile

The lower tumor uptake of EphA2 antibody was comparable to the EpCAM antibody uptake for low doses (1mg/kg and 1.8mg/kg) which can be accounted for based on the measured differences in receptor expression.

6.4 Discussion

The complex design of ADCs leads to sometimes unexpected results, especially when translating from in vitro to in vivo to the clinic. Being able to connect specific mechanisms of action that lead to efficacy at each stage of this translation and potentially modify the design to incorporate the main drivers of efficacy has the potential to not only increase the fraction of viable candidates but also to improve their therapeutic response. In this work, we outline a novel method to investigate and isolate individual mechanisms of ADC action. While the method is simple in concept, the practical adaption is challenging.

Genetically engineered mouse models (GEMM) are some of the most advanced preclinical models to date. Spontaneous tumor formation from individual mutations has been shown to closely follow clinical tumor progression and may produce more translatable results. The rat-HER2 antibody (7.16.4) was produced, purified, and characterized and then a fraction of this stock was modified to attenuate Fc effector function. To isolate payload delivery, naked antibody was administered vs ADC and to turn on/off receptor modulation the total antibody dose delivered was modified. Figure 6-3 depicts the trends from these administrations although the dynamic range and mouse to mouse variability did not allow for a statistically significant comparison between treatment groups. Overall trends demonstrated that all three mechanisms aid in efficacy denoted by modest efficacy with each treatment and the greatest efficacy in the treatment regimen containing all three mechanisms. However, in these model trends were all that could be discerned (Figure 6-4). To determine relative contributions more effectively, we utilized a more consistent, syngeneic model.

Syngeneic models offer an intact immune system for a preclinical model but often lower variance in tumor growth delay and growth rate than the GEMM. The 4T1 syngeneic mouse tumor cell line has moderate expression of EpCAM and EphA2 as well as hosting a significant fraction of immune cells in the tumor microenvironment (~30% immune cells). Initial work with the 4T1 EpCAM model through in vitro toxicity assays demonstrated the potency of an EpCAM-PBD ADC. This potency was tested further through constant total antibody incubations with an increasing ratio of naked EpCAM antibody to EpCAM-PBD. The EpCAM-PBD ADC maintained 50% cell killing down to dilutions as extreme as 20-fold suggesting a therapeutic concentration could be maintained at high carrier doses in vivo (Figure 6-6).

Moving from in vitro to in vivo work we explored two administration doses (1.8mg/kg and 11.8mg/kg). Target mediated drug disposition (TMDD) of the kidney lead to rapid plasma clearance at low EpCAM doses (Figure 6-11A). Based on biodistributions (Figure 6-7), the kidney was the mediator of TMDD. While we have demonstrated kidney uptake up to 300%ID/g for peptides (e.g. helix bundles[102]), large kidney uptake of an EpCAM antibody with a molecular weight above the approximate renal filtration cutoff (<60kDa) was not expected. We confirmed the TMDD by administering a higher dose of antibody which saturated this clearance mechanism leading to the traditional antibody biexponential decay (Figure 6-11A). At the higher administered dose, kidney uptake reduced suggesting a saturable EpCAM target in the renal tissue (Figure 6-7). Additional data demonstrating the target specific binding of EpCAM in the kidney was conducted through histology imaging of renal tissue (Figure 6-9) portraying limited penetration of intact antibody. The accumulation of biologic in the kidney may partially explain the lackluster efficacy of the EpCAM ADC.

Biodistribution data showed moderate tumor uptake at low doses (with greater uptake at higher doses, Figure 6-7) and tumor histology depicted heterogenous expression with significant tumor penetration (Figure 6-8). Both of these data likely contribute to the limited efficacy of the EpCAM-PBD in the syngeneic mouse model (Figure 6-10). Moderate tumor inhibition but never tumor regression was documented with isolated ADC MoA and with all three MoA involved (Figure 6-10 A, B, C). Even the coadministration of an immune modulating agent did not improve efficacy leaving a narrow dynamic range to study the individual MoA impact on efficacy. Given the limited efficacy for this model system, we chose to switch antigen targets from EpCAM to EphA2 where previous reports of superior tumor efficacy have been documented[119].

The PK profile of EphA2 was improved compared to EpCAM which experienced TMDD (Figure 6-11). The increased blood residence time of EphA2 did not result in improved tumor uptake of EphA2 at 24 hours (Figure 6-12). Instead, due to lower receptor expression uptake was limited to 5-15% ID/g for the wildtype and mutated Fc. The lower uptake is concerning, but literature precedent suggests this uptake to be therapeutic for the 4T1 syngeneic model.

6.5 Future Work

The next steps of this project involve replicating the literature growth curves for an EphA2 ADC in a syngeneic model. The EphA2 receptor target should provide increased efficacy and dynamic range of tumor growth to compare the driving forces of ADC efficacy based on literature precedent. ADCs are complex biologics targeting a dynamic tumor environment with multifaceted features. This chapter began the work to develop a general protocol for isolating the key driving mechanisms for ADC efficacy in specific target systems. The method development has been as complex as the drug and tumor environment. Moving from a GEMM to a syngeneic mouse model reduced variability in tumor growth curves but a limited response from EpCAM ADCs required a shift to a well characterized delivery system. Achieving a general method for determining the key design features for efficacy may elucidate ADC design strategies for improved efficacy and clinical success.

6.6 Experimental Methods

Cell Culture and Animals

Cell lines were purchased from ATCC. Cells were cultured two to three times per week up to passage number of 25 and grown in RPMI/DMEM supplemented with 10% (v/v) FBS, 50 U/mL

penicillin, and 50 mg/mL streptomycin at 37°C with 5% CO2. Annual mycoplasma testing was conducted using the Mycoalert Testing Kit (Thermo Fisher Scientific, NC9719283). All animal studies were approved and conducted in compliance with the Institutional Animal Care and Use Committee of the University of Michigan (Ann Arbor, MI) and Association for Assessment and Accreditation of Laboratory Animal Care International. Antibody pharmacokinetics and in vivo organ distribution was analyzed in Genetically engineered mice and 4–8-week-old homozygous female nude (RRID: 2175030, Foxn1(nu/nu), Jackson Laboratories) mice. For in vivo tumor and organ distribution as well as growth studies, the nude mice were inoculated in the left flank with $1x10^6$ cells while GEMM were allowed to grow spontaneously over the course of 3-6 months. For tumor growth studies, tumor volume was measured with calipers 3 per week using the formula: volume = $0.5*length*width^2$.

Pharmacokinetics

Plasma clearance was measured after tail-vein injection of 10 to 20 mg/kg of fluorescent antibodies. Over the course of 24hrs, plasma samples were collected through retro-orbital sampling 10 µL of whole blood, then mixed with 15 µL of PBS- EDTA (10 mmol/L), and centrifuged at 3,000xg for 1 minute. 18µL of the resulting plasma was removed and frozen at 80°C until further analysis. The antibody concentration was then determined by scanning 15 µL of plasma in a 384-well black-walled Plate (Corning) on a NIR Odyssey CLx Scanner (LI-COR) and comparing the signal intensity to a calibration curve (at the same scan settings) of known antibody concentration to signal intensity of the injected stock. The clearance for each antibody was fit to using a non-linear biexponential decay fit using PRISM (GraphPad).

Biodistribution

The biodistribution of the antibodies was conducted as described previously[10, 38] with a bolus dose delivered for each antibody. Briefly, 24 hours after tail-vein injection of fluorescent antibody, mice were euthanized, and organs were resected. Organs were then homogenized by mechanical disruption, incubated with 1:1 RIPA buffer (Thermo Fisher Scientific)/PBS solution supplemented with 5 mg/mL Collagenase Type IV (Thermo Fisher) for 1.5 hours, disrupted using a FB-120 Sonic Dismembrator, and finally incubated in 1:1 RIPA buffer/0.025% trypsin-EDTA solution for 1.5 hours. Afterwards, organ solutions and scanned on the Odyssey CLx scanner. The percent injected dose per gram of organ tissue (%ID/g) was then calculated by comparing signal intensity of the homogenized organs to a calibration curve of known fluorescent antibody concentration and normalized to organ weight and homogenate volume. PBS injected control mice were used to account for autofluorescence and were processed in the same manner as treated mice.

Fluorescence histology for imaging antibody tumor distribution

As described previously[38], the tumor distribution of fluorescent antibody was analyzed using fluorescence microscopy 24 hours post injection. Briefly, fluorescent antibody was administered via tail-vein injection once the tumor volume was approximately 100-250 mm^3. To label functional vasculature in the tumor, Hoechst 33342 (Thermo Fisher Scientific) was administered 15 minutes before euthanasia via the tail vein at 15 mg/kg. Mice were then sacrificed, tumors resected, flash-frozen in optimum cutting temperature (OCT) compound using isopentane chilled on dry ice and sectioned for histology on a cryostat (10-mm slices). Before imaging, tumor slices were stained for 30 minutes with anti-mouse CD31 (BioLegend, 102402) conjugated to Alexa Fluor 555 and briefly rinsed with PBS then imaged on an upright Olympus FV1200 confocal

microscope equipped with a 20x objective and 405 nm, 543 nm, and 635 nm lasers. High-resolution tumor images were obtained by stitching smaller images with the Olympus software. Images were exported and analyzed using ImageJ image analysis software as described previously[10].

Tumor Efficacy Studies

Female homozygous Foxn1 nude mice (Jackson Laboratories, 002019) were injected in the left flank with $1x10^6$ 4T1 cells. Mice were assigned into three treatment groups. Once tumors were approximately $100mm^3$ for nude mice and 250 for GEMM, the ADC/antibody was delivered at via IV. Tumor sizes and mouse weight were recorded every 2 days until the study endpoint.

In vivo NIR fluorescence ratio measurements and fluorescence histology

Similar to previous studies[13, 146], the cellular uptake and degradation kinetics *in vivo* were conducted on tumor bearing mice with an average tumor volume of $100mm^3$. Antibodies were labeled with AF647 or AF680, administered to mice, followed by euthanasia after 24hrs and tumor resection. Tumor were subject to a single cell digest using the Miltenyi tumor dissociation kit and protocol before passing through a 40µm filter and analyzed by flow cytometry. PBS injected negative control tumor digests were conducted as auto fluorescent controls for background subtraction

Chapter VII

Concluding Remarks and Future Directions

7.1 Summary of Work

Throughout this dissertation, a hybrid approach of computational and experimental approaches was developed and applied to quantitatively track the distribution of protein drug conjugates at multiple length scales (organ, tissue, and cellular) with the goal of understanding how to design a successful protein drug conjugate. In Chapter 2 of this dissertation, I improved upon a previously developed dual label near infrared fluorophore method by utilizing a separate set of dyes (non-residualizing probe: BoDIPY-FL and residualizing probe: AF647) with greater signal to noise ratio providing accurate measurements on uptake and degradation for low expression tumor neoantigens. After the dual labeled antibody binds a receptor, becomes internalized and degraded, the non-residualizing probe leaks out of the cell providing a measure of intact protein while the residualizing probe remains intracellular to measure total uptake. The more sensitive fluorophores were validated against the previous dual label NIR fluorophores for antibodies and antibody drug conjugates. This method holds promise for measuring the net binding kinetics and internalization rates that dictate tumor penetration and the fraction of tumor cells targeted by therapy, specifically for low expression targets.

In Chapter 3, an intriguing discrepancy between in vitro and in vivo efficacies led to an in-depth quantitative analysis of the driving factors in solid tumor efficacy for protein drug

conjugates. A panel of single domain antibodies with significantly differing pharmacokinetics and internalization rates were systematically analyzed for their in vitro and in vivo delivery through biodistribution data, tumor histology images, spheroid experiments, in vivo single-cell measurements, and computational results. I predicted and experimentally verified that the overall tumor uptake of slowly cleared protein drug conjugates would be comparable with a Krogh cylinder model and biodistribution, highlighting that a separate factor must account for the discrepancy in potencies. I then investigated the intratumoral distribution computationally demonstrating that the more efficacious agent would penetrate tumor tissue, targeting a greater number of cells. After I validated these results through tumor histology and Euclidean distance mapping of tumor histology slides, I determined the therapeutic concentration of payload required to cause cell death via a tandem fluorescent and cytotoxicity assay. I used this data to verify that although the greater penetration reduced the amount of payload delivered per cell, that the lower amount of payload would still be therapeutic. Overall, I was able to demonstrate that a smaller size and slower internalization rate enabled higher tissue penetration and more cell killing. The results provided evidence that reaching the maximum number of cells with a lethal payload dose correlates more strongly with in vivo efficacy than total tumor uptake or in vitro potency alone for these protein-drug conjugates. Supporting the analysis of distribution characteristics in addition to toxicity measures for solid tumor ADC candidates.

In Chapter 4, I evaluated the clinical landscape of solid tumor ADCs and highlighted the similar design components for these ADCs. Current FDA-approved solid tumor ADCs target high expression antigens with large doses of IgG1-based therapeutics. These design features are supportive of tumor exposure and potentially saturation. The work demonstrated the need to design

ADCs based on tumor microenvironment characteristics. For some ADCs perivascular distribution can be improved by selecting protein scaffolds with a slower internalization rate (Chapter 3) but recently approved ADCs administer doses that can come close to tumor saturation. Optimal ADC design under these conditions were investigated in Chapter 5.

A slow internalization rate can improve penetration but as the internalization rate decreases so does direct payload delivery. While currently approved solid tumor ADCs consistently target high expression targets (>10^5 receptors per cell), many tumor neoantigens are considered to have too low expression or slow internalization. In chapter 3, I found that a biparatopic single-domain antibody internalized more quickly than a monovalent single domain antibody or bivalent antibody. Utilizing a previously discovered cross-linking antibody against CEA, I demonstrated that increasing the internalization rate with a saturating dose is more efficacious. This has implications for novel ADCs designed against low expression targets that have been discarded due to perceived limitations in cellular delivery of payload above a therapeutic threshold.

In Chapter 6, the main mechanism of action for ADCs were isolated to examine the relative importance of each mechanism. A collaboration with the Tessier lab, produced antibodies with point mutations that limit the Fc effector function, naked antibody removed payload delivery, and dose was used to modulate receptor modulation. An initial efficacy study using a GEMM resulted in trends favoring the combination of all three mechanisms over individual mechanisms, however, the difference in efficacy between individual mechanisms was not statistically significant. Syngeneic mice provide a model system with an intact immune system with less variability although with less clinical relevance. Initial studies in this model explore EpCAM targeted ADCs

with limited efficacy due to TMDD and poor expression. Current studies are exploring an EphA2 ADC which has demonstrated efficacy previously. The protein engineering approaches mentioned above are currently being used to elucidate the driving mechanisms behind ADC activity in vivo.

This dissertation improves upon previous techniques to study antibody distribution, degradation, and delivery as well as the key parameters for efficacy through quantitative computational and experimental techniques. These methods were applied to specific tumor systems to identify fit for purpose protein drug conjugates. In chapter 2 and 3, rapid internalization rate was identified as a key detriment to penetration concentrating payload in perivascular cells. Chapter 4 simplified the successful design of solid tumor ADCs to three broad design features: IgG1 isotype, large doses, and high expression targets. In Chapter 5 the concept of slower internalization to increase penetration was analyzed for ADC design following the most recent approvals. Mainly moderate potency ADCs that are tolerated at saturating doses demonstrate improved efficacy with a crosslinking antibody that drives internalization. Lastly, chapter 6 began to identify protein engineering approaches to selectively turn on or off individual mechanisms of action for ADC efficacy. While this work is ongoing, being able to determine the drivers of efficacy early in development may provide insight into areas of ADC design that are crucial for specific tumor indications.

7.2 Future Work and Directions

The research presented in this dissertation addressed current challenges but also developed methods capable of guiding the design of future ADCs. In this section I succinctly provide key

areas where ADC/payload distribution on the tumor and cellular level may directly impact anti-tumor efficacy.

Increased acceptance of fluorescent measurement of tumor penetration, saturation, and degradation of ADC therapies in the industry

In Chapter 2, I developed a novel dual label near infrared dye set to track total uptake and degradation of antibody in a single mouse. Ideally, this work could be used initially in vitro to highlight potential ADC design flaws before moving to in vivo systems. For example, if measurements of single cell uptake demonstrate DAR corrected payload uptake below a therapeutic threshold, then the antibody could be designed to incorporate more payload, a higher potency payload, or a faster internalizing protein scaffold. On the other side, if an antibody is shown to deliver more than enough payload through total uptake, a lower DAR, less potent payload, or slower internalizing agent may make more sense to move into preclinical studies. At this stage, the method will provide detailed distribution characteristics in terms of total tumor uptake, tumor penetration, and with flow cytometry payload uptake per cell. Further modifications could be made at this point to support internalization or penetration depending on the data presented. As tumor penetration and saturation become more routine in industry testing, I believe a larger fraction of clinical ADC trials will be successful.

Designing ADCs past simple drug carriers to the tumor microenvironment

In Chapters 4 and 6, I discuss the landscape of clinically successful solid tumor ADCs and their respective mechanisms of action. While ADCs have been in development for many decades, only recently are ADCs being recognized for the complexity of their anti-tumor efficacy. While

current preliminary methods of industrial development place an emphasis on potency in vitro and high binding affinity, these measures may be outdated for next-generation ADCs. The potency of an ADC in vitro overlooks the distribution profile and often in simple toxicity assays any immune effector function driven by the Fc region. In vivo these mechanisms all come together to form the overall response, however, in vitro tests often miss this combinatorial or synergistic effect. In chapter 3, we highlighted a protein drug conjugate that likely would not have moved on from initial testing. It was 10x less potent in vitro, but through computational and experimental methods we determined that the distribution profile in vivo was superior to the more potent agents resulting in greater efficacy. Identifying the key actions of an ADC in vivo and developing in vitro assays to quantify these actions will lead to stronger preclinical candidates and an increasingly robust clinical pipeline for protein drug conjugates.

Reconsidering what makes a desirable solid tumor target

In Chapter 5, I proposed that a biparatopic antibody that increased internalization of an ADC would be beneficial to cellular delivery under tumor saturating conditions. Retrospectively, these results may not be surprising, however, the potential impact on new ADCs is likely underappreciated. As pointed out in Chapter 4, large antibody doses and high expression targets are currently shared among all the current FDA approved ADCs for solid tumors. While these design features have played a critical role in the success of these agents, this analysis does not mean that high expression is a must. In fact, large doses are a direct requirement due to the high receptor expression. Lower receptor systems are easier to saturate and therefore can use a lower antibody dose. The difficulty in targeting low receptor expression systems is two-fold: lower internalized ADC at site of action requiring more potent payloads and a higher ratio of systemic

to tumor exposure when compared to high expressing systems. Protein scaffolds that drive internalization of the low expression receptor have the potential to increase the tumor exposure relative to systemic exposure broadening the therapeutic window for these targets. While there are multiple high expression targets (HER2, Trop2, Nectin-4, Tissue Factor) there are many lower expression systems (A33, CEA, CD19, CD21) that could benefit from rapid internalization.

7.3 Concluding Remarks

ADCs have made remarkable progress since I began my thesis work. In 2016, only a single ADC, Kadcyla, was approved for solid tumor therapy. Since that time 10 additional ADCs (6 for hematological tumors and 4 solid tumor ADCs) have been clinically approved by the FDA. Considering the first ADC was tested preclinically in 1983, the recent success of ADCs is encouraging and stimulating the industry to reconsider this therapeutic modality. While previous attempts considered finding the strongest binder, most stable linker, and most potent payload, recent advances in quantitative experimental studies to identify driving factors in efficacy have highlighted the balance these parameters must share. For example, Trodelvy counteracts the traditional dogma of ADC design with a moderately potent payload and readily cleavable linker. The multifaceted interaction of protein-drug conjugates to their target system produces confounding principles in drug design in addition to broad potential to engineer this therapeutic modality to specific indications. In the age of personalized medicine, quantitative experimental measures and computational methods are required to understand the relationship between ADC design and the tumor microenvironment on patient outcomes. As we further our understanding of the impact these factors have on efficacy and the therapeutic window, these agents will progress towards the “magic bullet” theorized over 100 years ago.

Appendices

Appendix A – Krogh Cylinder Simulation Parameters

Drug	Parameter	Value	Unit	Description	Refererence
VH2-VH1	k_{on}	$4.57x10^5$	$M^{-1}s^{-1}$	On rate constant	measured
	k_{off}	$5.44x10^{-5}$	s^{-1}	Off rate constant	measured
	K_d	0.119	nM	Dissociation constant	measured
	k_α	4.25	hr^{-1}	Clearance rate constant for alpha phase	measured
	k_β	0.13	hr^{-1}	Clearance rate constant for beta phase	measured
	Fraction Alpha	99.13	%	Percentage of dose cleared in alpha half life	measured
	Diffusivity	70	$\mu m^2/s$	Diffusivity	(20)
	Permeability	$1x10^{-8}$	m/s	Vascular permeability	(20)
	Epsilon	0.32		Protein accessible volume	(20)
	K_e	$5.50x10^{-4}$	s^{-1}	Internalization rate constant	measured
VH1-HLE	k_{on}	$4.03x10^5$	$M^{-1}s^{-1}$	On rate constant	measured
	k_{off}	$3.64x10^{-4}$	s^{-1}	Off rate constant	measured
	K_d	0.902	nM	Dissociation constant	measured
	k_α	2.28	hr^{-1}	Clearance rate constant for alpha phase	measured
	k_β	0.10	hr^{-1}	Clearance rate constant for beta phase	measured
	Fraction Alpha	47.30	%	Percentage of dose cleared in alpha half life	measured
	Diffusivity	70	$\mu m^2/s$	Diffusivity	(20)
	Permeability	$1x10^{-8}$	m/s	Vascular permeability	(20)
	Epsilon	0.32		Protein accessible volume	(20)
	K_e	$1.75x10^{-4}$	s^{-1}	Internalization rate constant	measured
VH2-VH1-HLE	k_{on}	$1.74x10^5$	$M^{-1}s^{-1}$	On rate constant	measured
	k_{off}	$4.24x10^{-4}$	s^{-1}	Off rate constant	measured
	K_d	0.243	nM	Dissociation constant	measured
	k_α	1.84	hr^{-1}	Clearance rate constant for alpha phase	measured
	k_β	0.09	hr^{-1}	Clearance rate constant for beta phase	measured
	Fraction Alpha	37.70	%	Percentage of dose cleared in alpha half life	measured
	Diffusivity	40	$\mu m^2/s$	Diffusivity	(20)
	Permeability	$7.8x10^{-9}$	m/s	Vascular permeability	(20)
	Epsilon	0.30		Protein accessible volume	(20)
	K_e	$2.89x10^{-4}$	s^{-1}	Internalization rate constant	measured
J591	k_{on}	$1.53x10^4$	$M^{-1}s^{-1}$	On rate constant	measured
	k_{off}	$3.82x10^{-5}$	s^{-1}	Off rate constant	measured
	K_d	2.5	nM	Dissociation constant	measured
	k_α	3.2481	hr^{-1}	Clearance rate constant for alpha phase	measured
	k_β	0.0354	hr^{-1}	Clearance rate constant for beta phase	measured
	Fraction Alpha	38.15	%	Percentage of dose cleared in alpha half life	measured
	Diffusivity	10	$\mu m^2/s$	Diffusivity	(20)
	Permeability	$3.0x10^{-9}$	m/s	Vascular permeability	(20)
	Epsilon	0.24		Protein accessible volume	(20)
	K_e	$1.28x10^{-4}$	s^{-1}	Internalization rate constant	(39)
Tumor Parameters	H	0.45		Hematocrit	Green E. Biology (1966)
	$[Ag]_0$	805	nM	Initial antigen concentration	measured
	R_s	438	μM/s	Antigen recycle rate at steady state	calculated
	$R_{Capillary}$	8	μm	Radius of capillary	(37)
	R_{Krogh}	75	μm	Intercapillary distance	(37)

Appendix B – Krogh Cylinder Simulation Equations and Boundary Conditions

Free Protein

$$\frac{\partial C_{pro}}{\partial t} = D_{eff}\left(\frac{1}{r}\frac{\partial}{\partial r}\left(r\frac{\partial C_{pro}}{\partial r}\right)\right) - k_{on}\frac{C_{pro}}{\varepsilon}T_{free} + k_{off}B_{pro}$$

Free Target

$$\frac{\partial T_{free}}{\partial t} = R_s - k_{on}\frac{C_{pro}}{\varepsilon}T_{free} + k_{off}B_{pro} - k_e T_{free}$$

Bound Protein

$$\frac{\partial B_{pro}}{\partial t} = k_{on}\frac{C_{pro}}{\varepsilon}T_{free} - k_{off}B_{pro} - k_{int}B_{pro}$$

Internalized Protein

$$\frac{\partial C_{int,pro}}{\partial t} = k_{int}B_{pro} - k_{loss}C_{int,pro}$$

Boundary Conditions

1. Robin Boundary Condition at capillary wall

$$-D_{eff}\left.\frac{dC_{pro}}{dr}\right|_{r=R_{capillary}} = P\left(C_{plasma} - \frac{C_{pro,(R+1)}}{\varepsilon}\right)$$

2. Neuman no flux condition at outer edge

$$D_{eff}\left.\frac{dC_{pro}}{dr}\right|_{r=R_{Krogh}} = 0$$

References

1. Kaplon, H. & Reichert, J.M. Antibodies to watch in 2021. *MAbs* **13**, 1860476 (2021).

2. Suzuki, M., Kato, C. & Kato, A. Therapeutic antibodies: their mechanisms of action and the pathological findings they induce in toxicity studies. *J Toxicol Pathol* **28**, 133-139 (2015).

3. Hughes, B. Antibody-drug conjugates for cancer: poised to deliver? *Nature Reviews Drug Discovery* **9**, 665-667 (2010).

4. Zolot, R.S., Basu, S. & Million, R.P. Antibody-drug conjugates. *Nature Reviews Drug Discovery* **12**, 259-260 (2013).

5. Polakis, P. Antibody Drug Conjugates for Cancer Therapy. *Pharmacological Reviews* **68**, 3-19 (2016).

6. Tong, J.T.W., Harris, P.W.R., Brimble, M.A. & Kavianinia, I. An Insight into FDA Approved Antibody-Drug Conjugates for Cancer Therapy. *Molecules* **26** (2021).

7. Lambert, J.M. & Chari, R.V.J. Ado-trastuzumab Emtansine (T-DM1): An Antibody-Drug Conjugate (ADC) for HER2-Positive Breast Cancer. *Journal of Medicinal Chemistry* **57**, 6949-6964 (2014).

8. Vasalou, C., Helmlinger, G. & Gomes, B. A Mechanistic Tumor Penetration Model to Guide Antibody Drug Conjugate Design. *Plos One* **10** (2015).

9. Baxter, L.T. & Jain, R.K. TRANSPORT OF FLUID AND MACROMOLECULES IN TUMORS .4. A MICROSCOPIC MODEL OF THE PERIVASCULAR DISTRIBUTION. *Microvascular Research* **41**, 252-272 (1991).

10. Cilliers, C., Guo, H., Liao, J.S., Christodolu, N. & Thurber, G.M. Multiscale Modeling of Antibody-Drug Conjugates: Connecting Tissue and Cellular Distribution to Whole Animal Pharmacokinetics and Potential Implications for Efficacy. *Aaps J.* **18**, 1117-1130 (2016).

11. Jain, R.K., Martin, J.D. & Stylianopoulos, T. The Role of Mechanical Forces in Tumor Growth and Therapy. *Annual Review of Biomedical Engineering, Vol 16* **16**, 321-346 (2014).

12. Bergers, G. & Hanahan, D. Modes of resistance to anti-angiogenic therapy. *Nat. Rev. Cancer* **8**, 592-603 (2008).

13. Cilliers, C., Menezes, B., Nessler, I., Linderman, J. & Thurber, G.M. Improved Tumor Penetration and Single-Cell Targeting of Antibody-Drug Conjugates Increases Anticancer Efficacy and Host Survival. *Cancer Research* **78**, 758-768 (2018).

14. Khera, E. et al. Quantifying ADC bystander payload penetration with cellular resolution using pharmacodynamic mapping. *Neoplasia* **23**, 210-221 (2021).

15. Khera, E. et al. Cellular-Resolution Imaging of Bystander Payload Tissue Penetration from Antibody-Drug Conjugates. *Mol Cancer Ther* (2021).

16. Nessler, I., Menezes, B. & Thurber, G.M. Key metrics to expanding the pipeline of successful antibody-drug conjugates. *Trends Pharmacol Sci* **42**, 803-812 (2021).

17. Chan, A.C. & Carter, P.J. Therapeutic antibodies for autoimmunity and inflammation. *Nature Reviews: Immunology* **10**, 301-316 (2010).

18. Scott, A.M., Wolchok, J.D. & Old, L.J. Antibody therapy of cancer. *Nature Reviews: Cancer* **12**, 278-287 (2012).

19. Press, O.W. et al. Comparative metabolism and retention of iodine-125, yttrium-90, and indium-111 radioimmunoconjugates by cancer cells. *Cancer Res* **56**, 2123-2129 (1996).

20. Vugmeyster, Y., Xu, X., Theil, F.P., Khawli, L.A. & Leach, M.W. Pharmacokinetics and toxicology of therapeutic proteins: Advances and challenges. *World journal of biological chemistry* **3**, 73-92 (2012).

21. Bartelink, I.H. et al. Tumor drug penetration measurements could be the neglected piece of the personalized cancer treatment puzzle. *Clinical pharmacology and therapeutics* (2018).

22. Vinegoni, C. et al. Advances in measuring single-cell pharmacokinetics and pharmacology in vivo. *Drug Discov Today* (2015).

23. Kaur, S. et al. Recent trends in antibody-based oncologic imaging. *Cancer letters* **315**, 97-111 (2012).

24. Miller, M.A. & Weissleder, R. Imaging of anticancer drug action in single cells. *Nature Reviews: Cancer* **17**, 399-414 (2017).

25. Maxwell, J.L., Terracio, L., Borg, T.K., Baynes, J.W. & Thorpe, S.R. A fluorescent residualizing label for studies on protein uptake and catabolism in vivo and in vitro. *Biochemical Journal* **267**, 155-162 (1990).

26. Thorpe, S.R., Baynes, J.W. & Chroneos, Z.C. The design and application of residualizing labels for studies of protein catabolism. *The FASEB Journal* **7**, 399-405 (1993).

27. Wu, A.M. Engineered antibodies for molecular imaging of cancer. *Methods* **65**, 139-147 (2014).

28. Ferl, G.Z., Kenanova, V., Wu, A.M. & DiStefano, J.J. A two-tiered physiologically based model for dually labeled single-chain Fv-Fc antibody fragments. *Molecular Cancer Therapeutics* **5**, 1550-1558 (2006).

29. Yip, V. et al. Quantitative cumulative biodistribution of antibodies in mice: effect of modulating binding affinity to the neonatal Fc receptor. *MAbs* **6**, 689-696 (2014).

30. Cilliers, C., Liao, J., Atangcho, L. & Thurber, G.M. Residualization Rates of Near-Infrared Dyes for the Rational Design of Molecular Imaging Agents. *Molecular Imaging and Biology* **17**, 757-762 (2015).

31. Williams, S.-P. Tissue distribution studies of protein therapeutics using molecular probes: molecular imaging. *The AAPS journal* **14**, 389-399 (2012).

32. Weissleder, R. & Ntziachristos, V. Shedding light onto live molecular targets. *Nature Medicine* **9**, 123-128 (2003).

33. Marshall, M.V. et al. Near-Infrared Fluorescence Imaging in Humans with Indocyanine Green: A Review and Update. *Open Surgical Oncology Journal* **2**, 12-25 (2010).

34. Cohen, R., Vugts, D.J., Stigter-van Walsum, M., Visser, G.W.M. & van Dongen, G.a.M.S. Inert coupling of IRDye800CW and zirconium-89 to monoclonal antibodies for single- or dual-mode fluorescence and PET imaging. *Nature Protocols* **8**, 1010-1018 (2013).

35. Oliveira, S. et al. A novel method to quantify IRDye800CW fluorescent antibody probes ex vivo in tissue distribution studies. *EJNMMI research* **2**, 50 (2012).

36. Adams, G.P. et al. High affinity restricts the localization and tumor penetration of single-chain Fv antibody molecules. *Cancer Research* **61**, 4750-4755 (2001).

37. Urano, Y. et al. Selective molecular imaging of viable cancer cells with pH-activatable fluorescence probes. *Nature Medicine* **15**, 104-109 (2009).

38. Cilliers, C., Nessler, I., Christodolu, N. & Thurber, G.M. Tracking Antibody Distribution with Near-Infrared Fluorescent Dyes: Impact of Dye Structure and Degree of Labeling on Plasma Clearance. *Molecular Pharmaceutics* **14**, 1623-1633 (2017).

39. Wiley, H.S. Anomalous binding of epidermal growth factor to A431 cells is due to the effect of high receptor densities and a saturable endocytic system. *The Journal of Cell Biology* **107**, 801-810 (1988).

40. Austin, C.D. et al. Endocytosis and sorting of ErbB2 and the site of action of cancer therapeutics trastuzumab and geldanamycin. *Molecular Biology of the Cell* **15**, 5268-5282 (2004).

41. Ackerman, M.E. et al. A33 antigen displays persistent surface expression. *Cancer Immunology Immunotherapy* **57**, 1017-1027 (2008).

42. Warther, D. et al. Live-Cell One- and Two-Photon Uncaging of a Far-Red Emitting Acridinone Fluorophore. *Journal of the American Chemical Society* **132**, 2585-2590 (2010).

43. Barok, M., Joensuu, H. & Isola, J. Trastuzumab emtansine: mechanisms of action and drug resistance. *Breast Cancer Research* **16**, 3378-3378 (2014).

44. Natarajan, A., Turkcan, S., Gambhir, S.S. & Pratx, G. Multiscale Framework for Imaging Radiolabeled Therapeutics. *Molecular Pharmaceutics* **12**, 4554-4560 (2015).

45. Hazin, J., Moldenhauer, G., Altevogt, P. & Brady, N.R. A novel method for measuring cellular antibody uptake using imaging flow cytometry reveals distinct uptake rates for two different monoclonal antibodies targeting L1. *Journal of Immunological Methods* **423**, 70-77 (2015).

46. Wang, Y., Pennock, S., Chen, X. & Wang, Z. Endosomal Signaling of Epidermal Growth Factor Receptor Stimulates Signal Transduction Pathways Leading to Cell Survival. *Molecular and Cellular Biology* **22**, 7279-7290 (2002).

47. Boswell, C.A., Bumbaca, D., Fielder, P.J. & Khawli, L.A. Compartmental tissue distribution of antibody therapeutics: experimental approaches and interpretations. *The AAPS journal* **14**, 612-618 (2012).

48. Conner, K.P. et al. Evaluation of Near Infrared Fluorescent Labeling of Monoclonal Antibodies as a Tool for Tissue Distribution. *Drug Metab. Dispos.* **42**, 1906-1913 (2014).

49. Sato, K. et al. Impact of C4′-O-Alkyl Linker on in Vivo Pharmacokinetics of Near-Infrared Cyanine/Monoclonal Antibody Conjugates. *Molecular Pharmaceutics* **12**, 3303-3311 (2015).

50. Kate, C.I.t. et al. Effect of isoelectric point on biodistribution and inflammation imaging with indium-111-labelled IgG. *European Journal of Nuclear Medicine* **17**, 305-309 (1990).

51. Boswell, C.A. et al. Effects of Charge on Antibody Tissue Distribution and Pharmacokinetics. *Bioconjugate Chemistry* **21**, 2153-2163 (2010).

52. Yamasaki, Y. et al. Pharmacokinetic analysis of in vivo disposition of succinylated proteins targeted to liver nonparenchymal cells via scavenger receptors: importance of molecular size and negative charge density for in vivo recognition by receptors. *Journal of Pharmacology and Experimental Therapeutics* **301**, 467-477 (2002).

53. Sorkin, M.R., Walker, J.A., Kabaria, S.R., Torosian, N.P. & Alabi, C.A. Responsive Antibody Conjugates Enable Quantitative Determination of Intracellular Bond Degradation Rate. *Cell Chem Biol* **26**, 1643-1651 e1644 (2019).

54. Oliveira, S. et al. A novel method to quantify IRDye800CW fluorescent antibody probes ex vivo in tissue distribution studies. *EJNMMI Res* **2**, 50 (2012).

55. Sharma, S.K. et al. Noninvasive Interrogation of DLL3 Expression in Metastatic Small Cell Lung Cancer. *Cancer Res* **77**, 3931-3941 (2017).

56. Cunningham, C.W. et al. Uptake, Distribution and Diffusivity of Reactive Fluorophores in Cells: Implications toward Target Identification. *Molecular Pharmaceutics* **7**, 1301-1310 (2010).

57. Cilliers, C., Guo, H., Liao, J., Christodolu, N. & Thurber, G.M. Multiscale Modeling of Antibody-Drug Conjugates: Connecting Tissue and Cellular Distribution to Whole Animal Pharmacokinetics and Potential Implications for Efficacy. *AAPS J.* **18**, 1117-1130 (2016).

58. Thurber, G.M., Schmidt, M.M. & Wittrup, K.D. Factors determining antibody distribution in tumors. *Trends in pharmacological sciences* **29**, 57-61 (2008).

59. Diamantis, N. & Banerji, U. Antibody-drug conjugates-an emerging class of cancer treatment. *British Journal of Cancer* **114**, 362-367 (2016).

60. Khera, E., Cilliers, C., Bhatnagar, S. & Thurber, G.M. Computational transport analysis of antibody-drug conjugate bystander effects and payload tumoral distribution: implications for therapy. *Molecular Systems Design & Engineering* **3**, 73-88 (2018).

61. Tsumura, R. et al. Influence of the dissociation rate constant on the intra-tumor distribution of antibody-drug conjugate against tissue factor. *Journal of Controlled Release* **284**, 49-56 (2018).

62. Wu, A.M. & Senter, P.D. Arming antibodies: prospects and challenges for immunoconjugates. *Nature Biotechnology* **23**, 1137-1146 (2005).

63. Stern, L.A., Case, B.A. & Hackel, B.J. Alternative non-antibody protein scaffolds for molecular imaging of cancer. *Current Opinion in Chemical Engineering* **2**, 425-432 (2013).

64. Weidle, U.H., Auer, J., Brinkmann, U., Georges, G. & Tiefenthaler, G. The Emerging Role of New Protein Scaffold-based Agents for Treatment of Cancer. *Cancer Genomics & Proteomics* **10**, 155-168 (2013).

65. Simon, M., Frey, R., Zangemeister-Wittke, U. & Pluckthun, A. Orthogonal Assembly of a Designed Ankyrin Repeat Protein-Cytotoxin Conjugate with a Clickable Serum Albumin Module for Half-Life Extension. *Bioconjugate Chemistry* **24**, 1955-1966 (2013).

66. Thurber, G.M. & Wittrup, K.D. Quantitative spatiotemporal analysis of antibody fragment diffusion and endocytic consumption in tumor spheroids. *Cancer Research* **68**, 3334-3341 (2008).

67. Rudnick, S.I. et al. Influence of Affinity and Antigen Internalization on the Uptake and Penetration of Anti-HER2 Antibodies in Solid Tumors. *Cancer Research* **71**, 2250-2259 (2011).

68. Yokota, T., Milenic, D., Whitlow, M. & Schlom, J. Rapid Tumor Penetration of a Single-Chain Fv and Comparison with Other Immunoglobulin Forms. *Cancer Research* **52**, 3402-3408 (1992).

69. Less, J.R. et al. INTERSTITIAL HYPERTENSION IN HUMAN TUMORS .4. INTERSTITIAL HYPERTENSION IN HUMAN BREAST AND COLORECTAL TUMORS. *Cancer Research* **52**, 6371-6374 (1992).

70. Bannas, P., Hambach, J. & Koch-Nolte, F. Nanobodies and Nanobody-Based Human Heavy Chain Antibodies As Antitumor Therapeutics. *Frontiers in Immunology* **8** (2017).

71. Thurber, G.M., Zajic, S.C. & Wittrup, K.D. Theoretic criteria for antibody penetration into solid tumors and micrometastases. *Journal of Nuclear Medicine* **48**, 995-999 (2007).

72. Schmidt, M.M. & Wittrup, K.D. A modeling analysis of the effects of molecular size and binding affinity on tumor targeting. *Molecular Cancer Therapeutics* **8**, 2861-2871 (2009).

73. Hoefman, S., Ottevaere, I., Baumeister, J. & Sargentini-Maier, M.L. Pre-Clinical Intravenous Serum Pharmacokinetics of Albumin Binding and Non-Half-Life Extended Nanobodies (R). *Antibodies* **4**, 141-156 (2015).

74. Tijink, B.M. et al. Improved tumor targeting of anti-epidermal growth factor receptor Nanobodies through albumin binding: taking advantage of modular Nanobody technology. *Molecular Cancer Therapeutics* **7**, 2288-2297 (2008).

75. Dennis, M.S. et al. Imaging tumors with an albumin-binding Fab, a novel tumor-targeting agent. *Cancer Research* **67**, 254-261 (2007).

76. Dennis, M.S. et al. Albumin binding as a general strategy for improving the pharmacokinetics of proteins. *J. Biol. Chem.* **277**, 35035-35043 (2002).

77. Steiner, D. et al. Half-life extension using serum albumin-binding DARPin (R) domains. *Protein Eng. Des. Sel.* **30**, 583-591 (2017).

78. Spiess, C., Zhai, Q.T. & Carter, P.J. Alternative molecular formats and therapeutic applications for bispecific antibodies. *Molecular Immunology* **67**, 95-106 (2015).

79. Miller, M.L. et al. A DNA-Interacting Payload Designed to Eliminate Cross-Linking Improves the Therapeutic Index of Antibody-Drug Conjugates (ADCs). *Mol Cancer Ther* **17**, 650-660 (2018).

80. Mayor, S., Rothberg, K. & Maxfield, F. Sequestration of GPI-Anchored Proteins in Caveolae Triggered by Cross-Linking. *Science* **264**, 1948-1951 (1994).

81. Liu, H. et al. Constitutive and antibody-induced internalization of prostate-specific membrane antigen. *Cancer Res* **58**, 4055-4060 (1998).

82. Dennis, M.S. et al. Imaging tumors with an albumin-binding Fab, a novel tumor-targeting agent. **67**, 254-261 (2007).

83. Khera, E. et al. Blocking Glucagon Like Peptide-1 Receptors in the Exocrine Pancreas Improves Specificity for Beta Cells in a Mouse Model of Type 1 Diabetes. *J Nucl Med* (2019).

84. Eary, J.F. et al. SUCCESSFUL IMAGING OF MALIGNANT-MELANOMA WITH TECHNETIUM-99M-LABELED MONOCLONAL-ANTIBODIES. *Journal of Nuclear Medicine* **30**, 25-32 (1989).

85. Oldham, R.K. et al. MONOCLONAL-ANTIBODY THERAPY OF MALIGNANT-MELANOMA - INVIVO LOCALIZATION IN CUTANEOUS METASTASIS AFTER INTRAVENOUS ADMINISTRATION. *Journal of Clinical Oncology* **2**, 1235-1244 (1984).

86. Oosterwijk, E. et al. ANTIBODY LOCALIZATION IN HUMAN RENAL-CELL CARCINOMA - A PHASE-I STUDY OF MONOCLONAL ANTIBODY-G250. *Journal of Clinical Oncology* **11**, 738-750 (1993).

87. Thurber, G.M., Schmidt, M.M. & Wittrup, K.D. Antibody tumor penetration: Transport opposed by systemic and antigen-mediated clearance. *Advanced Drug Delivery Reviews* **60**, 1421-1434 (2008).

88. Ong, G. & Mattes, M.J. Penetration and Binding of Antibodies in Experimental Human Solid Tumors Grown in Mice. *Cancer Research* **49**, 4264-4273 (1989).

89. Sancey, L. et al. Clustering and internalization of integrin alphavbeta3 with a tetrameric RGD-synthetic peptide. *Molecular therapy : the journal of the American Society of Gene Therapy* **17**, 837-843 (2009).

90. Li, J.Y. et al. ABiparatopic HER2-Targeting Antibody-Drug Conjugate Induces Tumor Regression in Primary Models Refractory to or Ineligible for HER2-Targeted Therapy. *Cancer Cell* **29**, 117-129 (2016).

91. Li, F. et al. Intracellular Released Payload Influences Potency and Bystander-Killing Effects of Antibody-Drug Conjugates in Preclinical Models. *Cancer Research* **76**, 2710-2719 (2016).

92. Hamblett, K.J. et al. Effects of drug loading on the antitumor activity of a monoclonal antibody drug conjugate. *Clin Cancer Res* **10**, 7063-7070 (2004).

93. Hinrichs, M.J.M. et al. Fractionated Dosing Improves Preclinical Therapeutic Index of Pyrrolobenzodiazepine-Containing Antibody Drug Conjugates. *Clin Cancer Res* **23**, 5858-5868 (2017).

94. Dal Corso, A., Gebleux, R., Murer, P., Soltermann, A. & Neri, D. A non-internalizing antibody-drug conjugate based on an anthracycline payload displays potent therapeutic activity in vivo. *Journal of Controlled Release* **264**, 211-218 (2017).

95. Gebleux, R., Stringhini, M., Casanova, R., Soltermann, A. & Neri, D. Non-internalizing antibody-drug conjugates display potent anti-cancer activity upon proteolytic release of monomethyl auristatin E in the subendothelial extracellular matrix. *Int. J. Cancer* **140**, 1670-1679 (2017).

96. Shah, D.K., Haddish-Berhane, N. & Betts, A. Bench to bedside translation of antibody drug conjugates using a multiscale mechanistic PK/PD model: a case study with brentuximab-vedotin. *Journal of Pharmacokinetics and Pharmacodynamics* **39**, 643-659 (2012).

97. Fujimori, K., Covell, D.G., Fletcher, J.E. & Weinstein, J.N. A MODELING ANALYSIS OF MONOCLONAL-ANTIBODY PERCOLATION THROUGH TUMORS - A BINDING-SITE BARRIER. *Journal of Nuclear Medicine* **31**, 1191-1198 (1990).

98. Bhatnagar, S., Deschenes, E., Liao, J., Cilliers, C. & Thurber, G.M. Multichannel Imaging to Quantify Four Classes of Pharmacokinetic Distribution in Tumors. *Journal of Pharmaceutical Sciences* **103**, 3276-3286 (2014).

99. Zhang, L., Navaratna, T., Liao, J.S. & Thurber, G.M. Dual-Purpose Linker for Alpha Helix Stabilization and Imaging Agent Conjugation to Glucagon-Like Peptide-1 Receptor Ligands. *Bioconjugate Chemistry* **26**, 329-337 (2015).

100. Zhang, L., Navaratna, T. & Thurber, G.M. A Helix-Stabilizing Linker Improves Subcutaneous Bioavailability of a Helical Peptide Independent of Linker Lipophilicity. *Bioconjugate Chemistry* **27**, 1663-1672 (2016).

101. Kampmeier, F., Williams, J.D., Maher, J., Mullen, G.E. & Blower, P.J. Design and preclinical evaluation of a Tc-99m-labelled diabody of mAb J591 for SPECT imaging of prostate-specific membrane antigen (PSMA). *Ejnmmi Research* **4** (2014).

102. Zhang, L. & Thurber, G.M. Quantitative Impact of Plasma Clearance and Down-regulation on GLP-1 Receptor Molecular Imaging. *Molecular Imaging and Biology* **18**, 79-89 (2016).

103. Tung, Y.C. et al. High-throughput 3D spheroid culture and drug testing using a 384 hanging drop array. *Analyst* **136**, 473-478 (2011).

104. Goldenberg, D.M., Cardillo, T.M., Govindan, S.V., Rossi, E.A. & Sharkey, R.M. Trop-2 is a novel target for solid cancer therapy with sacituzumab govitecan (IMMU-132), an antibody-drug conjugate (ADC). *Oncotarget* **6**, 22496-22512 (2015).

105. Iwata, T.N. et al. A HER2-Targeting Antibody-Drug Conjugate, Trastuzumab Deruxtecan (DS-8201a), Enhances Antitumor Immunity in a Mouse Model. *Mol Cancer Ther* **17**, 1494-1503 (2018).

106. Mathe, G., Tran Ba, L.O. & Bernard, J. [Effect on mouse leukemia 1210 of a combination by diazo-reaction of amethopterin and gamma-globulins from hamsters inoculated with such leukemia by heterografts]. *C R Hebd Seances Acad Sci* **246**, 1626-1628 (1958).

107. Ghose, T. et al. Immunochemotherapy of cancer with chlorambucil-carrying antibody. *Br Med J* **3**, 495-499 (1972).

108. Ford, C.H. et al. Localisation and toxicity study of a vindesine-anti-CEA conjugate in patients with advanced cancer. *Br J Cancer* **47**, 35-42 (1983).

109. Riechmann, L., Clark, M., Waldmann, H. & Winter, G. Reshaping human antibodies for therapy. *Nature* **332**, 323-327 (1988).

110. Weinstein, J.N. et al. The pharmacology of monoclonal antibodies. *Ann N Y Acad Sci* **507**, 199-210 (1987).

111. Jain, R.K. Transport of molecules in the tumor interstitium: a review. *Cancer Res* **47**, 3039-3051 (1987).

112. Jain, R.K. Transport of molecules across tumor vasculature. *Cancer Metastasis Rev* **6**, 559-593 (1987).

113. Gai, S.A. & Wittrup, K.D. Yeast surface display for protein engineering and characterization. *Curr Opin Struct Biol* **17**, 467-473 (2007).

114. Weiner, L.M. & Adams, G.P. New approaches to antibody therapy. *Oncogene* **19**, 6144-6151 (2000).

115. Donaghy, H. Effects of antibody, drug and linker on the preclinical and clinical toxicities of antibody-drug conjugates. *Mabs* **8**, 659-671 (2016).

116. Ponte, J.F. et al. Antibody Co-Administration Can Improve Systemic and Local Distribution of Antibody-Drug Conjugates to Increase In Vivo Efficacy. *Mol Cancer Ther* **20**, 203-212 (2021).

117. Cruz, E. & Kayser, V. Monoclonal antibody therapy of solid tumors: clinical limitations and novel strategies to enhance treatment efficacy. *Biologics* **13**, 33-51 (2019).

118. Nessler, I., Khera, E. & Thurber, G.M. Quantitative pharmacology in antibody-drug conjugate development: armed antibodies or targeted small molecules? *Oncoscience* **5**, 161-163 (2018).

119. Rios-Doria, J. et al. Antibody-Drug Conjugates Bearing Pyrrolobenzodiazepine or Tubulysin Payloads Are Immunomodulatory and Synergize with Multiple Immunotherapies. *Cancer Res* **77**, 2686-2698 (2017).

120. Zhou, J. et al. Immunogenic cell death in cancer therapy: Present and emerging inducers. *J Cell Mol Med* **23**, 4854-4865 (2019).

121. Hoffmann, R.M. et al. Antibody structure and engineering considerations for the design and function of Antibody Drug Conjugates (ADCs). *Oncoimmunology* **7**, e1395127 (2018).

122. U.S.FDA Kadcyla Biologic License Application (125427Orig1s000). *Pharmacol Rev* (2013).

123. Ogitani, Y. et al. DS-8201a, A Novel HER2-Targeting ADC with a Novel DNA Topoisomerase I Inhibitor, Demonstrates a Promising Antitumor Efficacy with Differentiation from T-DM1. *Clin Cancer Res* **22**, 5097-5108 (2016).

124. Sun, N. et al. Clinical application of the AUC-guided dosage adjustment of docetaxel-based chemotherapy for patients with solid tumours: a single centre, prospective and randomised control study. *J Transl Med* **18**, 226 (2020).

125. Zhang, D. et al. Exposure-Efficacy Analysis of Antibody-Drug Conjugates Delivering an Excessive Level of Payload to Tissues. *Drug Metab Dispos* **47**, 1146-1155 (2019).

126. Krasner, C. & Joyce, R.M. Zevalin: 90yttrium labeled anti-CD20 (ibritumomab tiuxetan), a new treatment for non-Hodgkin's lymphoma. *Curr Pharm Biotechnol* **2**, 341-349 (2001).

127. Boswell, C.A. et al. Differential Effects of Predosing on Tumor and Tissue Uptake of an In-111-Labeled Anti-TENB2 Antibody-Drug Conjugate. *Journal of Nuclear Medicine* **53**, 1454-1461 (2012).

128. Nessler, I. et al. Increased Tumor Penetration of Single-Domain Antibody-Drug Conjugates Improves In Vivo Efficacy in Prostate Cancer Models. *Cancer Res* **80**, 1268-1278 (2020).

129. Thurber, G.M. & Weissleder, R. Quantitating antibody uptake in vivo: conditional dependence on antigen expression levels. *Mol Imaging Biol* **13**, 623-632 (2011).

130. Dijkers, E.C. et al. Biodistribution of Zr-89-trastuzumab and PET Imaging of HER2-Positive Lesions in Patients With Metastatic Breast Cancer. *Clin. Pharmacol. Ther.* **87**, 586-592 (2010).

131. Bang, Y.J. et al. First-in-human phase 1 study of margetuximab (MGAH22), an Fc-modified chimeric monoclonal antibody, in patients with HER2-positive advanced solid tumors. *Ann Oncol* **28**, 855-861 (2017).

132. Ponte, J.F. et al. Antibody Co-Administration Can Improve Systemic and Local Distribution of Antibody Drug Conjugates to Increase In Vivo Efficacy. *Molecular Cancer Therapeutics* (2020, in press).

133. Yoder, N.C. et al. A Case Study Comparing Heterogeneous Lysine- and Site-Specific Cysteine-Conjugated Maytansinoid Antibody-Drug Conjugates (ADCs) Illustrates the Benefits of Lysine Conjugation. *Mol Pharm* **16**, 3926-3937 (2019).

134. Burton, J.K., Bottino, D. & Secomb, T.W. A Systems Pharmacology Model for Drug Delivery to Solid Tumors by Antibody-Drug Conjugates: Implications for Bystander Effects. *The AAPS journal* **22**, 12 (2019).

135. Thuss-Patience, P.C. et al. Trastuzumab emtansine versus taxane use for previously treated HER2-positive locally advanced or metastatic gastric or gastro-oesophageal junction adenocarcinoma (GATSBY): an international randomised, open-label, adaptive, phase 2/3 study. *Lancet Oncol* **18**, 640-653 (2017).

136. Shitara, K. et al. Trastuzumab Deruxtecan in Previously Treated HER2-Positive Gastric Cancer. *N Engl J Med* **382**, 2419-2430 (2020).

137. Sukumaran, S. et al. Mechanism-Based Pharmacokinetic/Pharmacodynamic Model for THIOMAB Drug Conjugates. *Pharm Res* **32**, 1884-1893 (2015).

138. Junutula, J.R. et al. Site-specific conjugation of a cytotoxic drug to an antibody improves the therapeutic index. *Nat Biotechnol* **26**, 925-932 (2008).

139. Pabst, M. et al. Modulation of drug-linker design to enhance in vivo potency of homogeneous antibody-drug conjugates. *J Control Release* **253**, 160-164 (2017).

140. Thurber, G.M. & Weissleder, R. A Systems Approach for Tumor Pharmacokinetics. *Plos One* **6** (2011).

141. Cardillo, T.M. et al. Sacituzumab Govitecan (IMMU-132), an Anti-Trop-2/SN-38 Antibody-Drug Conjugate: Characterization and Efficacy in Pancreatic, Gastric, and Other Cancers. *Bioconjug Chem* **26**, 919-931 (2015).

142. Goldenberg, D.M. & Sharkey, R.M. Sacituzumab govitecan, a novel, third-generation, antibody-drug conjugate (ADC) for cancer therapy. *Expert Opin Biol Ther* **20**, 871-885 (2020).

143. Sharkey, R.M. et al. Enhanced Delivery of SN-38 to Human Tumor Xenografts with an Anti-Trop-2-SN-38 Antibody Conjugate (Sacituzumab Govitecan). *Clin Cancer Res* **21**, 5131-5138 (2015).

144. Schmidt, M.M., Thurber, G.M. & Wittrup, K.D. Kinetics of anti-carcinoembryonic antigen antibody internalization: effects of affinity, bivalency, and stability. *Cancer Immunol Immunother* **57**, 1879-1890 (2008).

145. Hafeez, U., Parakh, S., Gan, H.K. & Scott, A.M. Antibody-Drug Conjugates for Cancer Therapy. *Molecules* **25** (2020).

146. Nessler, Cilliers & Thurber Practical Guide for Quantification of In Vivo Degradation Rates for Therapeutic Proteins with Single-Cell Resolution Using Fluorescence Ratio Imaging. *Pharmaceutics* **12** (2020).

147. Borcoman, E. & Le Tourneau, C. Antibody drug conjugates: the future of chemotherapy? *Curr. Opin. Oncol.* **28**, 429-436 (2016).

148. Wittrup, K.D. Antitumor Antibodies Can Drive Therapeutic T Cell Responses. *Trends Cancer* **3**, 615-620 (2017).

149. Tsuchikama, K. & An, Z.Q. Antibody-drug conjugates: recent advances in conjugation and linker chemistries. *Protein & Cell* **9**, 33-46 (2018).

150. Gemmete, J.J. & Mukherji, S.K. Trastuzumab (Herceptin). *Am. J. Neuroradiol.* **32**, 1373-1374 (2011).

151. Muller, P. et al. Trastuzumab emtansine (T-DM1) renders HER2(+) breast cancer highly susceptible to CTLA-4/PD-1 blockade. *Science Translational Medicine* **7** (2015).

152. Royce, M. et al. FDA Approval Summary: Margetuximab plus Chemotherapy for Advanced or Metastatic HER2-Positive Breast Cancer. *Clin Cancer Res* (2021).

153. van der Horst, H.J., Nijhof, I.S., Mutis, T. & Chamuleau, M.E.D. Fc-Engineered Antibodies with Enhanced Fc-Effector Function for the Treatment of B-Cell Malignancies. *Cancers (Basel)* **12** (2020).

154. Park, H.I., Yoon, H.W. & Jung, S.T. The Highly Evolvable Antibody Fc Domain. *Trends Biotechnol* **34**, 895-908 (2016).

155. Li, F. et al. Intracellular Released Payload Influences Potency and Bystander-Killing Effects of Antibody-Drug Conjugates in Preclinical Models. *Cancer Res* **76**, 2710-2719 (2016).

156. Moynihan, K.D. et al. Eradication of large established tumors in mice by combination immunotherapy that engages innate and adaptive immune responses. *Nat Med* **22**, 1402-1410 (2016).

157. Jiang, T. et al. Tumor neoantigens: from basic research to clinical applications. *J Hematol Oncol* **12**, 93 (2019).

158. Steenbrugge, J. et al. Comparative Profiling of Metastatic 4T1- vs. Non-metastatic Py230-Based Mammary Tumors in an Intraductal Model for Triple-Negative Breast Cancer. *Front Immunol* **10**, 2928 (2019).

159. Grasselly, C. et al. The Antitumor Activity of Combinations of Cytotoxic Chemotherapy and Immune Checkpoint Inhibitors Is Model-Dependent. *Front Immunol* **9**, 2100 (2018).

160. Gregorio, A.C. et al. Inoculated Cell Density as a Determinant Factor of the Growth Dynamics and Metastatic Efficiency of a Breast Cancer Murine Model. *PLoS One* **11**, e0165817 (2016).